Modelling Coupled Surface Water-Groundwater Flow and Heat Transport in a Catchment in a Discontinuous Permafrost Zone in Umiujaq, Northern Québec

Thèse

Masoumeh Parhizkar

Doctorat interuniversitaire en sciences de la Terre
Philosophiæ doctor (Ph. D.)

Québec, Canada

Modelling Coupled Surface Water-Groundwater Flow and Heat Transport in a Catchment in a Discontinuous Permafrost Zone in Umiujaq, Northern Québec

Thèse

Masoumeh Parhizkar

Sous la direction de :

René Therrien, directeur de recherche

John Molson, codirecteur de recherche

Résumé

Les systèmes hydrogéologiques devraient réagir au changement climatique de manière complexe. En région froide, la simulation de l'effet du changement climatique nécessite un modèle hydrologique intégré de pointe. Dans cette recherche, un modèle numérique entièrement couplé en 3D a été développé pour simuler l'écoulement des eaux souterraines et le transport de chaleur dans un bassin versant dans la région d'Umiujaq, dans le nord du Québec, au Canada.

Le bassin versant est situé dans une zone de pergélisol discontinue et contient une épaisse couche glaciofluviale à grains grossiers formant un bon aquifère sous une unité gélive de silts marins sensible au gel. Une étude de terrain détaillée a été réalisée pour mesurer les caractéristiques du bassin versant telles que les propriétés hydrauliques et thermiques et la distribution des unités géologiques. Trois méthodes différentes disponibles dans le logiciel PEST sont utilisées pour caler le modèle 3D par rapport aux charges hydrauliques mesurées. Les résultats ont montré que l'utilisation de méthodes de calage simplifiées, telles que la méthode de zonation, n'est pas efficace dans cette zone d'étude, qui est très hétérogène. L'utilisation d'un calage plus détaillé par les méthodes du système PEST de points pilotes a permis de mieux s'adapter aux valeurs observées. Cependant, le temps de calcul était élevé.

L'effet de la condition initiale pour la simulation du transport de chaleur est étudié en appliquant une condition initiale différente au modèle. Les résultats montrent que l'inclusion du processus de démarrage dans les simulations produit des températures simulées plus stables. Les zones du modèles à des profondeurs plus élevées, en-dessous de la profondeur de pénétration des variations saisonnières de température, nécessitent des temps de simulation plus longs pour être en équilibre avec les conditions limites appliquées.

Les résultats montrent que l'application de la température moyenne de surface en tant que condition limite pour la simulation du transport de chaleur donne un meilleur ajustement aux valeurs observées en été qu'en hiver. En hiver, du fait de l'épaisseur variable de la neige dans le bassin versant, l'utilisation d'une température de surface uniforme diminue la qualité de l'ajustement aux valeurs observées.

L'inclusion de l'advection dans la simulation du transport de chaleur accélère le taux d'augmentation de la température. De plus, l'eau chaude qui pénètre dans le sous-sol

augmente la température souterraine dans les zones de recharge. Lorsque les eaux souterraines s'écoulent, elles perdent de l'énergie thermique. Par conséquent, le taux d’augmentation de la température dans les zones de décharge est inférieur à celui des zones de recharge.

Abstract

Groundwater systems are expected to respond to climate change in a complex way. In cold regions, simulating the effect of climate change requires a state-of-the-art integrated hydrologic model. In this research, a fully coupled 3D numerical model has been developed to simulate groundwater-surface water flow and heat transport in a 2-km^2 catchment in Umiujaq, Nunavik (northern Quebec), Canada.

The catchment is located in a discontinuous permafrost zone. It contains a lower aquifer, consisting of a thick coarse-grained glaciofluvial layer, overlain by a frost-susceptible silty marine unit and a perched upper aquifer. Detailed field investigations have been carried out to characterize the catchment, including its hydraulic and thermal properties and the subsurface geology.

Three different calibration methods using the inverse calibration code PEST were used to calibrate the 3D flow model against measured hydraulic heads, assuming a fixed distribution of low hydraulic conductivity for discontinuous permafrost blocks. Heat transfer was not considered for this calibration. Results showed that using simplified calibration methods, such as the zoning method, is not efficient in this study area, which is highly heterogeneous. Using a more detailed calibration, such as the pilot-points method of PEST, gave a better fit to observed values. However, the computational time was significantly higher.

In subsequent simulations, which included heat transport, different approaches for assigning initial temperatures during model spin-up were investigated. Results show that including the spin-up process in the simulations produces more realistic simulated temperatures. Furthermore, the spin-up improves the model fit to deeper subsurface temperatures because areas of the subsurface below the depth where seasonal surface temperature variations penetrate require longer simulation times to reach equilibrium with the applied boundary conditions.

Applying the annual average surface temperature as the boundary condition to the heat transport simulation provided a better fit to observed values in the summer compared to winter. During winter, because of different snow thicknesses throughout the catchment, using a uniform surface temperature results in a poor fit to observed values.

Simulations show that warm water entering the subsurface increases the subsurface temperature in the recharge areas. As groundwater flows through the subsurface, it loses thermal energy. Therefore, discharging water is cooler than recharging water. This causes the rate of temperature rise to be lower in discharge areas than in recharge areas.

The modelling results have helped provide insights into 3D simulation of coupled water flow-heat transfer processes. Furthermore, it will help users of cryo-hydrogeological models in understanding effective parameters in development and calibration of model to develop their own site-specific models.

Contents

List of Tables

List of Figures

To my Family…

Acknowledgment

This has been a long journey, in which I have met many amazing people who helped me to accomplish my PhD. I am extremely grateful to everyone who helped me in this path.

I would like to express my deepest appreciation to my supervisor, Prof. René Therrien, for his generous support, expert guidance, and constructive advice. His kindness and continuous support have made my PhD experience one of the best and memorable stages of my life. I have been fortunate to have had this opportunity to work under his supervision. My success in the completion of my dissertation would have not been possible without his support…Thank you René, for everything.

I would like to extend my sincere thanks to my co-supervisor, Prof. John Molson, for his valuable advice and professional feedback and reviews throughout this PhD and in writing of this dissertation.

Many thanks to the external examiners on my doctoral dissertation committee: Prof. Alain Dassargues, Prof. Jasmin Raymond, and Prof. Claudio Paniconi for providing valuable comments and constructive questions.

I am also grateful to Prof. Jean-Michel Lemieux and Prof. Richard Fortier, who have shared their expert knowledge and experience about hydrogeology of Umiujaq, which was significantly helpful to complete this research.

I would like to acknowledge the help of PhD and MSc students who provided field observation data and shared their experiences about Umiujaq, including David Banville, Renaud Murray, Sophie Dagenais, and Dr. Marion Cochand.

Many thanks to my friends and officemates who helped to sustain a positive atmosphere and made my study more enjoyable, including Vinicius Ferreira Boico, Jonathan Fortin, Alexandra Germain, Pierrick Lamontagne-Hallé, and Shuai Guo.

I would like to acknowledge the assistance of the staff of the Department of Geology and Geological Engineering, including Marie-Catherine Talbot Poulin, Pierre Therrien, Guylain Gaumond, Marcel Langlois, and many others.

I cannot begin to express my thanks to my parents and my sisters for their unconditional love and unwavering belief in me, which always gave me the confidence to overcome the challenges and move beyond what I thought I could.

Above all, I would like to thank my love and husband, Dr. Amir Bolouri, for his endless love, support, and patience, which helped me to pursue my study and get to this point. Thank you for being my editor, proofreader, and sounding board. But most of all, thank you for being my best friend.

Without all these supports, this dissertation would have not been possible.

Avant-propos

Chapter 3 of this thesis is an article published by the Canadian Geotechnical Society and presented at the GeoOttawa 2017 conference. The work described in this article was performed during my Doctoral degree at Laval University, under the supervision of Prof. René Therrien and Prof. John Molson. The article describes the initial stage of my PhD research project, involving development and calibration of the water flow model. My role was to develop the 3D model and calibrate it using the available field data. I wrote the manuscript with advice from Prof. René Therrien and Prof. John Molson. The field data used to calibrate the model were obtained by the research team under the supervision of Prof. John-Michel Lemieux and Prof. Richard Fortier and with help from Marie-Catherine Talbot Poulin and Michel Ouellet. Pierre Therrien helped in developing the 2D mesh of the model, which then was transformed to a 3D mesh. The article and the co-authors are as follows:

Parhizkar, M., Therrien, R., Molson, J., Lemieux, JM., Fortier, R., Talbot Poulin, MC., Therrien, P., & Ouellet, M. (2017) An Integrated Surface-Subsurface Flow Model of the Thermo-Hydrological Behavior and Effect of Climate Change in a Cold-Region Catchment in Northern Quebec, Canada. GeoOttawa 2017: the 70th Canadian Geotechnical Conference and the 12th Joint CGS/IAH-CNC Groundwater Conference, Canadian Geotech Soc, Ottawa, 1-4 Oct. 2017.

Introduction

Background and motivation

Climate change is having a significant impact on ecosystems, economies and communities as well as on subsurface thermal regimes. Climate change can increase groundwater and soil temperatures, which can affect groundwater quality, harm groundwater-sourced ecosystems, and contribute to the geotechnical failure of infrastructure.

Various studies have been conducted to evaluate the effect of climate change on groundwater resources. For example, Menberg et al. (2014) investigated groundwater temperature response to recent climate change. They examined the coupling of atmospheric and groundwater warming with stochastic and deterministic models. Their findings demonstrated that shallow groundwater temperatures have responded rapidly to climate change, thus providing insight into the vulnerability of aquifers and groundwater-dependent ecosystems to future climate change. Lemieux et al. (2015) applied the finite-element model FEFLOW to quantify the potential impact of climate change on freshwater resources of the Magdalen Islands, Quebec, by simulating variable-density flow (induced by saltwater intrusion) and solute transport under saturated-unsaturated conditions. Simulation results showed that the most important impact on groundwater would be caused by sea-level rise, followed by decreasing groundwater recharge and coastal erosion.

Groundwater systems are expected to respond to climate change in a complex way (Bloomfield et al., 2013). Since groundwater supplies almost half of the global drinking water demand (Van der Gun, 2012), investigating the impact of climate change on groundwater temperature and quality is a high priority.

However, further studies are required to better quantify groundwater response to climate change in cold areas. The increase in atmospheric temperature resulting from climate change can lead to permafrost thaw in high altitude and/or high latitude regions. Permafrost is a soil or rock formation that remains at or below the freezing point of water for two or more consecutive years (Dobinski, 2011). Water in the pores of these soils is therefore stored as ice and is essentially immobile and not recoverable by pumping. In addition, permafrost acts as a frozen impervious layer that limits recharge of underlying aquifers, thus decreasing the availability and sustainability of groundwater resources.

The spatial distribution of permafrost is controlled by several factors including air temperature, vegetation and land surface slope (Shur and Jorgenson, 2007; Jorgenson et al., 2010). According to the Intergovernmental Panel on Climate Change (IPCC, 2007), anticipated climate warming at high latitudes will cause thawing of permafrost over the coming decades. Water trapped as ice will be released and aquifer recharge will increase, which will also likely increase the potential for exploitation of groundwater as a source of drinking water. It is notable that climate change is projected to be most severe at high latitudes, leading to decreasing sea ice, permafrost warming or degradation, increasing carbon dioxide release from soils, decreasing glacier ice mass, and shifting biological indicators (Kurylyk et al. 2014a).

Several studies have been conducted over the past few years to survey the effect of climate change on subsurface conditions in northern regions, including temperature, permafrost distribution, and water quality. The hydrology of the active layer, which is the top layer of soil above permafrost that freezes and thaws on an annual basis, was studied by Quinton and Baltzer (2013) for a thawing peat plateau in a wetland-dominated zone of discontinuous permafrost. Results showed that permafrost thaw reduced subsurface runoff by lowering the hydraulic gradient, increasing the active layer thickness and, most importantly, reducing the surface area of the thawing peat plateau. Wu et al. (2015) investigated changes in active-layer thickness and near-surface permafrost between 2002 and 2012 at 10 sites within five alpine ecosystems. All sites showed an increase in active-layer thickness and near-surface permafrost temperature. They suggested that the primary control on the active-layer thickness increase was an increase in summer rainfall and the primary control on increasing permafrost temperature was probably the combined effects of increasing rainfall and the asymmetrical seasonal changes in subsurface soil temperatures.

Integrated surface and subsurface hydrologic models are valuable tools to understand and characterize catchment functions and behaviour. The following sections will review the available literature for integrated simulations of surface water/ groundwater flow and coupled water flow and heat transfer simulations. Missing gaps in previous research studies are then discussed and the objectives of this study are defined to fulfill some of this missing knowledge.

Literature review

Integrated simulations for groundwater flow

The terrestrial portion of the water cycle is only one of the many inter-connected components of the complete water cycle. Simulations of catchment-scale groundwater processes are therefore moving towards integration. In an integrated simulation framework, groundwater, surface water and other environmental components are considered as one system. When environmental processes are simulated separately, usually some important assumptions and simplifications are made, which potentially increases the error and uncertainty in the results. Integrated simulation of environmental processes can help to reduce these potential errors.

Integrated simulation of surface and subsurface flow has been used, for example, to study the process of runoff generation (Frei et al. 2010, Liggett et al. 2015, Park et al. 2011, Weill et al., 2013). Ala-aho et al. (2017) applied the HydroGeoSphere model (HGS) for integrated surface-subsurface hydrological simulations to study the role of groundwater in headwater catchment runoff generation. They used a novel calibration approach, which included the main hydrological parameters and minimal field data to simulate the main characteristics of runoff generation. They showed that the model output in an integrated simulation is sensitive to surface parameters as well as subsurface parameters. Therefore, the surface parameters, such as Manning's coefficients, are appropriate to include in the calibration. Furthermore, they showed that adding observational data improved the model calibration for some output targets, for example groundwater levels, but not for other targets such as evapotranspiration time series.

Jones et al. (2008) applied the Integrated Hydrologic Model (InHM) to a 75-km^2 watershed in southern Ontario to investigate the model's ability to simulate transient flow processes. They initially calibrated the subsurface flow properties to observed steady-state hydraulic heads and baseflow. They then simulated the stream hydrograph by applying two rainfall time series and compared them to the observed rainfall-runoff responses. Results showed that the model could realistically simulate the fully integrated surface/variably-saturated subsurface flow system.

Ala-aho et al. (2015) applied HGS to investigate groundwater (GW) and surface water (SW) interactions in both steady-state and transient modes in an esker located in northern Finland.

The model reproduced the magnitude, temporal variability and spatial distribution of water fluxes at the GW-SW interface. The results were compared to those obtained from airborne measurements of thermal infrared radiation and from mass balance based on stable isotope (δ18O) data. The general pattern of GW inflow locations to lakes, interpreted from areal thermal imaging, was captured by the simulations, and the GW flux to lakes calculated with the stable isotope technique showed good agreement with the simulations, including reasonable estimates of the hydraulic head and stream baseflow distribution throughout the aquifer. The differences between simulations and observations were mainly attributed to difficulties in observing GW inflow locations with thermal imaging data, model mesh resolution, and a simplified geological model, which led to overestimation of hydraulic head. They concluded that, since field methods for studying transient influxes in a lake system would be labour-intensive, developing a model to reproduce the discharge locations and flow volumes is useful.

Hwang et al. (2018) used HGS to study the effect of parameterization of peatlands and forestlands for a basin-scale simulation of surface-subsurface water flow, in the northern Athabasca River Basin in Canada. They used this model to identify the cause of higher annual downstream flow rates compared to upstream.

El-Zehairy et al (2018) used the MODFLOW-NWT code (MODFLOW with a new Newton (NWT) solver) to characterize the dynamics of transient interactions between artificial lakes and groundwater. They showed that, due to large and fast man-induced changes of lake stages, the interaction of artificial lakes and groundwater is not mainly driven by natural forces (for example precipitation and evapotranspiration) but by a transient balance between river inflow and outflow. They concluded that the study of dynamics between artificial lakes and groundwater requires a fully-coupled model that accounts for variably-saturated flow and for the spatio-temporal variability of water exchange between the surface and subsurface.

Integrated models also create a useful framework to simulate observed catchment behaviour and test future scenarios and potential hydrologic behaviours. For example, Huo et al. (2016) developed an interactive interface between the Soil and Water Assessment tool (SWAT) and MODFLOW to couple surface water-groundwater flow. They applied the integrated model to study the effect of future climate change on river runoff in the Xi'an Heihe River basin, China.

Yang et al. (2015) used HGS to investigate a 3D heterogeneous coastal aquifer of the Weser river estuary in the German Bight. They studied the long-term impact of climate change considering interactions between mean sea level rise, river discharge variation into the sea estuary and increases of storm surge intensity that induce seawater overtopping. Furthermore, they utilized the software package PEST (Doherty et al., 2010) for the steady-state calibration. Results showed a rise in groundwater level, as well as the creation of surface water ponding and shifts in salinized areas. Moreover, discharge canals cause the seawater to flow further inland by providing pathways for water flow.

Thompson et al. (2015) used an empirical dataset to develop numerical models capable of representing the dominant hydrologic processes, and addressed how catchment hydrology within a complex pond-peat land region is influenced by the configuration of landscape units. They developed 2D models in HGS to reproduce observed hydrologic responses to climate change and to evaluate the sensitivity of the system to changes in specified parameters and boundary conditions. Their results demonstrate a dynamic interaction between pond-peat lands, especially with frequent reversals in hydraulic gradients in response to rain events. Comparisons between simulated and observed hydraulic heads indicated that the models were able to provide a reasonable representation of the groundwater flow system. However, they suggested that neglecting freezing and thawing in the simulation can produce discrepancies in model outcomes, such as poor representation of hydraulic heads. Wetlands located at high elevations were shown to be heavily reliant on precipitation inputs and are particularly vulnerable to changes in climate.

Jutebring Sterte et al. (2018) used the MIKE SHE model to study the influence of catchment parameters and freeze-thaw processes on surface water-groundwater interactions. They showed that the landscape heterogeneity and sub-catchment characteristics play an important role in the catchment hydrological functioning.

Numerical simulations of coupled groundwater flow and heat transfer

Due to the emergence of advanced groundwater flow and heat transport models, the capability to simulate the subsurface thermal response to climate change in hydrologically complex environments has improved rapidly over the last decade. Harlan (1973) is credited for developing the first coupled groundwater flow and heat transport model that incorporates the effects of freezing and thawing. Painter (2011) presented a three-phase numerical

model, MarsFlo, for partially-frozen, partially-saturated porous media. MarsFlo accommodates the range of pressure and temperature conditions of interest in studies of the past or present hydrological system on Mars, which by appropriate input choice can be applied to Earth-related hydrological phenomena. MarsFlo uses the integral finite-difference method to discretize the conservation equations. The discretized air and water balance equations are then solved in a fully-coupled manner with the corresponding discretized energy balance equations. In order to validate the model, they used data from previously published laboratory experiments to probe both the underlying mathematical model and its numerical solution. The simulation demonstrated that the choice of spatial difference for the vapor diffusion term significantly affects the simulation behavior at the interface between an ice-saturated and a partially-saturated grid cell, which can lead to convergence failures for the air component. The simulation adequately reproduced the principal phenomenon observed in the experiment, which was freezing-induced water redistribution (cryosuction).

Sjöberg et al. (2013) applied MarsFlo in three warming scenarios to study trends of increasing minimum stream discharge and recession flow characteristics (in particular the recession intercept) across various geological settings of northern Sweden. The study showed that these two streamflow characteristics may not always respond to permafrost thaw. Indeed, they are rather different and potentially complementary in the information they provide with respect to permafrost thawing across the northern Swedish landscape. Minimum discharge occurs during the cold season and thus trends in minimum discharge mainly reflect changes in the deeper groundwater flow pathways under and around permafrost bodies, while changes in the recession flow will be more related to active layer dynamics. Although subsurface temperatures responded quickly to the surficial thermal perturbations, they noted that there was a delay in the melting of subsurface ice.

Another finite element code that has been widely used to solve partial differential equations in two or three dimensions is Flex PDE. This code was used, for example, by Bense et al. (2012) for catchments consisting of a series of linked sub-basins, to evaluate how representations of present-day permafrost conditions impact the evolution of groundwater recharge and discharge driven by permafrost degradation. They considered two scenarios with different initial permafrost and hydrogeological conditions. Their simulations showed that permafrost degradation shifts regional connectivity between basins and increases aquifer storage, which leads to modified space-time trends in groundwater regimes. In their study, the range of estimated increases in groundwater flow due to climate change was not

high. Therefore, permafrost thaw was in this case controlled by heat diffusion while advective heat flow did not accelerate permafrost degradation. They noted that heat advection can impact transient permafrost distribution when recharge is not limited by effective rainfall, when flow is strongly focused, or when geothermal heat flow anomalies occur. In their studied catchment, the initial distribution of permafrost and shifts in aquifer permeability architecture control the timing and circulation rate of groundwater in aquifers. An increase in sub-permafrost hydraulic head and uptake of water into aquifer storage delays the effects of permafrost degradation on increasing groundwater fluxes, possibly by several decades to centuries.

The U.S. Geological Survey model SUTRA is a coupled finite-element simulation model for saturated-unsaturated, fluid-density-dependent ground-water flow. A modified version of SUTRA was used by McKenzie and Voss (2013) to investigate the interaction between heat conduction and heat advection via groundwater flow with both seasonal ground ice and permafrost. They considered two climate change scenarios (i.e. +1 °C/100 yr and +6 °C/100 yr). By comparing the advection-influenced thaw rate and pattern with the case in which there is no groundwater flow, termed conduction-only, they concluded that the time needed for permafrost to disappear in the advection-influenced case was about one-third less than the time required for complete permafrost loss in the equivalent conduction-only system. For conduction-only thaw, the thinnest parts of the permafrost layer thawed first, which led to permafrost bodies persisting below hilltops. In contrast, the warm recharge water in advection-influenced thaw caused the permafrost to thaw mostly below hilltops with residual permafrost zones remaining in the valley. If the permafrost layer is initially discontinuous, with open taliks (unfrozen zones that are often formed by heat flowing from or towards surface water bodies or heated buildings, Kurylyk et al., 2014a) initially below valley surface-water bodies, the time for total thaw may be further reduced.

Briggs et al. (2014) used SUTRA to investigate mechanisms of permafrost aggradation around shrinking Arctic lakes focusing on ecological feedback. Their simulations demonstrated that emerging shrubs, as a result of lake recession and opening of meadow areas, reduce annual direct short-wave radiation to soil due to summer canopy shading. Furthermore, since shrubs intercept and take up water, they also diminish recharge infiltration (heat advection). They showed that a shrub-driven reduction in recharge has a much stronger effect on frost characterization when combined with summer shading.

However, they suggested that the new permafrost will eventually thaw based on climate projections.

The impact of climate change on the timing, magnitude and temperature of groundwater discharge was studied by Kurylyk et al. (2014b). They applied a modified version of the SUTRA model to small, unconfined aquifers that undergo seasonal freezing and thawing. The model included surface water and heat balance models and was run by applying downscaled climate scenarios to obtain future projections. The simulations show a potential rise in the magnitude and temperature of groundwater discharge to the adjacent river during the summer months as a result of projected increases in air temperature and precipitation. The thermal response of groundwater to climate change was shown to be dependent on the aquifer dimensions. Furthermore, the results indicated that the probability of exceeding critical temperature thresholds within groundwater-sourced thermal refugia (microhabitats for cold water fishes created due to spatially discrete groundwater discharge and induced riverine thermal heterogeneity) may significantly increase under the most extreme climate scenarios.

Another model in this group, HEATFLOW-SMOKER, is an advanced numerical model for solving complex density-dependent groundwater flow and heat transport problems (Molson and Frind, 2018). The model can be used for applications involving the storage or transport of thermal energy in the subsurface where temperatures remain < 100 °C, including advective-conductive heat transport with phase change and latent heat. The HEATFLOW-SMOKER model has been tested and applied to a variety of systems, including groundwater-surface water systems (Markle et al. 2004, 2006; Kalbus et al, 2007) and for simulating permafrost thaw (Grenier et al., 2018; Albers et al., 2020; Dagenais et al., 2020). Shojae Ghias et al. (2016) developed a 2D coupled water flow and heat transfer model with HEATFLOW/SMOKER to study the effect of climate warming on permafrost degradation at the Iqaluit airport, northern Canada. The model considered both advection and conduction processes. Their results showed that even though thermal advection was not negligible in their study area, thermal conduction was the controlling process for permafrost degradation. Dagenais et al., (2020) applied the model to a 2D cross-section of the Tasiapik Valley near Umiujaq, Quebec, where the discontinuous permafrost is rapidly thawing. They showed that advective heat transport played a critical role in permafrost thaw from above and below the shallow permafrost layer. In a parameter sensitivity analysis of the Dagenais model using PEST coupled to the HEATFLOW-SMOKER code, Albers et al. (2020) showed that thermo-

hydraulic parameters defining the surface and near-surface layers had the most influence on the cry-hydrogeological system behaviour.

Hu et al. (2018) developed a fully-coupled heat transport and groundwater flow model with COMSOL Multiphysics. They used the model to study heat transfer during artificial ground freezing with groundwater flow. They concluded that effective hydraulic conductivity and the saturation of unfrozen water control the heat transfer process during the phase change.

Painter et al. (2016) present what is likely one of the most advanced coupled models published to date. They applied the Arctic Terrestrial Simulator (ATS) code to integrate surface/subsurface simulation of thermal hydrology in a region with permafrost. They ran a 100-year 2D model and included phase changes, transitions among different states for the land surface, and topography. They suggest the need to reach an acceptable time step to make feasible large 3D decadal projections.

Current research needs

Groundwater supplies almost half of the global drinking water demand. The main question that motivated this research was to investigate how climate change would affect future availability of groundwater for northern communities. Since subsurface systems respond to climate change in a complex way, simulating this complexity requires a state-of-the-art integrated hydrologic model. Despite the available studies on simulations of coupled groundwater flow, heat transport and freeze-thaw processes in cold regions, most studies do not yet consider all relevant hydraulic and thermal processes. According to Ireson et al. (2013), one of the modelling challenges that need to be addressed is to couple the near-surface freeze-thaw cycles with the underlying unsaturated zone and saturated zone groundwater processes, as well as heat transfer by conduction and advection, taking into account phase change and latent heat during permafrost degradation. Furthermore, with the possible exception of the ATS model (Painter et al. 2016), mostly the existing models do not consider surface processes such as snowpack dynamics and surface water flow. Changes in topography due to thaw settlement of ice-rich permafrost, which provide feedback to surface processes and heat transfer at the air-ground interface, are also usually not considered. All these coupled processes are highly dynamic and nonlinear. Predictive accuracy can be limited due to nonlinearity of these coupled phenomena and the presence of natural feedback loops. For example, in an unsaturated zone, since thermal conductivity

increases with soil water content, flowing groundwater will promote heat transport and permafrost thaw. Thawing permafrost will release more water, which will in turn promote heat transport, creating a positive feedback loop. Moreover, as permafrost thaw may release sequestered carbon, it can exacerbate the rate of anthropogenic climate change (Tarnocai et al. 2009, Harden et al., 2012).

Even though there is increasing interest in exploring groundwater flow and heat transport, only a limited number of field investigations have focused on groundwater. Therefore, the current models have rarely been calibrated against field data. It is recommended that dedicated groundwater monitoring systems should be established to enable assessment of future climate impacts on groundwater (Bloomfield et al., 2013). The number of field investigations is particularly limited in cold regions, due to their remoteness and higher costs to perform these studies in such environments.

Research objectives and methodology

This study focuses on a small catchment near the Inuit village of Umiujaq in Nunavik, northern Quebec. One of the research needs identified for this study was calibrating the coupled water flow-heat transport model against field data in a cold region. The catchment selected for this study is in the discontinuous permafrost zone where detailed field investigations have been ongoing. The model is calibrated using field data. Field investigations have focused on characterizing the hydrogeological and thermal regimes and they provide valuable observations that can be used to calibrate complex numerical models.

The main aim for this study is to develop and apply a 3D integrated thermo-hydrogeological model to the cold-region catchment of Umiujaq. It represents a unique application of a fully-integrated model to a catchment where a detailed hydrogeological characterization was available, as opposed to an application to a synthetic catchment. Furthermore, this work will address existing scientific gaps in coupled groundwater-heat transfer simulations.

Three objectives were defined for this project: a) investigate a new calibration method for simulating water flow in highly heterogeneous areas (chapter 3 and 4), b) identify spin-up strategies to obtain the initial condition for coupled groundwater flow and heat transfer models (chapter 5), and c) apply the model to the cold region of Umiujaq (chapter 6).

In this PhD project, the following tasks (numerical simulations) were accomplished:

1. Flow model calibration, including an assessment of different calibration strategies
2. Sensitivity analysis
3. Investigating spin-up strategies for heat transport simulations
4. Assessing the role of the unsaturated zone on heat transfer simulations and temperature changes in the subsurface

The following methodology was used to reach the research objectives. First, the existing geological model for Umiujaq (Fortier et.al, 2020) was used to generate the 3D conceptual model, which consisted of the 3D mesh and hydrogeological model. A numerical flow model was then developed based on the conceptual model, using the HydroGeoSphere code, which is a fully coupled surface-subsurface flow model designed to simulate the coupled water flow-heat transport process. The model included the key components of the hydrologic cycle, including precipitation, infiltration, surface flow, and groundwater flow. Heat transfer processes were then coupled to the water flow model to provide insight and understanding into subsurface thermal dynamics in the study area.

This project addresses some of the deficiencies noted in the previous hydrogeological studies of cold regions. These include coupling surface-subsurface flow in a 3D environment and including the effect of snowmelt and the unsaturated zone. Furthermore, the project benefits from access to detailed hydrogeological field data from a cold region environment, which has been a limitation in previous hydrogeological studies of cold regions.

The present thesis contains six chapters. Chapter 1 presents the study area, near Umiujaq, Canada, and a summary of field measurements. Chapter 2 describes the numerical code, used to simulate coupled flow and heat transport. Chapter 3 is a conference paper presented in GéoOttawa, 2017: 70 years of Canadian Geotechnics and Geoscience. Chapters 4, 5, and 6 present the simulations and results of this study. These chapters are written in the format of journal papers and they will eventually be submitted for publication. Because of the format, there is some repetition in these papers in relation to the site and numerical model description. The last chapter concludes this work and discusses perspectives and potential future research.

1 Study area

1.1 Location

The study area for this project is located in the Tasiapik valley near the village of Umiujaq in northern Quebec, Canada (56°32′N 76°33′W; Figure 1.1, Figure 1.2). The catchment covers an area of 2.23 km^2, within the discontinuous permafrost zone.

Figure 1.1 Location of Umiujaq in Canada (Google Maps,2019)

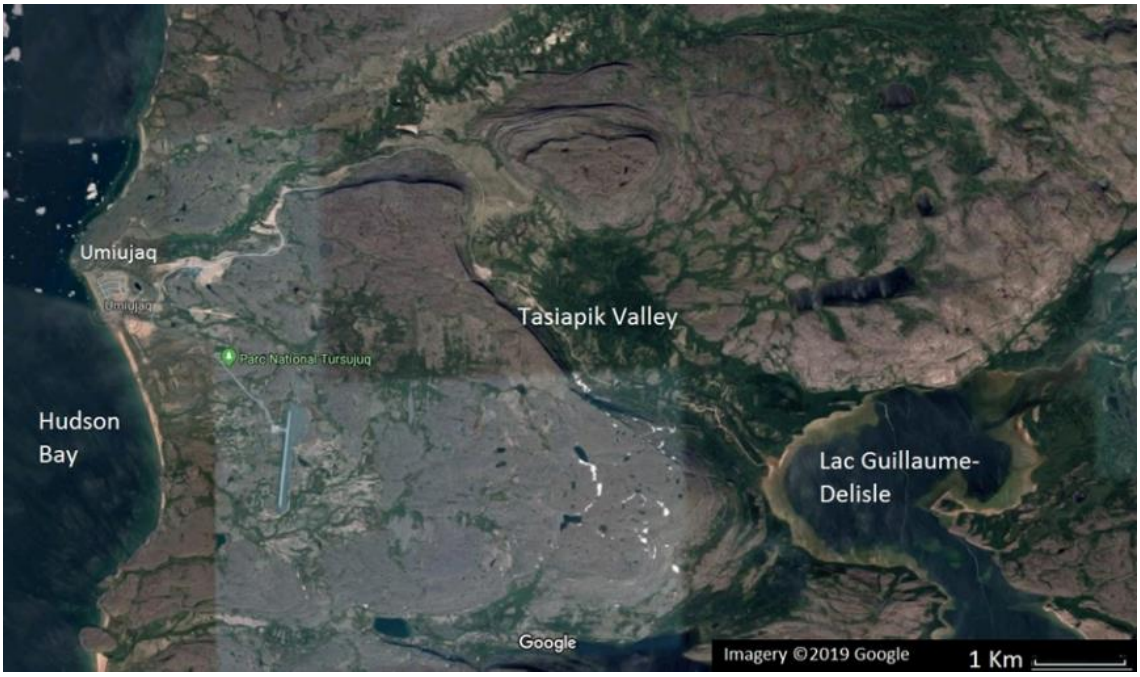

Figure 1.2 Location map of the study area in the Tasiapik Valley near the Inuit village of Umiujaq in northern Quebec

1.2 Geology and hydrogeology

Within the study area, six distinct hydrostratigraphic units were defined by LIDAR topographic surfaces, surface geophysical EM surveys and borehole logs (Figure 1.3). An elevation difference of 100 m exists between the flat downstream part of the valley and the relatively flat upstream area. In the upper reaches of the valley, the surface layer is a thin layer of littoral and pre-littoral sediments, which contains a shallow, perched aquifer. Below this aquifer lies a layer of frost-susceptible silt, which is thinner in the upstream part and becomes thicker downstream. In the frost-susceptible silty marine unit, discontinuous permafrost mounds can be seen in the cross-section, especially where the silty layer is thicker. The silt layer overlies the layers of subaqueous fluvioglacial sediments (Gs) and frontal moraine deposits (Gxt). Units Gs and Gxt form a deeper aquifer that is unconfined in the upper part of the valley and confined in the lower part.

In this subarctic region, permafrost mounds are discontinuous but widespread. The permafrost mounds in the Tasiapik valley are characterized by an oval or approximately circular shape, 3 to 4 m higher than the surrounding terrain, as a result of frost heave, and

they are about 50 m in diameter. The active layer, less than 2 m thick, is the surficial layer of the permafrost mound. The permafrost base is about 22.5 m deep (Leblanc et al., 2006).

The catchment has a river system that is mainly intermittent except for the main stream. The vegetation cover varies according to the level of drainage. High topographic and well-drained zones in the upstream part of the watershed contain lichen vegetation, whereas convex topographic areas contain shrubs. Spruce vegetation is found in well-drained sites in the southeast part of the watershed and herbaceous plants are found near bodies of water (Provencher-Nolet, 2014).

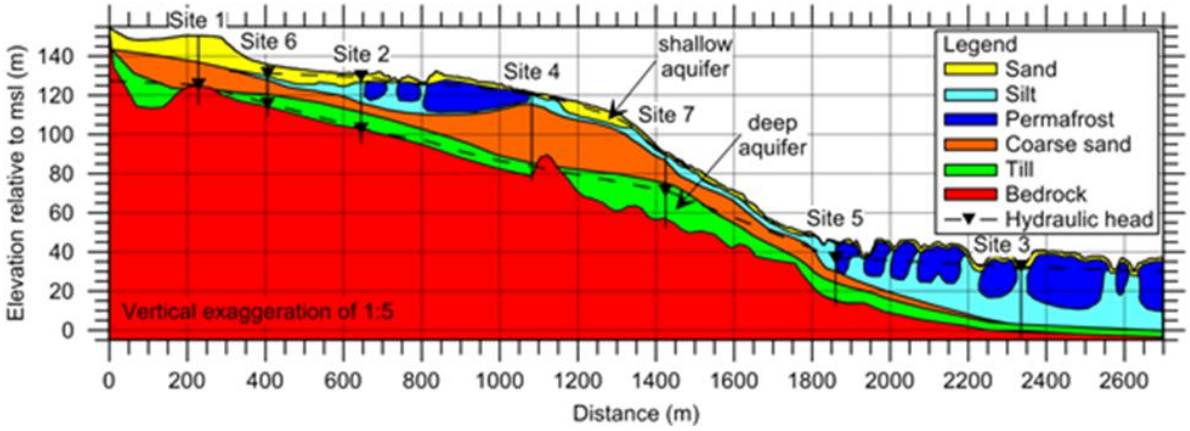

Figure 1.3 Cross-section of the study area along the valley axis showing 6 distinct hydrostratigraphic units

1.3 Climate

The regional climate of the study site is subarctic with cool and damp summers, and relatively dry and cold winters. Hudson Bay has a major influence on the regional climate due to strong winds in winter over the frozen bay and due to frequent dense fog in summer. A weather station in the catchment measures wind speed, air temperature and precipitation (Figure 1.4). Figure 1.5 shows measured air temperature, precipitation, and land surface temperatures from 2014-05-01 until 2017-05-01. Generally, the cold season occurs between October and May, and above-zero temperatures occur from May to September. The mean annual air and land surface temperatures for this period were -4.5 and 0.6 °C, respectively. The mean annual precipitation between 2014 and 2017, including rain and snow, was 760 mm.

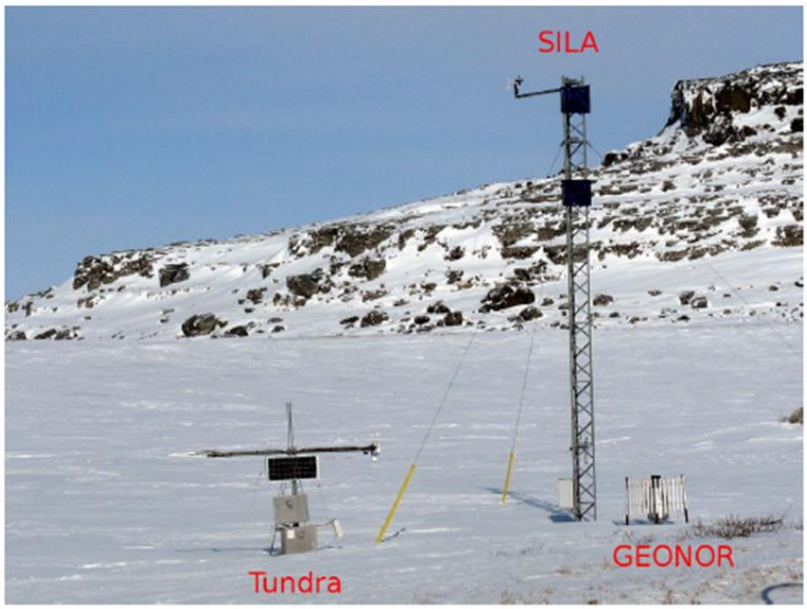

Figure 1.4 The weather station in Umiujaq (Barrère, 2018)

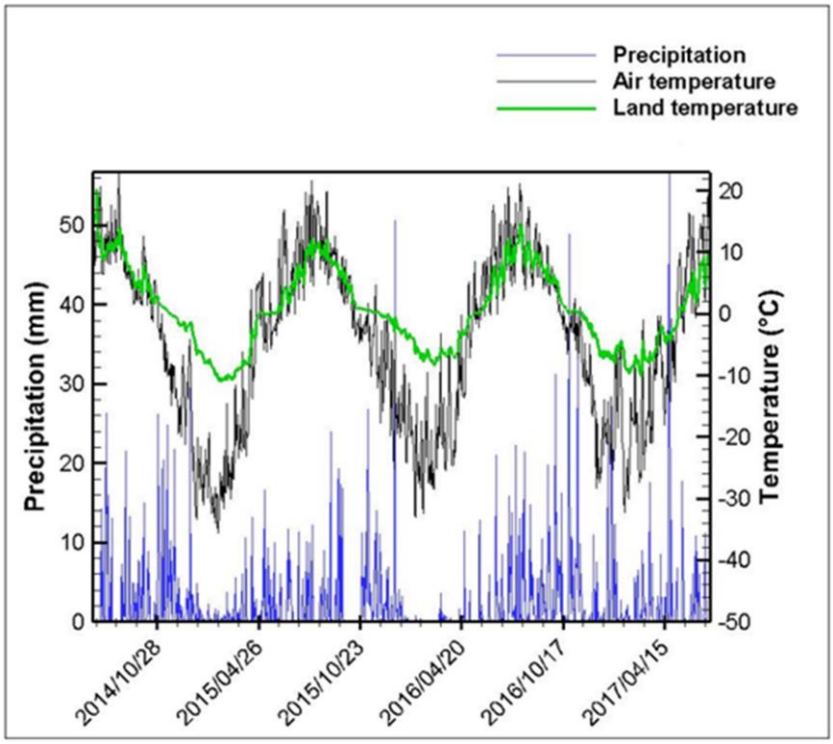

Figure 1.5 Measured precipitation, land and air temperatures at Umiujaq from July 2014 to July 2017

1.4 Field investigations and observed data

The hydrology of the catchment has been under investigation since 2013. The physical properties of the geological materials such as hydraulic and thermal conductivities, porosity, and specific heat capacity were measured in the field (Murray 2016, Dagenais 2018). Furthermore, meteorological conditions such as precipitation, thickness of snow cover, and air temperature have also been regularly measured. Several observation stations have been installed in the valley (Lemieux et al. 2020), including a gauging station located at the outlet of the watershed, which quantifies surface runoff in the basin, seven observation boreholes that measure the groundwater level throughout the valley, and 3 temperature stations that measure the temperature profile down to 35 m in depth (Figure 1.6). Furthermore, the land-surface temperature has been monitored with 38 probes installed at a depth of 10 cm throughout the catchment (Figure 1.7). The location of the surface-temperature probes was chosen to include different conditions in the catchment that could affect thermal behaviour, including type of vegetation, depth of snow cover and soil type. Field investigations in the catchment have also included the study of hydro-geochemistry (Cochand et al. 2020). Table 1.1 summarizes the available data from the field investigations.

Table 1.1 Available data provided through field investigations

Category	**Data**	**Source of Data**
Geological	Thickness of sediments Distribution of sediments Water table elevation and location Permafrost location and thickness	Geophysics (Resistivity)
Hydrogeological Data	Physical properties (K, θ) Water levels	Slug tests Grain-size or sediment type Observation boreholes
Thermal Data	Thermal conductivity Heat capacity Temperature depth profiles	Lab measurements Temperature probes Literature values
Hydro-geochemistry	Major ions, pH, isotopes	Surface-subsurface sampling

Meteorological	Air temperature Precipitation (rain, snow) Snow thickness	Meteorological stations

Banville (2016) and Fortier et al (2020) carried out a cryo-hydrogeophysical investigation of the study area and developed a 3D geological model using GOCAD, which delineated the boundaries of all hydrostratigraphic units in the study area (Figure 1.8). In the current study, grid elements of the numerical model were assigned properties based on this 3D geological model.

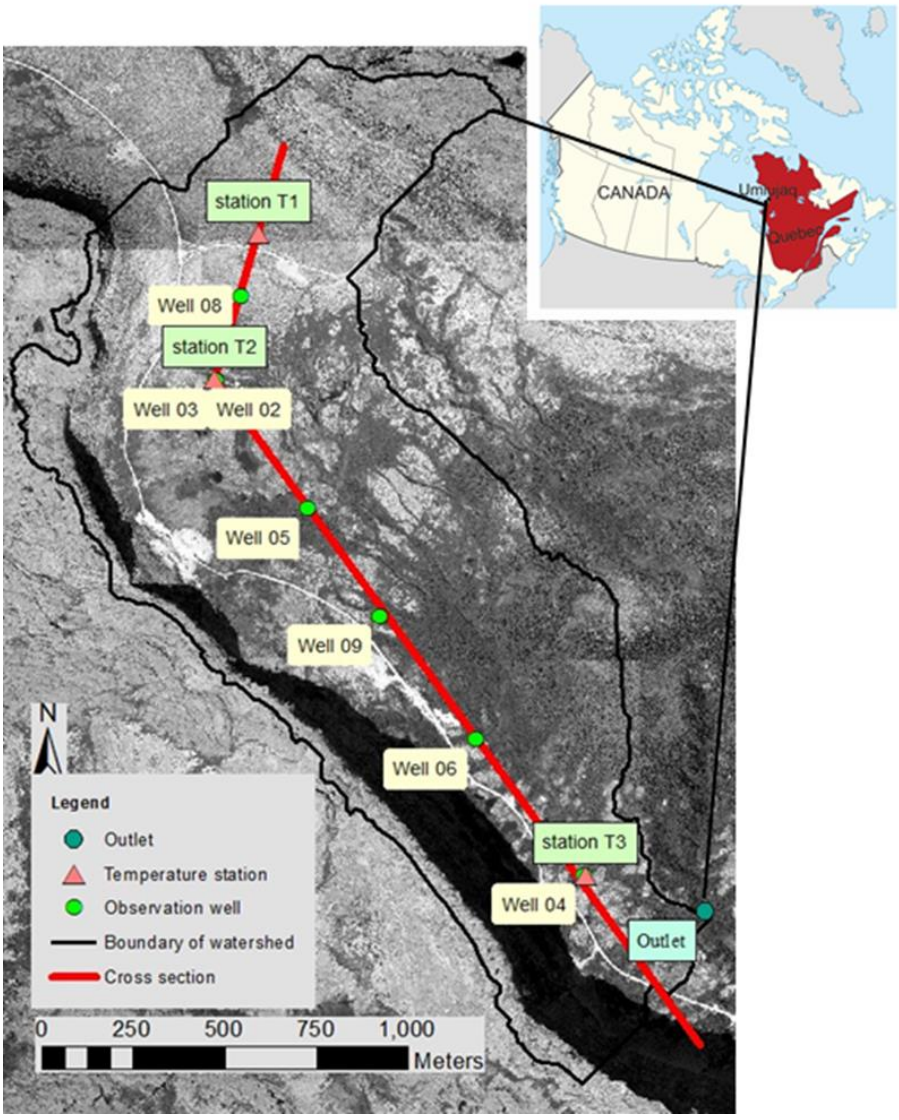

Figure 1.6 Observation stations in Umiujaq

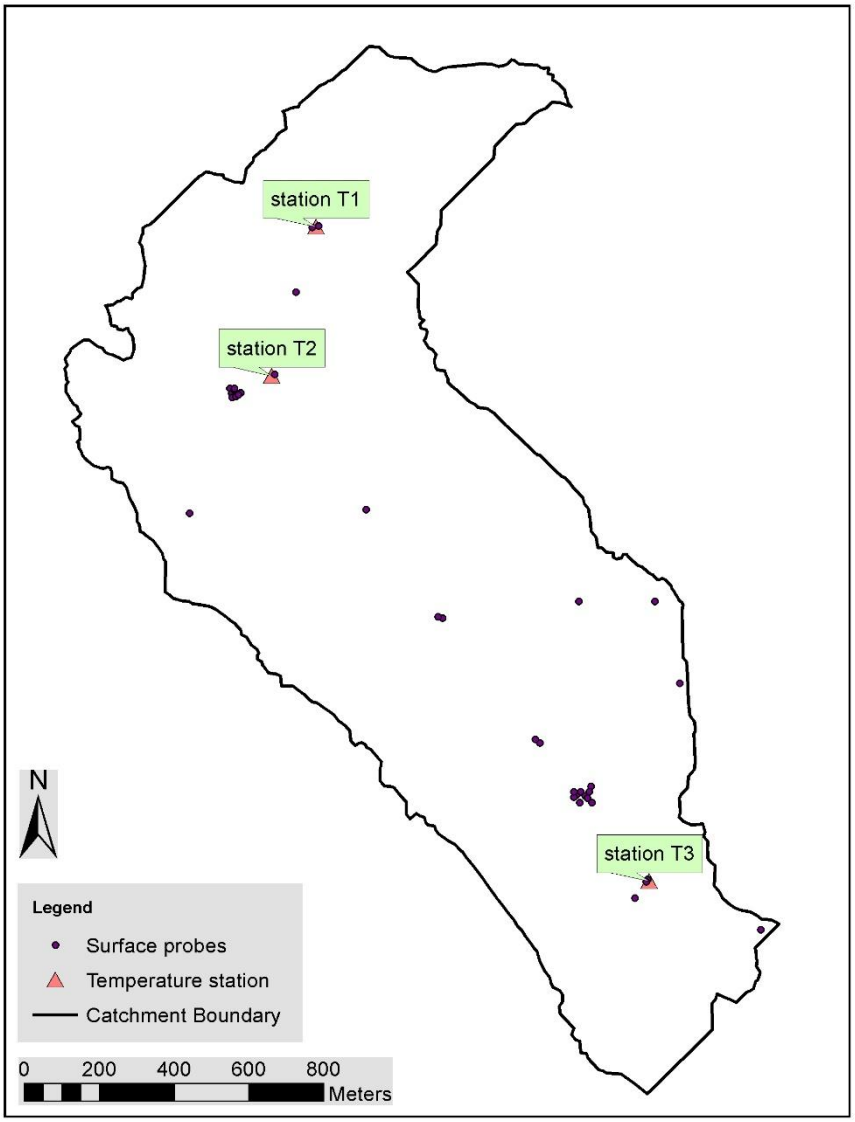

Figure 1.7 Instrumentation at the Umiujaq field site for thermal measurements: Thirty-eight probes are installed at depths of 10 cm to measure the ground surface temperature

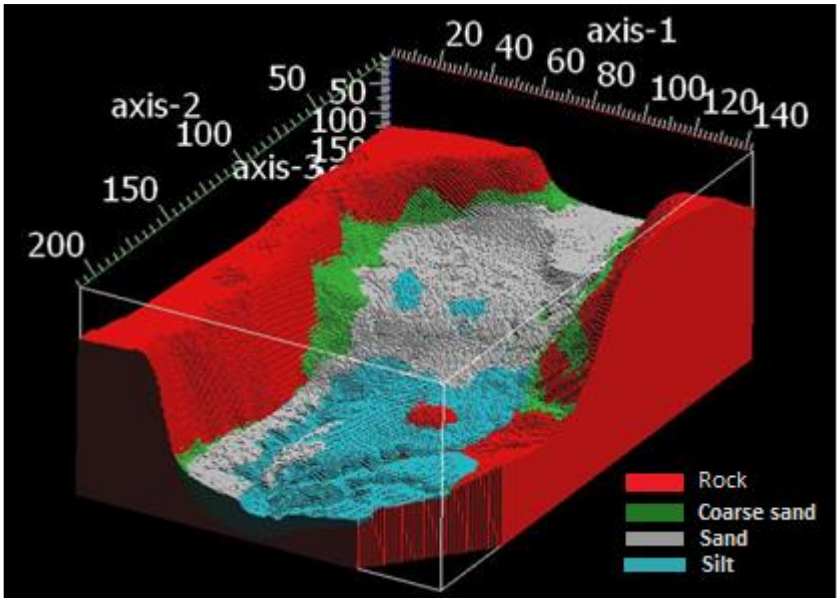

Figure 1.8 3D GOCAD geological model of the hydrostratigraphy in the Tasiapik Valley (Banville, 2016).

1.4.1 Precipitation measurement and processing

The weather station in Umiujaq (Figure 1.4) uses the Geonor T200-B precipitation gauge with an alter windshield to measure hourly precipitation (Smith, 2007). Systematic biases in measurements include wind-induced under-catch, wetting loss, evaporation loss and underestimation of trace precipitation amounts. For example, turbulent airflow over the gauge can prevent precipitation from falling into the bucket, which results in an under-estimation of true precipitation. Wind turbulence, in particular, affects snow catch in the bucket, since snow has lower density and falling speed. Therefore, treatment of the data is sometimes necessary to correct the precipitation (Goodison et al., 1998). In the course of this PhD project, the hourly precipitation measured by the Geonor T200-B gauge in Umiujaq was processed by applying the hourly relationship between wind speed and Geonor gauge catch efficiency. The methodology used to process the observed precipitation data is described here and the applied Matlab code and the steps are presented in Appendix 1.

Meteorological data used to process precipitation included hourly measures of air temperature, wind speed, and cumulative total precipitation. The Geonor T200-B unit at Umiujaq had only one vibrating wire until October 2015, when it was upgraded to include three vibrating wires, with which the instrument could record changes with a resolution of

0.1 mm at hourly intervals. The bucket is emptied twice each year and oil and antifreeze is added to melt frozen precipitation and minimize evaporation from the bucket.

1.4.1.1 Methodology

Measured precipitation at Umiujaq by Geonor T200-B was processed before being used in the numerical model. However, as it will be described in Chapter 4, processing of the precipitation data resulted in precipitation rates that were too high and not in agreement with climate conditions in Umiujaq. Therefore, in the end, the unprocessed precipitation data were used in the model. Nevertheless, the methodology used to process the precipitation data and the results are described in following sections.

1.4.1.1.1 Data pre-processing

The first step is to manually remove obvious outliers and eliminate the effect of gauge maintenance events like emptying the bucket and adding the oil. Subsequently, an automated filtering is needed to remove the effect of evaporation and sublimation (Duchon, 2008). For automatic filtering, a “brute-force” filtering algorithm is used to eliminate negative and small positive values by aggregating them with the nearest positive value, above the specified threshold (Pan et al., 2016). Here a threshold of 0.1 mm, which is the smallest value measureable by the device, is considered as the lowest acceptable measurement and all values below 0.1 mm were eliminated by aggregating them with the nearest acceptable positive value. The “brute-force” filtering algorithm consists of three steps. In the first step, the hourly precipitation, as the difference between consecutive values, is calculated from the cumulative time series recorded by the device. In the next step starting from the lowest off-threshold value, all values below the specified threshold were combined with the nearest positive values and then set to zero. This filtering algorithm assumes that the total cumulative precipitation is correct; therefore, at the end of the filtering process the total cumulative precipitation should be same for the initial and corrected data.

1.4.1.1.2 Correcting for under-catch of precipitation

The catch efficiency of a gauge with an alter wind shield has been shown to decrease with increasing wind speed, resulting in an under-catch of precipitation (Smith 2007). These biases in precipitation measurements are more evident in winter, since snow particles are less dense and their falling speed is lower than liquid precipitation. Therefore, a correction

for wind-induced biases is necessary to obtain more realistic precipitation values. A solid precipitation measurement inter-comparison was organized by the WMO in 1985 to introduce a reference method of solid precipitation measurement and to calibrate precipitation gauges (Goodison et al., 1998). Smith (2007) used the reference method recommended by WMO using the Geonor T200-B with an alter windshield to obtain the following empirical relationship between catch efficiency and wind speed:

$$P_{cor} = P_{obs}/CE \qquad CE = 1.18e^{-0.18W_s} \tag{1-1}$$

where P_{cor} (mm) is the corrected precipitation, P_{obs} (mm) is the measured solid precipitation after filtering, W_s (ms^{-1}) is the hourly mean wind speed at the gauge height, catch efficiency (CE) is the ratio of the Geonor catch to the "true" snowfall measured by a WMO reference called the double-fence inter-comparison reference (DFIR) (Goodison, et al., 1998). According to Smith (2007), this correction is applicable to a relatively cold, dry, and windy environment such as the Canadian prairies and arctic. Accurate snowfall observations are required in near real time. This relationship for CE is obtained for hourly measured precipitation. Therefore, in this project, an hourly timescale is used for the precipitation, wind and temperature measurements.

For a Geonor T200-B located in an open site with short grass:

$$W_s(h) = W_s(H)\left[\frac{Ln\left(\frac{h}{z_0}\right)}{Ln\left(\frac{H}{z_0}\right)}\right] \tag{1-2}$$

where $W_s(h)$ and $W_s(H)$ are wind speed at gauge height (m/s) and wind speed measured by an anemometer (m/s), respectively, h and H are the elevation of the Geonor (1.75 m) and the elevation of the anemometer (10m), respectively, and z_0 is the roughness (m). It is assumed that the shrubs are completely covered by snow in winter so the roughness is assumed equal to 1 mm for the snow period ($T_a < 0$) and one-tenth of shrub height (2 cm) for the warm period ($T_a > 0$).

For rainfall, a CE of 95% was measured for the Geonor instrument, relative to the WMO reference pit gauge for rainfall inter-comparison. Therefore, the wind biases for rainfall have not been considered here, and the data were corrected only for snowfall.

To avoid over correction, a maximum threshold for wind speed has to be assigned. For daily precipitation total, a maximum daily mean wind speed of 6.5 m/s is often applied in Arctic and northern regions (Yang *et al.*, 2005). Furthermore, according to Smith (2007), the CE for the Geonor with an alter shield remains equal to 1 at wind speeds up to 1.2 m/s. This is due to elimination of wind turbulence by the shield. Determination of precipitation type is also required for the bias correction algorithm for precipitation measurements, which can be done either by using a specific temperature to separate rain and snow, or by using a specified threshold to also include the mixed rain-snow type. Barrère (2018) has compared two methods for Umiujaq: 1) considering a temperature threshold of 1 °C to distinguish between rain and snow, and 2) including mixed rain and snow for temperatures between 0 and 2°C. However, the resulting cumulative precipitation did not show a significant difference between the two approaches. Therefore, a temperature threshold of 1 °C has been used in this study to separate rain and snow.

1.4.1.2 Results

Measured precipitation by the Geonor T200-B gauge can include noise in the time series. Sources of such noise include electromagnetic disturbances, irregular diurnal drift due to turbulent pressure fluctuations and temperature effects on gauge transducers (which is more evident during cold periods), and an evident decline in accumulation due to evaporation losses (Pan et al., 2016). This noise was removed by applying the filter described in the previous section. Figure 1.9 shows an example of noise in the cumulative precipitation data and corresponding filtering. Although the filtering process can create artificial rainfall events or can remove real events, it will preserve the total accumulation in a year.

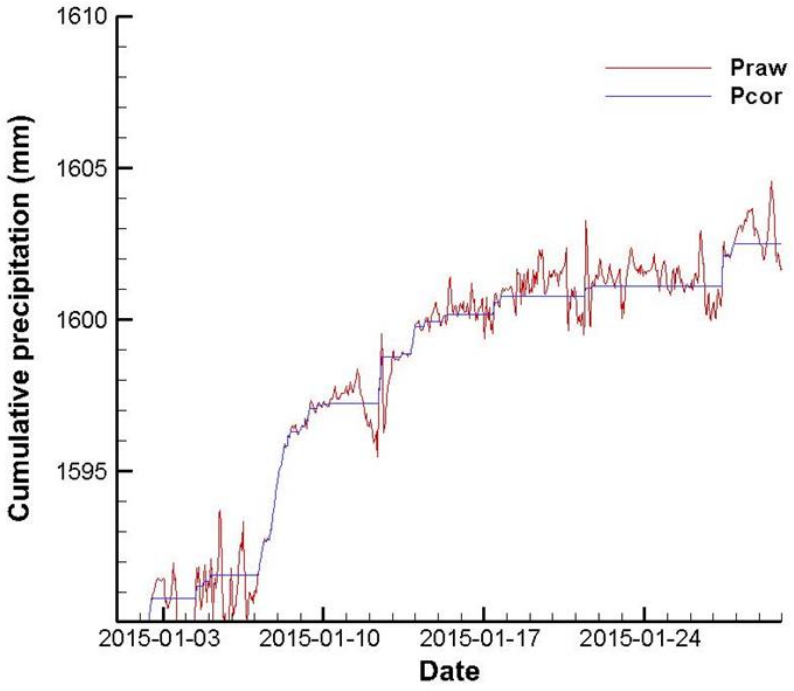

Figure 1.9 Effect of automated filtering to eliminate the effect of noise in the precipitation measurements

Figure 1.10 and Figure 1.11 show the monthly wind-induced bias corrections and the corresponding meteorological summaries, respectively. In summer, when precipitation only occurs as rainfall, the observed and corrected precipitation values are equal since the catch efficiency is considered equal to 1 for rainfall (Figure 1.10). Higher wind speed tends to be correlated to colder weather in winter, which decreases the catch efficiency of the device (Figure 1.11). As a result, corrections can reach up to 198% or 71 mm in winter (Figure 1.10). Bias correction also changes the peak in the annual precipitation cycle from summer to winter. Generally, the largest corrections are for November and December, due to higher wind speed and low temperature.

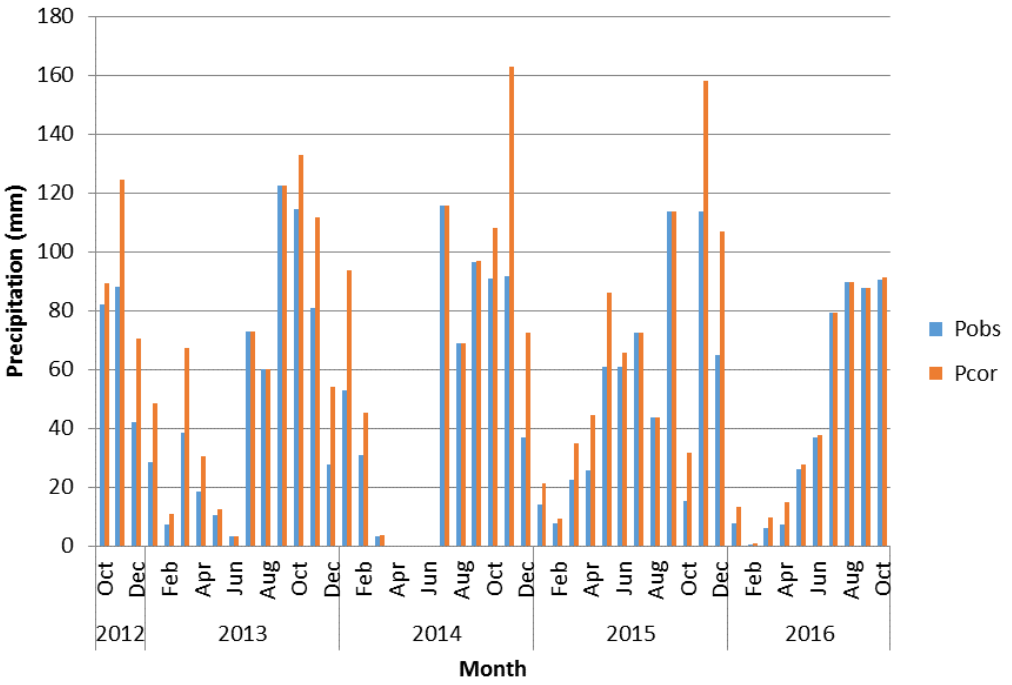

Figure 1.10 Monthly bias corrections in the precipitation data at Umiujaq

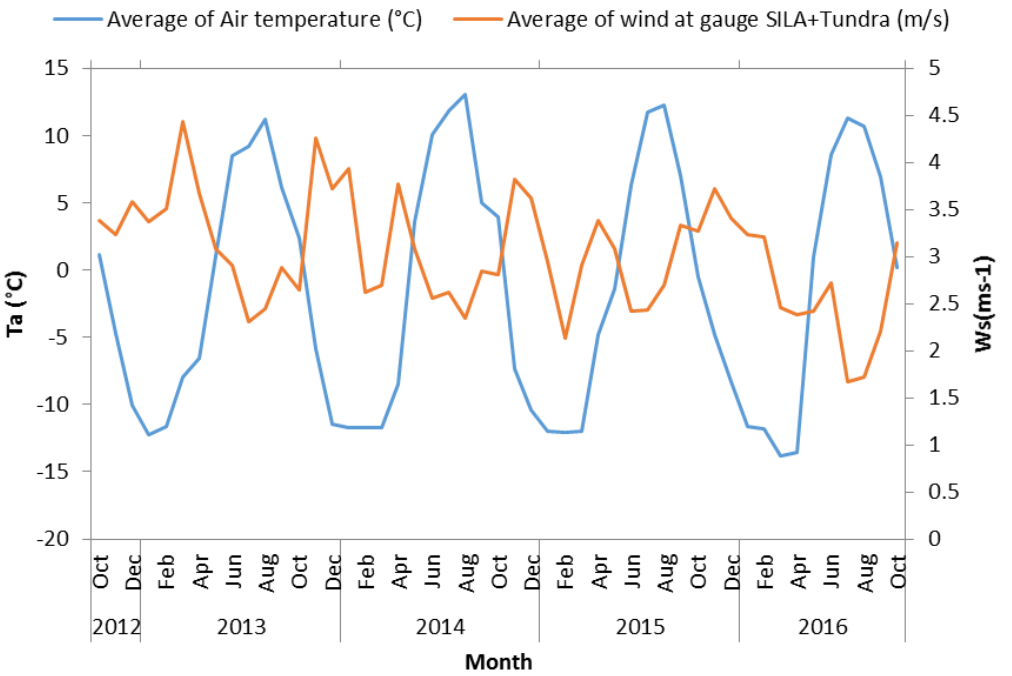

Figure 1.11 Average air temperature (Ta) and average wind speed at gauge height (Ws)

The frequency of observed hourly rainfall and snowfall is shown in Figure 1.12. To better highlight the lighter precipitation events, events over 5 mm/h, which occur less frequently, have been removed. The lighter precipitation events (<1 mmh^{-1}) occur more frequently than heavier precipitation. Also, heavier rainfalls happen more frequently compared to snow events.

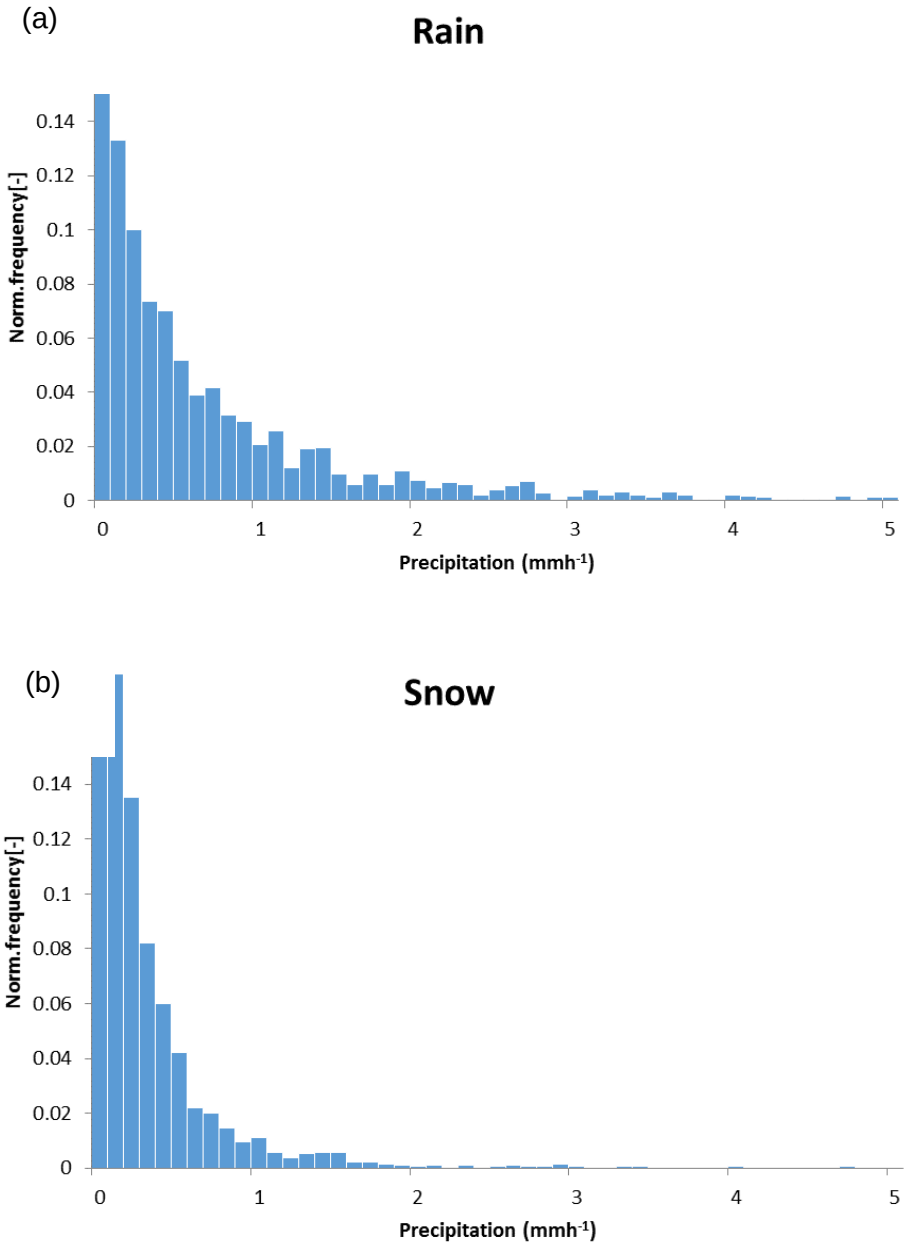

Figure 1.12 Histogram of hourly precipitation for a) Rainfall b) Snowfall

Another phenomenon that can affect measurement of snowfall is blowing snow, which is defined as snow lifted from the surface by the wind. Blowing snow can influence measurements in winter and quantifying its impact is challenging. Blowing snow fluxes collected by precipitation gauges are called false precipitation measurements (Pan et al, 2016). Blowing snow often occurs after continuous high wind speed (W_s >9.5 ms^{-1}) and may increase the volume of measured precipitation up to 50% (Bardsley and Williams, 1997). At this study site, the Geonor gauge is located in an open area. Therefore, the wind turbulence and blowing snow can influence the catch efficiency more than they affect devices with natural shielding of surrounding forests or bushes. Also, at Umiujaq, the elevation difference between the device and the top of the snow decreases in winter (Figure 3). Therefore, blowing snow can cause major errors in the measurements and a more detailed study is needed to quantify the magnitude of over-measurement caused by the blowing snow. Therefore, in this study, the effect of blowing snow is not considered in the processed precipitation.

Figure 1.13 shows the hourly wind speed measured at the weather station (see location in Figure 1.4). During the 2012-2016 period, wind speeds greater than 9.5 ms^{-1} were measured several times. When they occur in winter, these high winds can generate blowing snow that creates anomalous precipitation readings. From Equation 2-1, a high W_s results in a smaller value for CE, which will increaseP_{cor}. Therefore, if the measurement included this erroneous precipitation reading during blowing snow, the use of bias corrections for under-catch will even magnify errors caused by the blowing snow. An example of high wind speed and corresponding bias-corrected snowfall is provided in Figure 1.14 while the raw and corrected precipitation values are provided in Figure 1.15. During the winter, negative precipitation values were recorded by the device, which has reduced the total processed precipitation. These negative values were considerable during the winter of 2014.

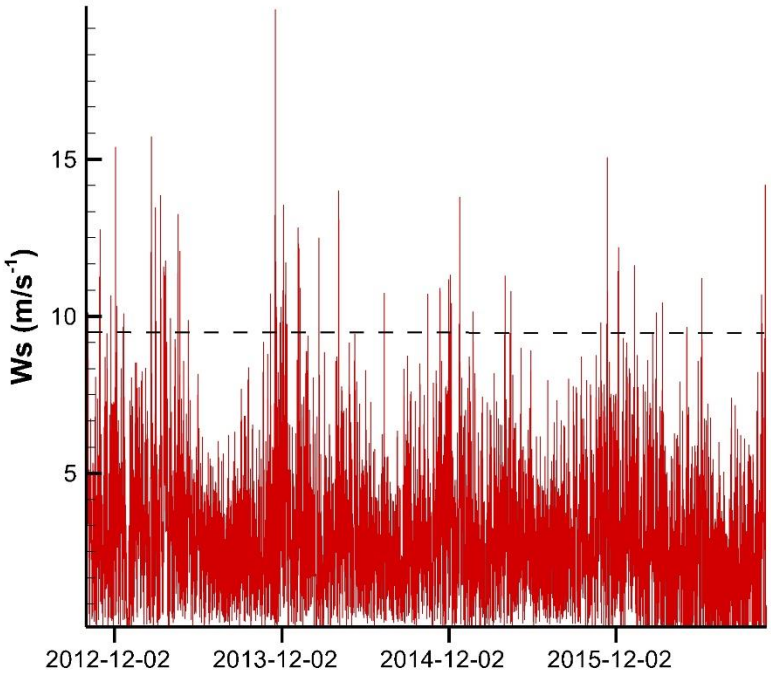

Figure 1.13 Observed hourly wind speed at gauge height

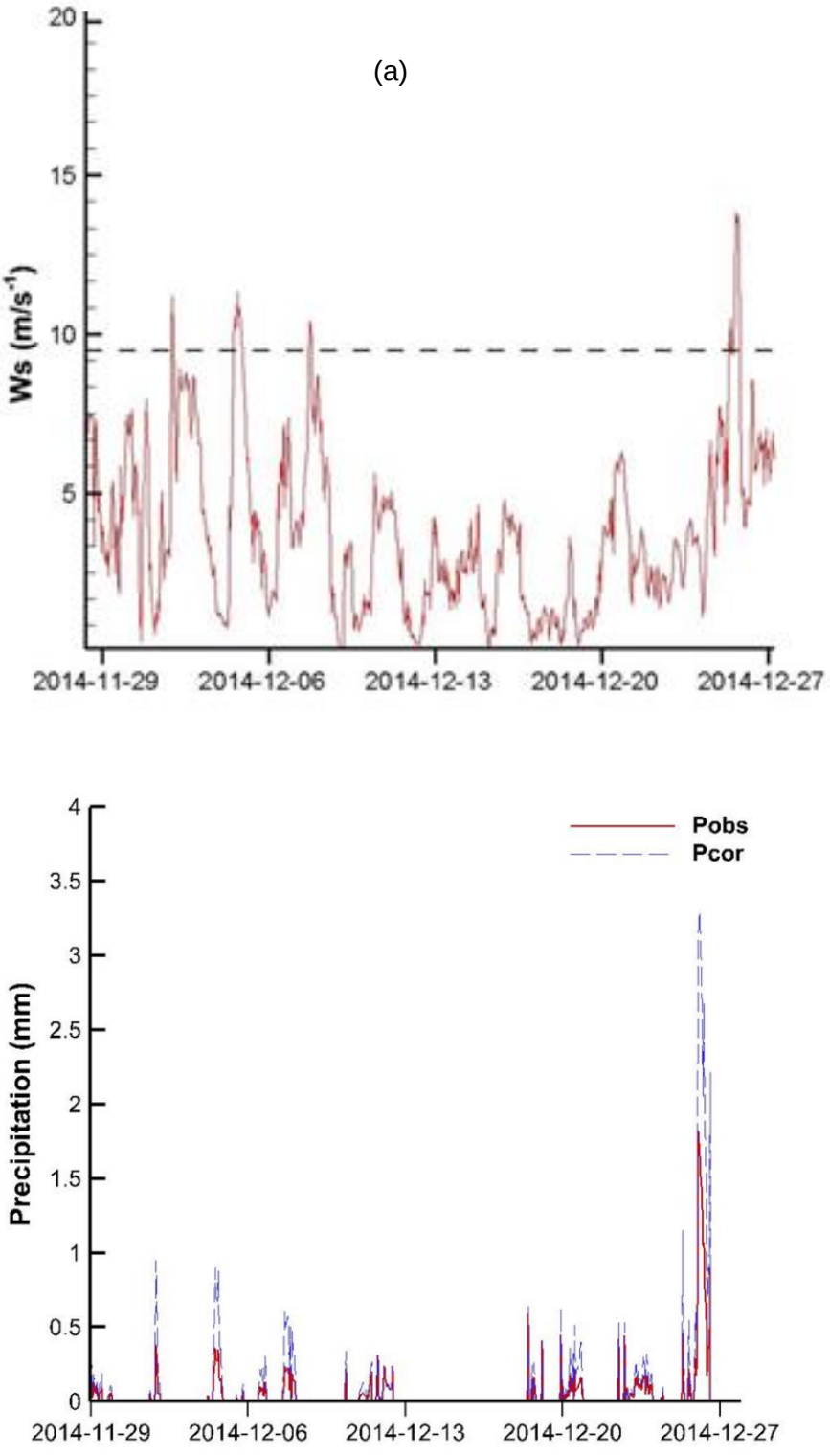

Figure 1.14 Example of effect of corrections on blowing snow. a) Wind speed b) Corresponding bias correction

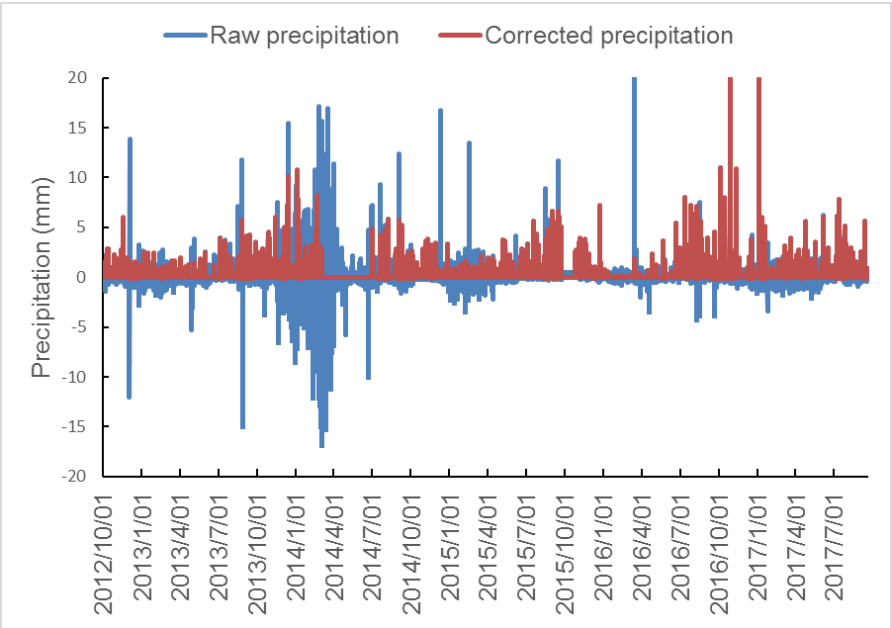

Figure 1.15 Raw and corrected precipitation at Umiujaq from October 2012 to October 2017

2 Numerical model

2.1 Introduction

HydroGeoSphere is a fully integrated, physically-based three-dimensional numerical model able to simulate subsurface, surface and drainage water flow, solute and heat transport (Therrien et al., 2010). HydroGeoSphere couples the two-dimensional, depth-integrated diffusion-wave approximation of the Saint Venant equation for surface water flow and Richards' equation governing 3-D unsaturated/saturated subsurface flow. For problems that also involve solute or heat transport, the classical advection-dispersion equation is used in all domains. A brief overview of the governing flow equations is presented in the following sections. A more detailed model description is available in Aquanty (2017).

2.2 Governing equations

2.2.1 Subsurface flow

The basic equation that HGS uses to model three-dimensional transient subsurface flow in a variably-saturated porous medium is the modified form of Richards' equation (Aquanty, 2017):

$$-\nabla.\left(\omega_m q\right)+\sum\Gamma_{ex}\pm Q=\omega_m\frac{\partial}{\partial t}\left(\theta_s S_w\right) \tag{2-1}$$

where ω_m (dimensionless) is the volumetric fraction of the total porosity of the porous medium. In equation (2-1), S_w (dimensionless) and θ_S (dimensionless) are the degree of water saturation and the saturated water content, respectively, t is time (T), Q ($L^3L^{-3}T^{-1}$) represents a source/sink and Γ_{ex} ($L^3L^{-3}T^{-1}$) is the volumetric fluid exchange rate between the porous medium and other flow domains. In equation (2-1) q (T^{-1}) is the fluid flux, which is defined as:

$$q=-K.k_r\nabla\left(\psi+z\right) \tag{2-2}$$

where $k_r = k_r(S_\omega)$ is the relative permeability of the medium, $\psi\ (L)$ is the pressure head and $z\ (L)$ is the elevation head. The hydraulic conductivity tensor $K\ (LT^{-1})$ is given by:

$$K = \frac{\rho_w g}{\mu} k \tag{2-3}$$

where g, ρ_w, μ and k are the gravitational acceleration (LT^{-2}), the density of water (ML^{-3}), the viscosity of water $(ML^{-1}T^{-1})$, and the permeability of the porous medium (L^2), respectively.

Compressibility effects on storage of water are negligible compared to the effect of changes in saturation, in unsaturated conditions. The storage term in equation (2-1) can then be defined as:

$$\frac{\partial}{\partial t}\left(\theta_s S_w\right) \approx S_w S_s \frac{\partial \psi}{\partial t} + \theta_s \frac{\partial S_w}{\partial t} \tag{2-4}$$

where (S_S) is the specific storage coefficient of the porous medium (L^{-1}).

The previously mentioned basic equation can be expanded to include other features, such as discrete fractures, wells, tile drains and surface flow.

2.2.2 Surface flow

A diffusion-wave approximation of the Saint-Venant equation for surface water flow is solved in HGS. A simplified form of the full two-dimensional Saint-Venant equation solved by HGS is as follows (Aquanty, 2017):

$$\frac{\partial \varphi_o h_o}{\partial t} - \frac{\partial}{\partial x}\left(d_o K_{ox} \frac{\partial h_o}{\partial x}\right) - \frac{\partial}{\partial y}\left(d_o K_{oy} \frac{\partial h_o}{\partial y}\right) + d_o \Gamma_o \pm Q_o = 0 \tag{2-5}$$

where K_{ox} and K_{oy} are surface conductances (LT^{-1}) that depend on the equation used to approximate the friction slopes, d_o is the depth of flow (L), h_o is the water surface elevation (L), t is time (T), $Q_o\ (L^3L^{-3}T^{-1})$ is a volumetric flow rate per unit area representing external sources or sinks φ_o is the surface flow domain porosity depending on rills and obstructions, and Γ_o is the water exchange between the surface and subsurface systems.

The two flow domains are coupled through the exchange term $\Gamma_o$with:

$$d_o \Gamma_o = \frac{k_r K_{zz}}{l_{exch}} (h - h_0) \quad (2\text{-}6)$$

where $k_r$is the relative permeability of the exchange layer, K_{zz} is the vertical saturated hydraulic conductivity, and $l_{exch}$is the coupling length (L).

2.2.3 Heat transport

The fully-integrated feature of HydroGeoSphere makes it an ideal choice for integrating the heat transport system. The model includes heat transport in both the surface and subsurface domains. Surface heat fluxes from atmospheric inputs are incorporated into HydroGeoSphere. The general equation for variably-saturated subsurface heat transport is (Molson, 1992 and Aquanty, 2017):

$$\frac{[(\partial c_b T)]}{\partial t} = -\nabla[q\rho_\omega c_\omega T - (k_b + \theta_s S_w c_w \rho_w D)\nabla T] \pm Q_T + \Omega_o \quad (2\text{-}7)$$

where c is the specific heat capacity, T is the temperature of the bulk porous medium (assuming local thermal equilibrium between the fluid and grains, k_b is the thermal conductivity, D is the hydrodynamic dispersion, Q_T is a thermal source/sink and Ω_o is the thermal surface/subsurface interaction term. The subscript b denotes a bulk term, whereas ω represents the aqueous phase. The Darcy flux (q) in the subsurface is calculated from a numerical solution of the mixed form of Richards' equation, which is valid both above and below the water table, and the water saturation term is included in each of the bulk property terms.

Heat transport in surface water is described by the following equation (Aquanty, 2017):

$$\frac{[(\partial \rho_\omega c_\omega d_o T_o)]}{\partial t} = -\nabla[q_o \rho_\omega c_\omega T_o - (k_\omega + D_o c_\omega \rho_\omega) d_o \nabla T_o] + E_{atm} \pm Q_{T_o} - d_o \Omega_o \quad (2\text{-}8)$$

where E_{atm} represents the atmospheric inputs to the surface thermal energy system, and subscript o denotes overland (or stream) flow. The overland water flux (q_o) is calculated from the numerical solution of the diffusion-wave equation, together with Manning's equation.

The total atmospheric input to the surface thermal energy system can be expressed as:

$$E_{atm} = K_* + L_* + Q_H + Q_E \quad (2\text{-}9)$$

where K_* is the net shortwave radiation, L_* is the net longwave radiation, Q_H is the sensible heat flux and Q_E is the latent heat flux.

More details on the governing equations are presented in Aquanty, (2017).

2.2.4 Solution procedure

HydroGeoSphere uses the control volume finite element method to solve either a set of linear equations (for fully-saturated flow or solute transport) or non-linear equations (for variably-saturated subsurface flow, etc.). In HGS, the mass and heat transport equations are solved in a fully coupled fashion. To solve the non-linear equations, HGS applies the Newton-Raphson linearization method. This method is robust and has good convergence properties. The matrix equations are implicit and are solved at each non-linear iteration until convergence.

2.2.5 Simulation of winter processes in HydroGeoSphere

In HGS, the governing equation is expanded to include both solid and liquid phase of water in the surface domain. In this application, precipitation is divided into liquid and solid phases, based on the air temperature. It is assumed that the solid phase snow is immobile. Therefore the flow equation is described as:

$$\frac{\partial}{\partial \mathrm{t}}(\rho_{\mathrm{w}} \mathrm{d}_{\mathrm{wv}} + \rho_{\mathrm{snow}} \mathrm{d}_{\mathrm{snow}}) = \frac{\partial}{\partial \mathrm{x}}\left(\rho_{\mathrm{w}} \mathrm{d}_{\mathrm{f}} \mathrm{K}_{\mathrm{ox}} \frac{\partial \mathrm{h}_{\mathrm{o}}}{\partial \mathrm{x}}\right) + \frac{\partial}{\partial \mathrm{y}}\left(\rho_{\mathrm{w}} \mathrm{d}_{\mathrm{f}} \mathrm{K}_{\mathrm{oy}} \frac{\partial \mathrm{h}_{\mathrm{o}}}{\partial \mathrm{y}}\right) + \rho_{\mathrm{w}} \mathrm{Q}_{\mathrm{o}} - \rho_{\mathrm{w}} \Gamma_{\mathrm{ex}} + \rho_{\mathrm{snow}}(\mathrm{q}_{\mathrm{snow}} - \mu) \tag{2-10}$$

where q_{snow} and μ_{snow} are the rates of snow precipitation and sublimation per unit surface area ($L^3T^{-1}L^{-2}$), respectively. The depth of snow is determined by snow precipitation, sublimation and melting by temperature change:

$$\frac{\partial}{\partial \mathrm{t}}(\rho_{\mathrm{snow}} \mathrm{d}_{\mathrm{snow}}) = \rho_{\mathrm{snow}}(\mathrm{q}_{\mathrm{snow}} - \mu) - \rho_{\mathrm{snow}} \mathrm{q}_{\mathrm{melt}} \tag{2-11}$$

where the depth of snow is always positive and the rate of melting is assumed to be proportional to a constant (α) and to the difference between the air temperature (T_{air}) and threshold temperature ($T_{threshold}$) when $T_{air} > T_{threshold}$,or α=0 when $T_{air} \leq T_{threshold}$.

$$\rho_{\mathrm{snow}} \mathrm{q}_{\mathrm{melt}} = \alpha(T_{air} - T_{threshold}) \tag{2-12}$$

A detailed description of snowmelt processes in HGS is explained in the HGS manual (Aquanty, 2017) and in Schilling *et al.* (2019).

Some simplifying assumptions were used in the simulation. The general assumption includes not accounting for soil freeze-thaw cycles and the effect of latent heat in the simulations. Therefore, the variability of hydraulic and thermal conductivities of units due to freezing and thawing processes was not considered. The assumptions and simplification will be discussed in the following chapters in more detail.

3 An integrated surface-subsurface flow model of the thermo-hydrological behavior and effect of climate change in a cold-region catchment in northern Quebec, Canada

Masoumeh Parhizkar, René Therrien, John Molson, Jean-Michel Lemieux, Richard Fortier, Marie-Catherine Talbot Poulin & Pierre Therrien

Department of Geology and Geological Engineering – Université Laval, Québec, QC, Canada

Michel Ouellet

Ministère du Développement durable, de l'Environnement et de la Lutte contre les changements climatiques, Québec, QC, Canada

Conference paper presented at GeoOttawa 2017

Reference:

Parhizkar, M., Therrien, R., Molson, J., Lemieux, JM., Fortier, R., Talbot Poulin, MC. & Therrien, P., Ouellet, M. (2017) An Integrated Surface-Subsurface Flow Model of the Thermo-Hydrological Behavior and Effect of Climate Change in a Cold-Region Catchment in Northern Quebec, Canada. GeoOttawa 2017: the 70th Canadian Geotechnical Conference and the 12th Joint CGS/IAH-CNC Groundwater Conference, Canadian Geotech Soc, Ottawa, 1-4 Oct. 2017

3.1 Résumé

Trois modèles numériques d'écoulement des eaux souterraines avec différents degrés d'hétérogénéité spatiale ont été calés pour un petit bassin versant situé au Québec nordique, en zone de pergélisol discontinu. Pour le calage, le logiciel de modélisation inverse PEST a été couplé aux modèles d'écoulement de l'eau souterraine 3D en régime permanent développés avec HydroGeoSphere. Les modèles calés ont ensuite été utilisés pour des simulations en régime transitoire pour évaluer leur efficacité à prédire des séries chronologiques observées de charges hydrauliques. La comparaison des résultats en régime permanent montre que l'inclusion d'une plus grande hétérogénéité dans le modèle permet un meilleur ajustement aux observations moyennes sur le terrain. Les modèles hétérogènes peuvent reproduire de manière précise les séries temporelles pour les charges

hydrauliques dans les matériaux grossiers, dans une partie de la zone d'étude avec moins de pergélisol. Par contre, dans les parties de la zone d'étude avec plus de pergélisol, un calage supplémentaire est nécessaire pour inclure l'effet du pergélisol dans le système d'écoulement des eaux souterraines.

3.2 Abstract

Three numerical groundwater flow models with different levels of spatial heterogeneity were calibrated for a hydrogeological system located in a cold environment with discontinuous permafrost. Calibration was completed by coupling the inverse calibration code PEST to the 3D steady-state groundwater flow models developed using HydroGeoSphere. Results were then used in a transient model to assess the efficiency of calibrated models in predicting the observed time series of hydraulic heads. Comparison of steady-state results shows that by allowing more heterogeneity in the model, a better fit to average field observations can be achieved. Although heterogeneous models could accurately reproduce the time series for hydraulic heads in coarse materials in a part of the study area with less permafrost, in the parts of the study area with more permafrost, a more effective calibration approach is required which includes the effect of the permafrost in the groundwater flow system.

3.3 Introduction

Over the past decades, the availability of complex numerical models has allowed including heterogeneous system property distributions and complex processes such as coupled groundwater flow and heat transport. However, complex models are often difficult and time consuming to calibrate.

In one example, Ala-aho et al. (2015) calibrated hydraulic conductivity and anisotropy for an integrated surface water- groundwater model using the HydroGeoSphere (HGS) model. They reproduced the hydraulic head and stream baseflow distribution under transient and steady- state conditions. In a first step, they calibrated hydraulic properties in steady-state by using average recharge values. Vertical hydraulic conductivity and anisotropy were manually adjusted to find a combination that best fit the observed field values. Transient evapotranspiration (ET) dynamics and average annual ET rates were then used to calibrate the ET parameters in HGS.

PEST (Doherty 2016) is a software package for parameter estimation and uncertainty analysis of complex environmental models, which offers an efficient alternative to manual calibration. The uncertainty of highly parameterized models can be analyzed by the utilities provided for linear and nonlinear error-variance and uncertainty analysis.

Pilot-point calibration available through PEST has been used in many studies including Herckenrath et al. (2011), Yoon et al. (2013), and Doherty et al. (2010). Moeck et al. (2015) illustrated the application of the pilot-point based calibration method in a 2D steady-state model developed using HGS. They also used cross-validation and linear uncertainty analysis to validate alternative calibrated hydraulic conductivity distributions and to evaluate the importance of observations for parameter estimates.

In this paper, three methods are applied to calibrate the hydraulic conductivity in a 3D groundwater model for a watershed located in Umiujaq, northern Québec, Canada. This site is located in a discontinuous but widespread permafrost zone. In the first method, the porous medium is divided into 6 zones corresponding to 6 hydrostratigraphic units identified from field measurements and a single hydraulic conductivity is assigned to each zone. With only 6 hydraulic conductivity values, this first model is the simplest of the three. To include the effect of full heterogeneity in the evaluation, two additional heterogeneous models were developed by using pilot-points.

The 3D steady-state groundwater flow models were developed in HGS and were coupled to PEST using the method explained in Moeck et al. (2015). The average observed hydraulic heads in seven observation wells were used as the target values in PEST, which were compared to the steady-state model results. After calibrating the three models for steady state, transient models were created using the obtained calibrated models to evaluate the efficiency of each model in generating time series of hydraulic heads.

3.4 Study Area

The study site is a 2 km^2 catchment located on the eastern shore of Hudson Bay, northern Quebec, Canada. The watershed contains a discontinuous but widespread permafrost zone (Figure 3.1).

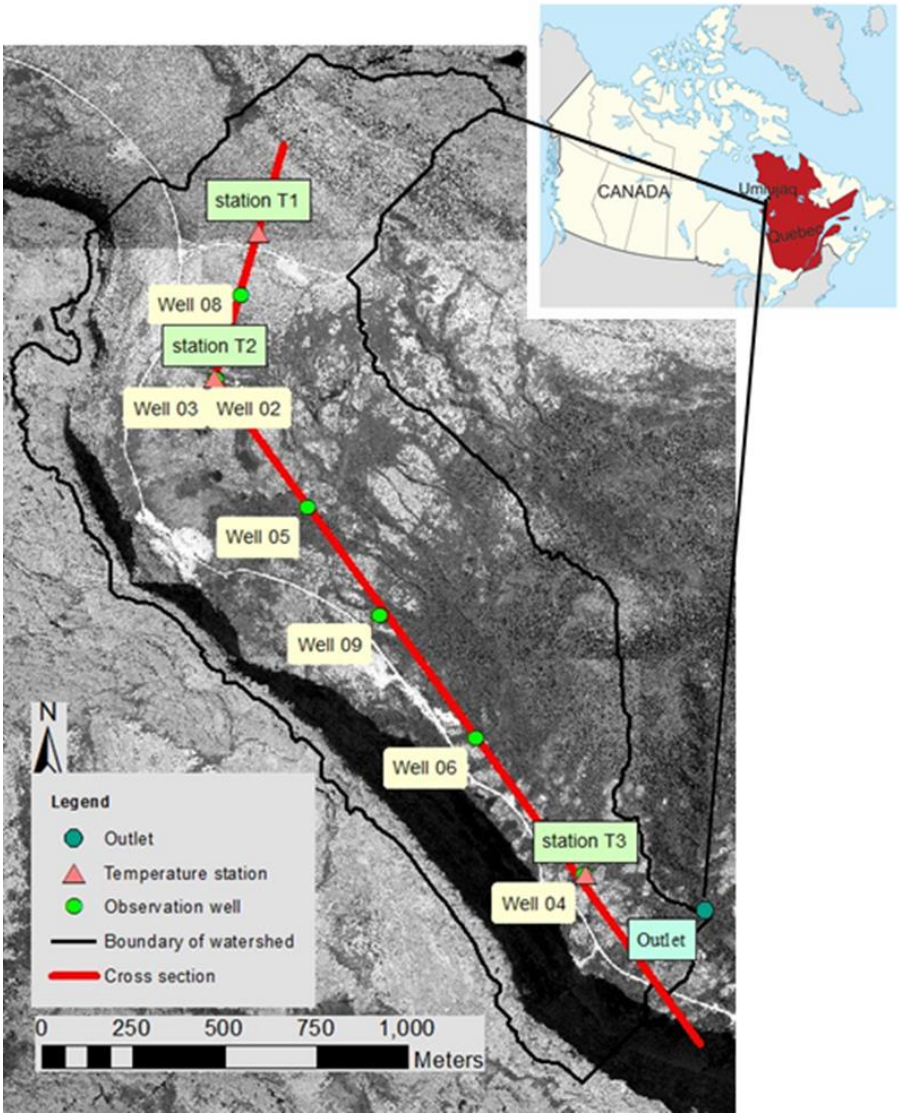

Figure 3.1 Areal-view of the study area, located in the Tasiapik Valley close to the village of Umiujaq. Seven observation wells along with 3 temperature stations and a stream gauge to measure the discharge at the outlet provide the observation data for the field.

The study area consists of 6 distinct hydrostratigrapic units defined by LIDAR topographic surfaces, surface geophysical EM surveys and borehole logs (Figure 3.2). The relatively flat upstream and downstream parts of the valley are offset by an elevation difference of 100 m and are connected by a relatively steep slope.

Discontinuous permafrost mounds are located in the silty layer, which is thicker in the downstream part of the valley and thus embeds more permafrost units. In this study area, field work has been carried out since 2013 to study the hydrogeology of the region. Physical properties of the geological materials such as hydraulic conductivities, unsaturated

properties and porosity were measured in the field. Furthermore, meteorological conditions such as precipitation, snow cover thickness, air temperature and wind speed have also been regularly measured.

Several observation stations have been installed in the valley which allows calibrating the model using direct local field measurements. The observation stations include seven observation wells that measure groundwater levels throughout the valley and three temperature stations that provide temperature profiles down to 35 m in depth (Figure 3.1).

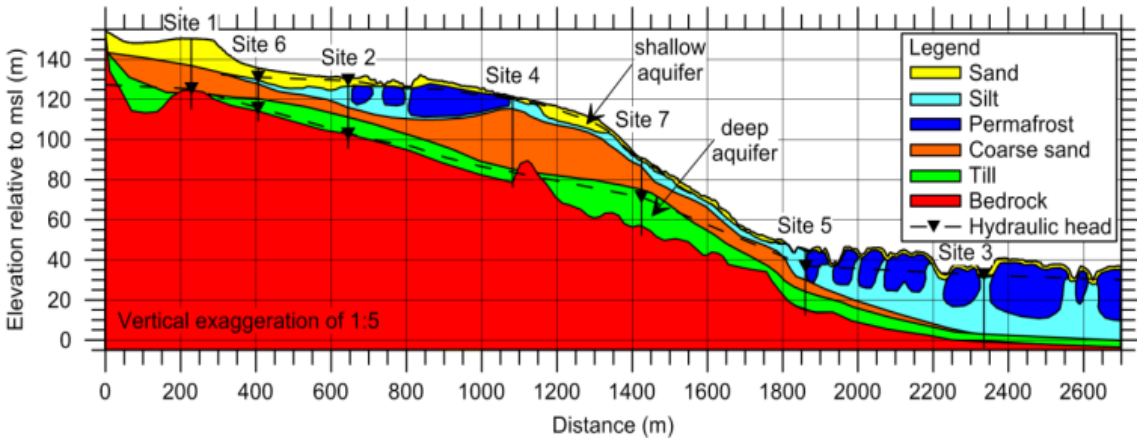

Figure 3.2 Vertical cross-section along the valley axis showing the 6 distinct hydrostratigraphic units. Cross-section location given in Figure 3.1. (Modified from Lemieux et al. 2016).

Table 3.1 summarizes some of the available data from the field investigations which were used for the purpose of this paper, including climate data, geologic and hydraulic properties and water table levels.

Table 3.1 Type of data collected during field investigations

Category	Data	Source of Data
Geological	• Thickness of sediments • Distribution of sediments • Permafrost location and thickness	• Geophysics (Resistivity) • Grain-size, sediment type
Hydrogeological	• Hydraulic properties (K,θ) • Water table elevation and location	• Slug test

Meteorological	• Air temperature • Precipitation (rain, snow) • Snow thickness	• Weather stations

The hourly precipitation data (involving both rainfall and snow fall) is measured in the field by a Geonor T200-B instrument. Figure 3.3 shows measured precipitation from October 2012 until October 2016. More details on the field investigations in the catchment are provided in Lemieux et al. (2016).

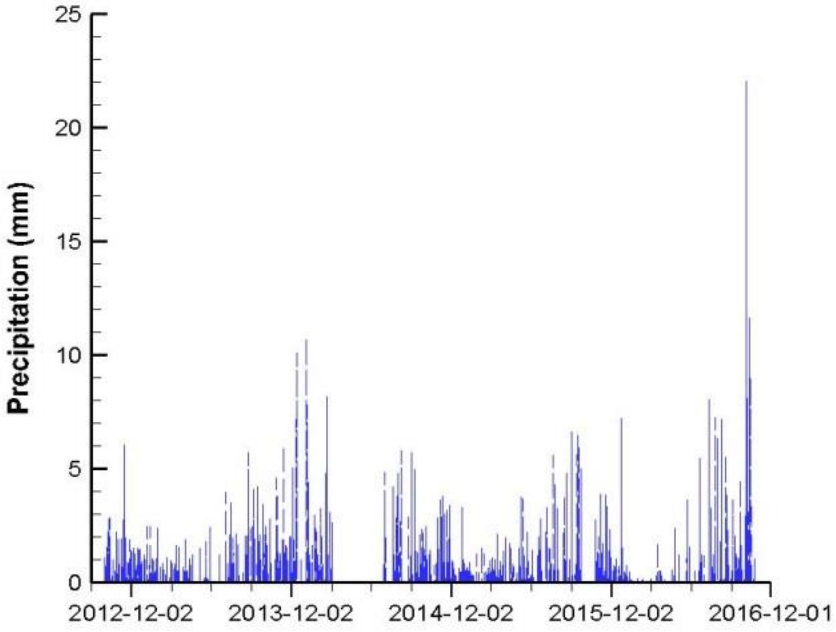

Figure 3.3 Precipitation (rain and snow fall) in the study area from October 2012 until October 2016

3.5 Methodology

3.5.1 Numerical model

The HydroGeoSphere model (Therrien et al. 2010), subsequently referred to as HGS, was used to simulate the hydrogeological system in this project. HGS is a physically-based 3D model that couples 2D overland flow with 3D variably-saturated subsurface flow. For the

purpose of this paper, HGS is used to develop a model for variably-saturated groundwater flow.

The basic equation that HGS uses to model transient subsurface flow in a variably-saturated porous medium is a modified form of Richards' equation:

$$-\nabla.(\omega_m q)+\sum \Gamma_{ex} \pm Q = \omega_m \frac{\partial}{\partial t}(\theta_s S_w) \quad (3\text{-}1)$$

where ω_m (dimensionless) is the volumetric fraction of the total porosity of the porous medium. In Eq (3-1), S_w (dimensionless) and θ_S (dimensionless) are the degree of water saturation and the saturated water content, respectively, t is time (T), Q ($L^3L^{-3}T^{-1}$) represents a source/sink and Γ_{ex} ($L^3L^{-3}T^{-1}$) is the volumetric fluid exchange rate between the porous medium and other flow domains. q (T^{-1}) is the fluid flux which is defined as:

$$q = -Kk\nabla h \quad (3\text{-}2)$$

where K (LT^{-1}) is the hydraulic conductivity, k (dimensionless) is the relative permeability as a function of water saturation and h is the hydraulic head.

3.5.2 Initial and boundary conditions

The bottom boundary of the simulation domain is located at an elevation of -40 m within bedrock. A no-flow boundary condition is considered at the bottom and lateral boundaries of the model, except at the lateral nodes below the watershed outlet where a specified head boundary condition is applied to let the water drain via the subsurface. Only the subsurface medium is included here. A recharge equal to 20% of precipitation is applied to surface nodes. Since surface-subsurface water interaction is not calculated by HGS in this case, the specific head boundary condition is applied to selected surface nodes on the river and close to the outlet to allow water discharge.

For the transient water flow simulation, the final system state (hydraulic heads and saturation) obtained from the steady-state calibration was used as the initial condition.

While hydraulic conductivities were obtained from the PEST calibration, specific storage was calibrated manually to obtain a best fit to observed data. The Rosetta software is used to calculate the van Genuchten parameters from the grain-size distribution.

3.5.3 Calibration

The flow model is first calibrated for hydraulic conductivities by applying PEST with HGS and comparing simulated steady-state heads against observed heads in the 7 observation wells. Subsequently, the calibrated models were used to simulate transient variably-saturated flow, and the results were compared with field-measured time series for hydraulic heads. The 3D calibration was completed using three different functions available in PEST: 1) estimation with defined geologic zones (referred to here as 'zoning'), 2) regularization by pilot-points, and 3) a combination of the two approaches (pilot-point-zoning).

From the field measurements, 6 main hydrostratigraphic units were determined for the catchment (Figure 3.2). In the zoning method, the porous medium is divided into 6 zones, corresponding to these units, with piecewise uniformity and a single hydraulic conductivity value applied for each zone. Average measured hydraulic conductivities were used as initial estimates of hydraulic conductivities in PEST. In regularization by pilot-points, 55 pilot-points were used in 5 sub-layers to calibrate the 3D model (Figure 3.4).The hydraulic conductivities at the pilot-points were allowed to vary within the range of 1E-10 - 1E-1 m/s. However, the range of hydraulic conductivities of the neighbour pilot-points is restricted by defining a variogram.

In the third approach, the allowed conductivity value for each pilot-point is restricted to a range based on the spatial distribution of points and proximity of the various hydrostratigraphic units defined from field measurements. The initial and boundary values used in the PEST control file for calibration using the zoning and the pilot-point-zoning methods are shown in Table 3.2.

Table 3.2 Initial estimate and range of allowed values for hydraulic conductivities in the zoning and pilot-point-zoning methods

Geologic units	Initial K (m/s)	Minimum K (m/s)	Maximum K(m/s)
Sand	4.55E-4	1E-6	1E-2
Silt	1.18E-7	1E-8	1E-5
Coarse sand	1.52E-4	1E-6	1E-2
Till	5.03E-4	1E-4	1E-2
Rock	2.20E-8	1E-10	1E-5
Permafrost	1.00E-8	1E-10	1E-7

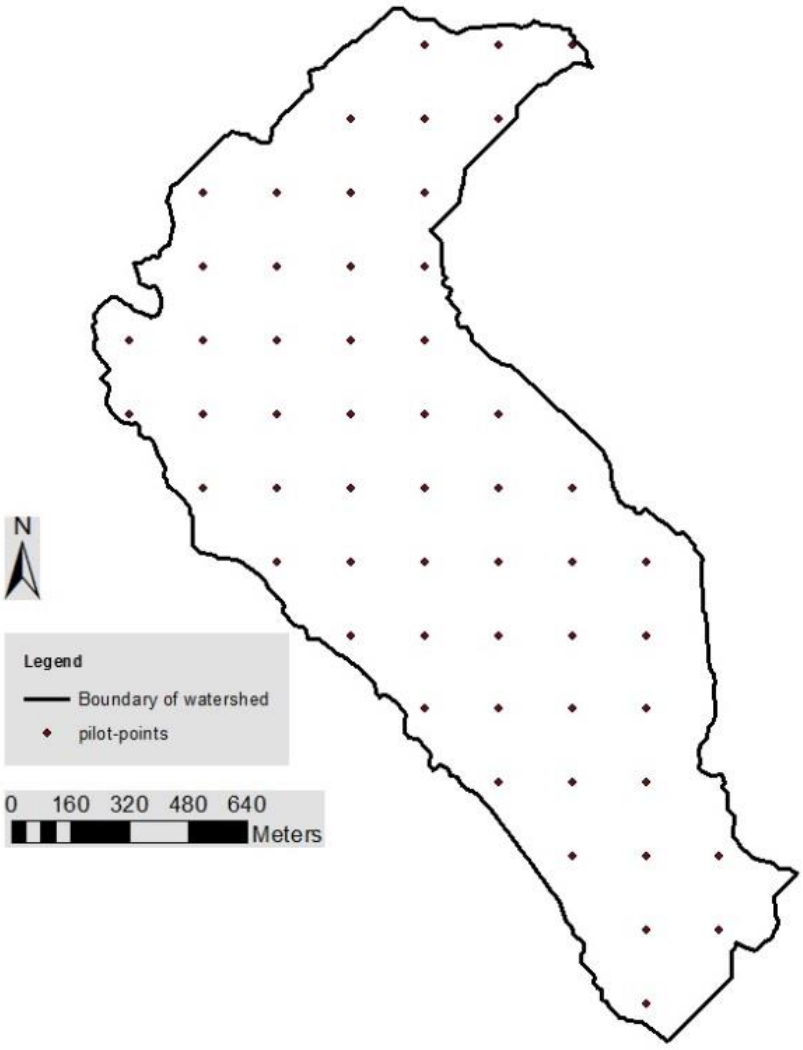

Figure 3.4 Location of pilot-points in the 2D plan. Five layers of pilot-points are used for the 3D model calibration.

3.6 Results

The calibrated hydraulic conductivities for the three PEST-calibration approaches are shown in Figure 3.5. In the calibration using zones, the boundaries of the defined hydrostratigraphic units are respected but each unit is assumed homogeneous and assigned a single hydraulic conductivity value. In regularization by only pilot-points, each point can have a different hydraulic conductivity, which will result in more heterogeneity in the model.

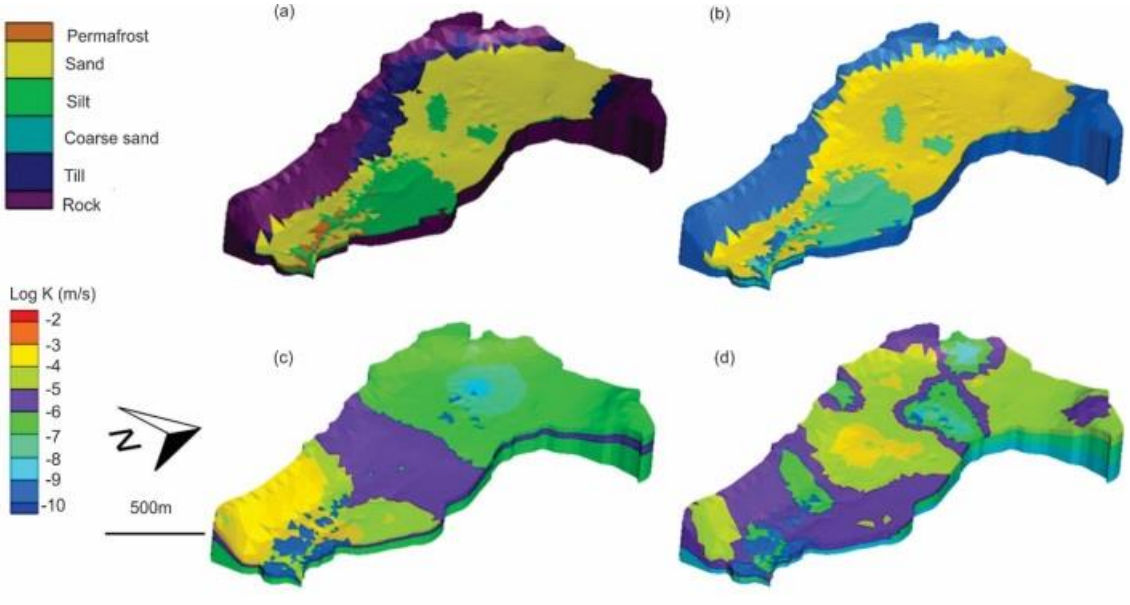

Figure 3.5 a) Hydrostratigraphic units from field investigations, and calibrated hydraulic conductivities from PEST using b) zoning, c) pilot-points and d) pilot-point-zoning approaches.

When using a combination of zones and pilot-points, the hydraulic conductivity at each point in each hydrostratigraphic unit can change compared to other points in that unit while they are all still restricted to the range of possible hydraulic conductivities for that unit. Therefore, more heterogeneity can be achieved for each unit compared to the zoning method while respecting the hydrostratigraphic boundaries.

The most important challenge when using pilot-points, either with pilot-points or pilot-point-zoning, is to maintain the permafrost units which are discontinuous and scattered. Depending on the density of the pilot-points in and around the permafrost units, these units may not be accurately reproduced, which could have significant effects on the flow system. After calibrating the model by pilot-points, a permafrost unit with a hydraulic conductivity of 4.9×10-10 m/s was therefore added to the model.

The hydraulic head was measured at seven wells for the period of 2012-10 until 2016-10. The average measured hydraulic head at the observation points was compared to the simulated head from the steady- state model. Each observation point has different sensitivity to the conductivity of each hydrostratigraphic unit, as determined with PEST (Figure 3.6). These sensitivities are obtained while calibrating the model using the zoning method. As an example, observation points at Well 02 and Well 03, which are near station T2 (Figure 3.1)

show a higher sensitivity to the hydraulic conductivity of the sand and silt layers, respectively. As seen in the cross-section in Figure 2, Well 02 is closer to the surface in the sand layer while Well 03 is deeper, in silt. The observation point 04 is surrounded by permafrost mounds, and shows higher sensitivity to the hydraulic conductivity of the silt layer.

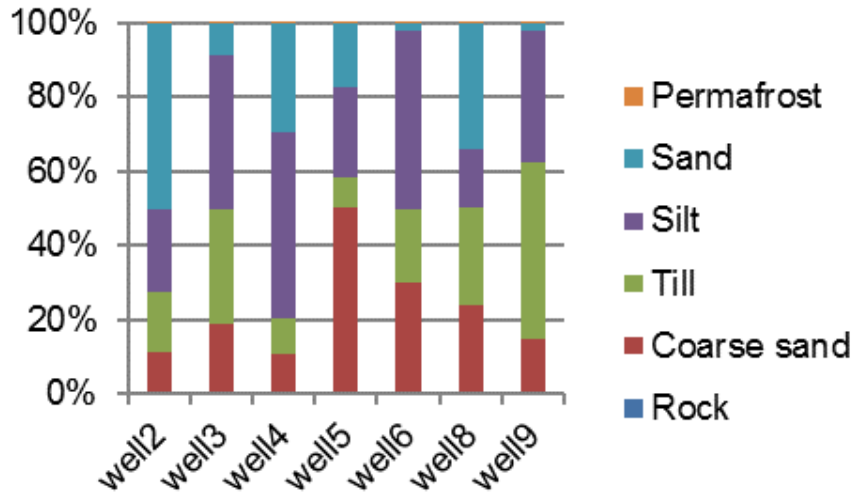

Figure 3.6 Sensitivity of hydraulic head to the hydrostratigraphic units for each observation point.

Figure 3.7 compares average observed heads in the seven observation wells to the simulated steady-state heads for the three calibration approaches. In this comparison, the pilot-point method shows a better fit compared to the two other methods. The calibrated heads from the zoning method are generally higher than the observed heads, especially at the center of the watershed. Except for Well 02, the pilot-point-zoning method has less error in the simulated heads compared to the zoning method.

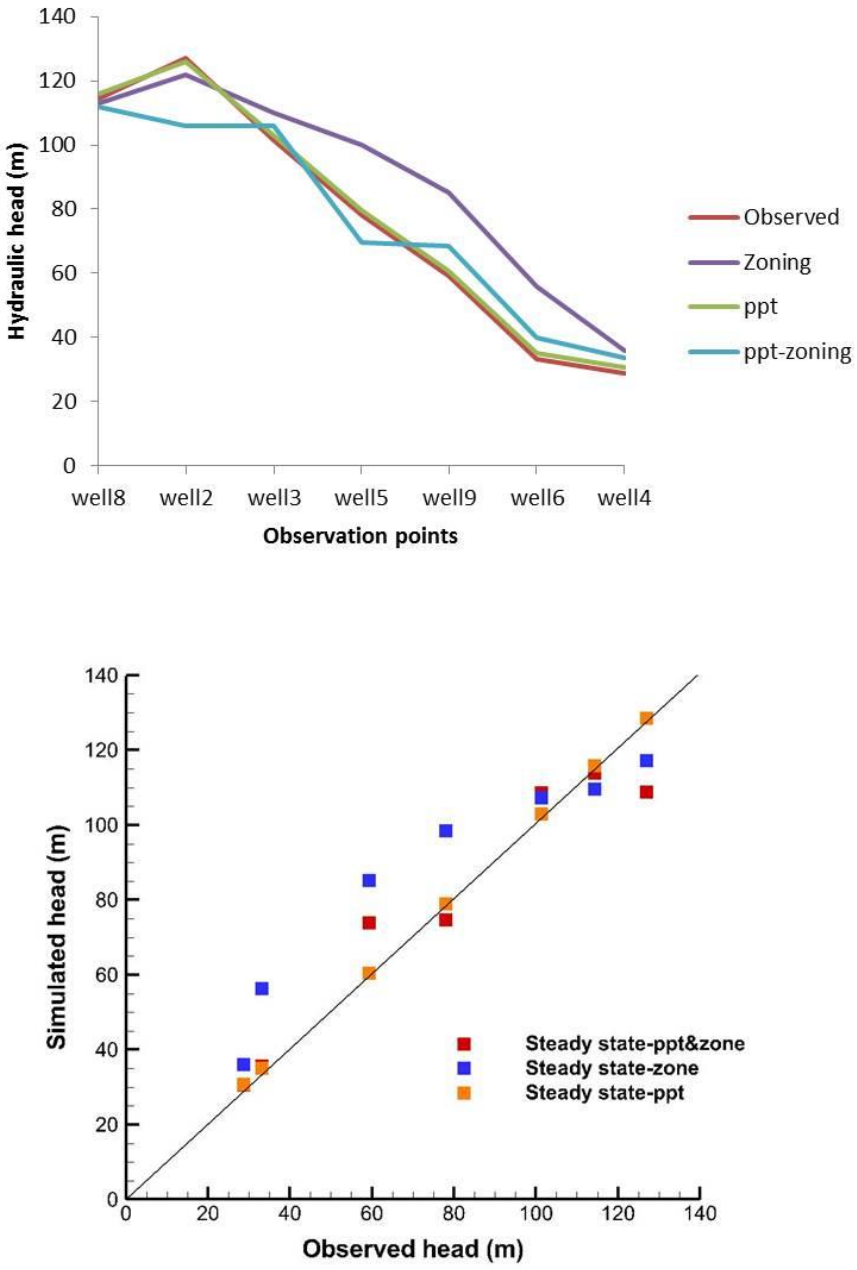

Figure 3.7 Comparison between the average observed hydraulic heads at seven observation wells to the simulated hydraulic heads using the three calibration methods.

After performing the steady-state calibration, the three models were used to simulate water flow under transient variably-saturated conditions. The specific storage is calibrated manually for the fine and coarse materials. The simulated time series of hydraulic heads were then compared to the time series measured in the field at Well 02 and Well 04, which show the best and worst fits, respectively (Figure 3.8). To better compare the time series and to show the dynamics in head variability, the head time series are adjusted in time to

match the observed heads at approximately the start of the observation times. The model developed by the zoning method is not included in the comparison due to its poor result under transient conditions.

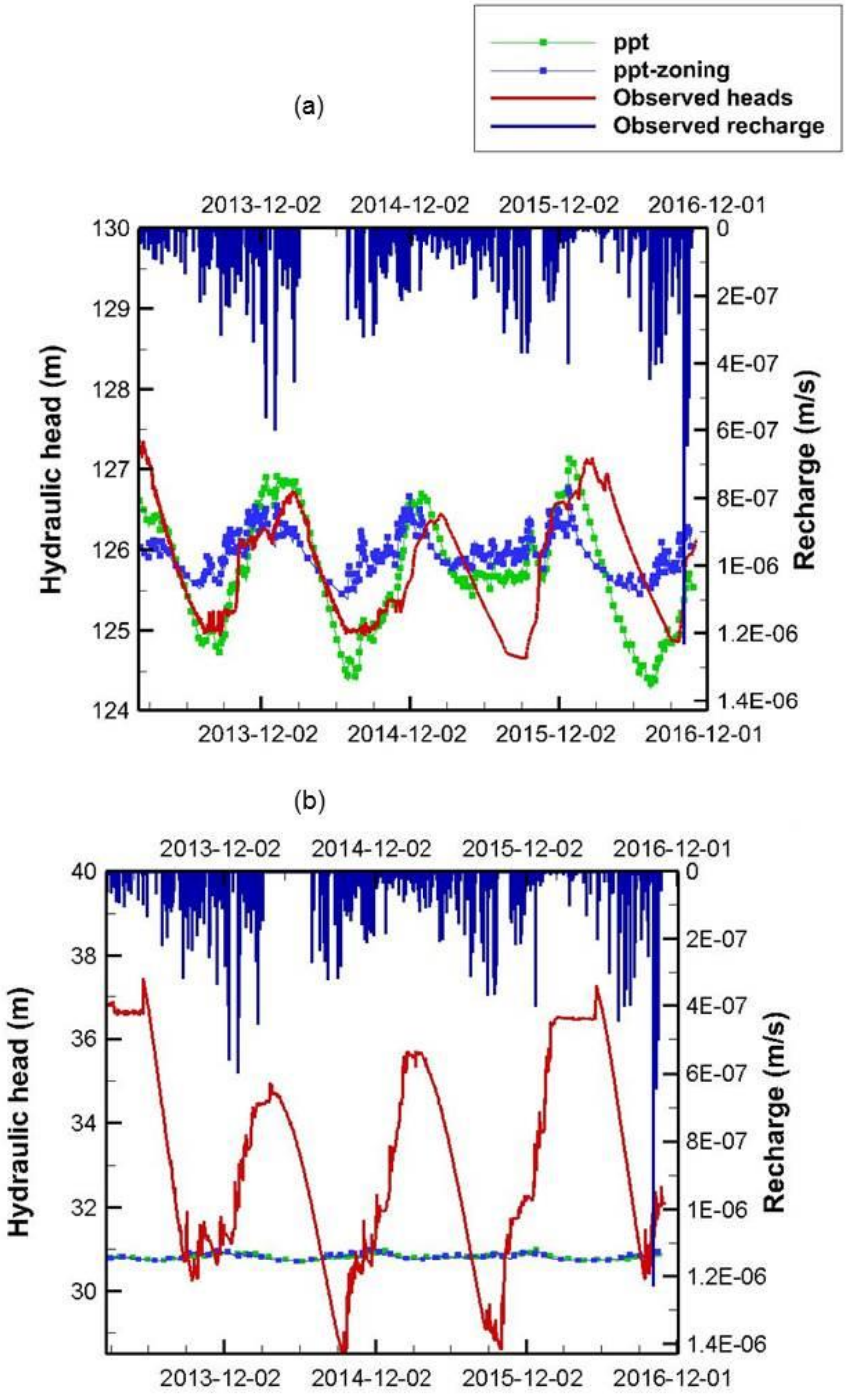

Figure 3.8 The respective best and worst fits for the simulated head time series at a) Well 02 and b) Well 04. To better compare the time series and to show the dynamics in head

variability, the head time series are adjusted to match observed heads at approximately the start of the observation times.

Both the pilot-point and pilot-point-zoning models have a good fit for Well 02. Although the pilot-point-zoning method showed a poorer fit at Well 02 under steady-state conditions compared to the zoning method, it demonstrated a better fit under transient conditions. The models showed the poorest fit at Well 04, which is located in the silty layer in the downstream part of the valley close to the outlet (Figure 3.1) and is surrounded by permafrost mounds.

Even though the two models showed a good fit to average hydraulic heads at Well 04 under steady-state conditions, the fit under transient flow was rather poor. Considering the number of pilot-points used in the calibration, the permafrost units were not completely maintained during the calibration process by PEST, which may be one reason behind the poor estimation of hydraulic heads in this location. In addition, the calibration was completed only under steady-state conditions, and other processes including freeze-thaw of permafrost on groundwater were not considered.

3.7 Discussion and conclusions

Three calibrated hydrogeological models were compared for a study area with discontinuous permafrost in northern Quebec. Using the defined hydrostratigraphic units and calibrating the model using the estimation mode in PEST respects the geologic field measurements and especially the permafrost unit which is important in studying groundwater flow system in cold regions. Another advantage of this method is having fewer unknowns and consequently a faster calibration. However, in this approach the heterogeneity within each unit is not considered which will result in a poorer fit of hydraulic heads.

In calibrating by pilot-points, the observed hydrostratigraphy is not taken into account and there is more freedom in changing the hydraulic conductivities at different points. As a result, increased heterogeneity and a better fit to observed values may be possible. However, the geometry of the permafrost units may be lost. This is especially important in the down-gradient part of the study area with more permafrost. This problem may be overcome by increasing the number of pilot-points in and around the permafrost units, however in this case the possibility of over-fitting should be considered. In addition, due to the higher number of unknowns, the calibration process will take more time. By using the combined pilot-point-

zoning method, the geologic field measurements can be considered. This method can reduce the possibility of over-fitting the model.

Surface water-groundwater interactions have not been included here, which may affect the calibration. Also, to reduce computational time, calibration was completed under steady-state conditions which may not be suitable in cold regions that include permafrost freezing and thawing. Due to the large number of unknowns in the model and resulting non-uniqueness of the fitted model, running only a few calibrated models is not sufficient to predict the groundwater flow conditions in this study area. Additional calibrated models are therefore needed to perform an uncertainty analysis and to evaluate the effect of future climate conditions on the groundwater flow system.

The calibration can be improved by increasing the number of pilot-points and using a transient model for calibration, each of which will increase the model complexity and calibration time. A balance between model accuracy and calibration time should therefore be sought. Future simulations with HGS for the catchment will integrate surface and subsurface flow as well as heat transport.

References

Ala-aho, P., Rossi, P.M., Isokangas, E. and Kløve, B. 2015. Fully integrated surface-subsurface flow modelling of groundwater-lake interaction in an esker aquifer: Model verification with stable isotopes and airborne thermal imaging. Journal of Hydrology, 522:391–406. doi:10.1016/j.jhydrol.2014.12.054.

Aquanty, 2016. HydroGeoSphere user manual, Release 1.0, Aquanty Inc., Waterloo, Ontario, Canada.

Doherty, J. 2016. PEST: Model-Independent Parameter Estimation, User Manual Part I: PEST, SEANSAN and Global Optimisers. Watermark Numerical Computing, 6th ed., Brisbane, Australia. Available from www.pesthomepage.org.

Doherty, J.E., Fienen, M.N. and Hunt, R.J. 2010. Approaches to Highly Parameterized Inversion : Pilot-Point Theory , Guidelines , and Research Directions. U.S. Geological Survey Scientific Investigations Report 2010–5168, 36p.

Herckenrath, D., Langevin, C.D. and Doherty, J. 2011. Predictive uncertainty analysis of a saltwater intrusion model using null-space Monte Carlo. Water Resources Research, 47(5): 1–16. doi:10.1029/2010WR009342.

Lemieux, J.-M., Fortier, R., Talbot-Poulin, M.-C., Molson, J., Therrien, R., Ouellet, M., Banville, D., Cochand, M. and Murray, R., 2016. Groundwater occurrence in cold environments: Examples from Nunavik, Canada, Hydrogeology Journal, Vol 24, Issue 6, pp 1497–1513.

Moeck, C., Hunkeler, D. and Brunner, P. 2015. Tutorials as a flexible alternative to GUIs: An example for advanced model calibration using Pilot-points. Environmental Modelling and Software, 66: 78–86. doi:10.1016/j.envsoft.2014.12.018.

Therrien, R., McLaren, R.G., Sudicky, E. A. and Panday, S.M. 2010. HydroGeoSphere : A Three-dimensional Numerical Model Describing Fully-integrated Subsurface and Surface Flow and Solute Transport. 429 pp.

Yoon, H., Hart, D.B. and McKenna, S.A. 2013. Parameter estimation and predictive uncertainty in stochastic inverse modelling of groundwater flow: Comparing null-space Monte Carlo and multiple starting point methods. Water Resources Research, 49(1): 536–553. doi:10.1002/wrcr.20064.

4 Simulation of coupled surface water and groundwater flow in a northern catchment

4.1 Introduction

Water resource management has been recently moving towards the integration of surface water and groundwater flow processes, which requires reliable simulation methods. The number of studies where coupled surface water and groundwater flow is simulated has also been increasing. For example, El-Zehairy et al. (2018) used the integrated MODFLOW-NWT transient model to characterize the interaction of an artificial lake with groundwater. They concluded that, contrary to natural lakes, interaction with groundwater in artificial lakes is mainly dependent of the balance between lake inflow and outflow, while precipitation and evapotranspiration play a secondary role. Maheswaran *et al.* (2016) analyzed stream-aquifer interaction using MODFLOW and concluded that long-term groundwater extraction has played a role in the sharp decrease of base flow in the Ganga River basin. Jones et al. (2008) applied the InHM model to a watershed in southern Ontario to investigate the model's ability to simulate transient flow processes. They initially calibrated the steady-state subsurface system to observed hydraulic heads and base flow discharge. They then calculated the discharge hydrograph by applying two rainfall time series and compared it to the observed rainfall-runoff responses. Results showed that the model could accurately simulate fully integrated surface and variably saturated subsurface flow.

Among the published studies where surface water and groundwater flow are fully integrated, a limited number have focused on cold regions. The study of groundwater flow in cold regions has its challenges and requires including other processes such as heat transfer and winter seasonal processes. Some studies have been conducted over the past few years to investigate the subsurface characteristics in northern regions, including temperature, permafrost distribution, and water quality. Sjöberg et al. (2013) combined field measurements and numerical simulations to show the effect of groundwater flow on permafrost distribution. Shojae Ghias *et al.* (2016) developed a 2D coupled water flow and heat transfer model with the HEATFLOW/SMOKER code to study the effect of climate warming on permafrost degradation in northern Canada. The model considered both advection and conduction processes. Their results showed that even though thermal

advection is not negligible in the study area, thermal conduction is the controlling process for permafrost degradation.

Existing simulations of the hydrogeology of cold regions usually involve some simplifications such as assuming a 2D environment or excluding surface processes. In this project, a 3D integrated model was developed by including surface water flow, groundwater flow and heat transfer to simulate and study the subsurface hydrogeological and thermal condition in a northern catchment near Umiujaq. This will extend our understanding of the effect of processes and parameters on the hydrogeological and thermal conditions of the aquifers in this region. While this chapter focuses on simulating surface and subsurface flow, the following chapters will present the simulation of heat transfer process in more detail.

4.2 Study Area

The study site is a 2 km^2 catchment located in a valley near the Inuit village of Umiujaq in northern Quebec, Canada (Figure 4.1). The flat downstream part of the valley is offset by an elevation difference of 100 m from the relatively flat upstream part. Six distinct hydrostratigraphic units have been defined by LIDAR topographic surfaces, surface geophysical EM surveys and borehole logs (Figure 4.2). In the upper reaches of the valley, the surface layer is a thin layer of littoral and pre-littoral sediments, which contains a shallow, perched aquifer. Below this aquifer lies a layer of frost-susceptible silt, which is thinner in the upper part of the valley and becomes thicker in the lower part. In the frost- susceptible silty marine unit, discontinuous permafrost mounds can be seen in the cross-section, especially where the silty layer is thicker. The silt layer overlies the layers of subaqueous fluvioglacial sediments (Gs) and frontal moraine deposits (Gxt). Units Gs and Gxt form a lower aquifer that is unconfined in the upper part of the valley and confined in the lower part.

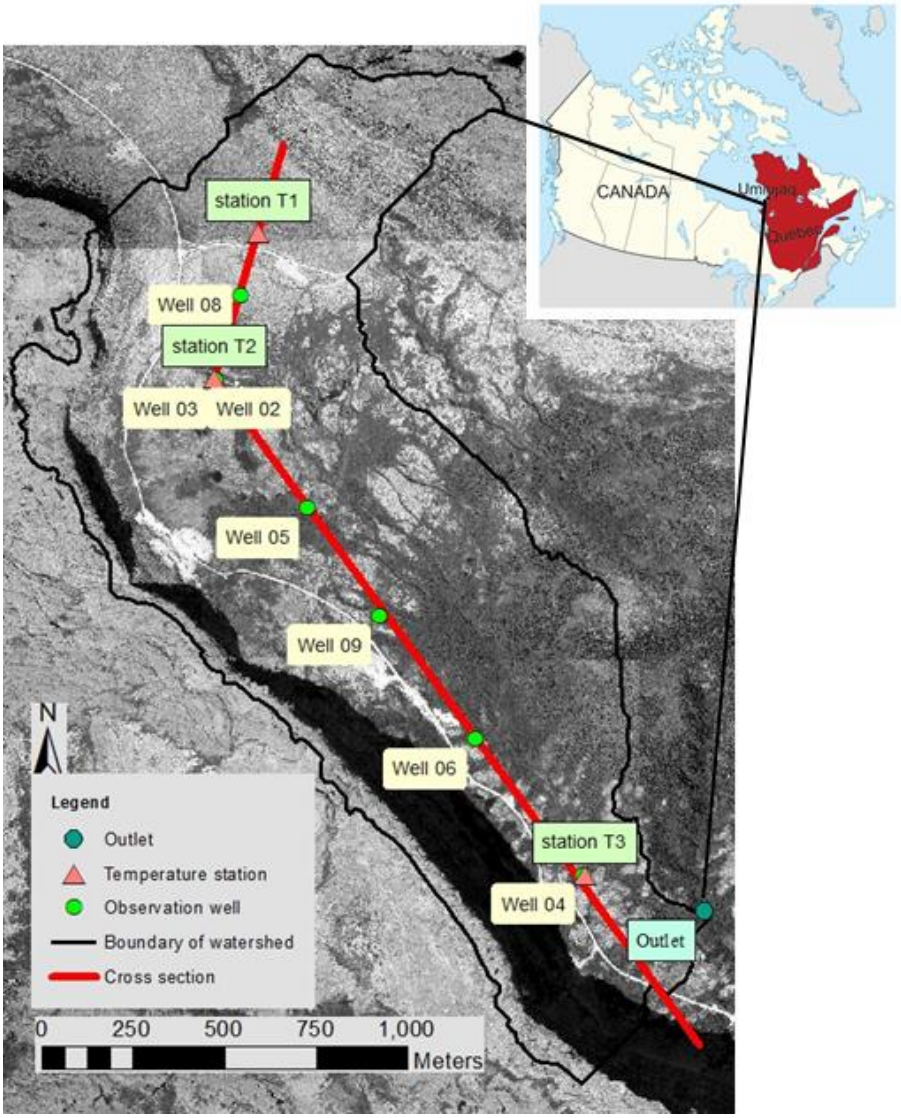

Figure 4.1 Location of study area near the village of Umiujaq in northern Quebec, showing observation boreholes and gauging station at the outlet. Red line identifies the cross-section for Figure 4.2.

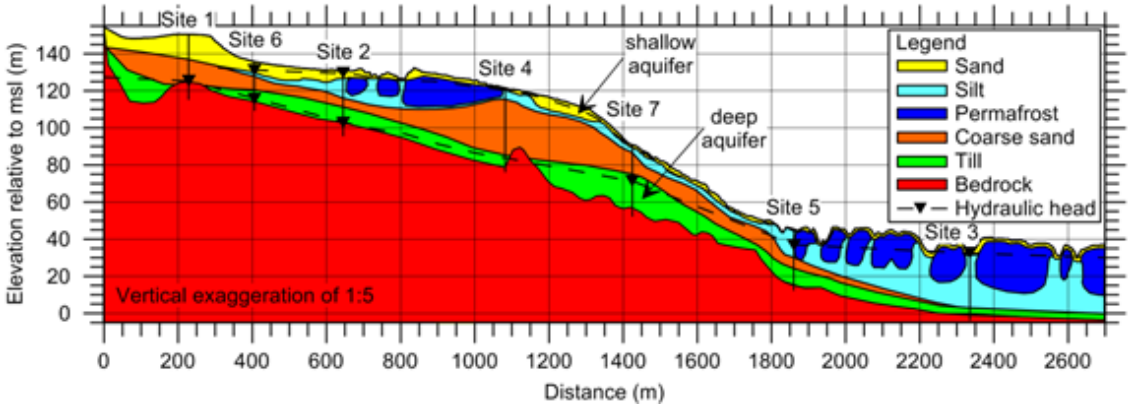

Figure 4.2 Cross-section of the study area with 6 distinct hydrostratigraphic units. The location of the cross-section is shown in Figure 4.2.

In this subarctic region, permafrost mounds are discontinuous but widespread. The permafrost mounds in the Tasiapik valley are characterized by an oval or approximately circular shape, 3 to 4 m higher than the surrounding terrain, as a result of frost heaving, and are about 50 m in diameter. The active layer, less than 2 m thick, is the surficial layer of the permafrost mound. The permafrost base is about 22.5 m deep (Leblanc et al., 2006).

The hydrology of the catchment has been studied since 2013. The catchment has a river system that is mainly intermittent except for the main stream. The physical properties of the geological materials such as hydraulic and thermal conductivities, porosity, and specific heat capacity were measured in the field. Furthermore, meteorological data such as precipitation, thickness of snow cover, and air temperature have been measured regularly. Several observation stations have also been installed, which provide field measurements for model calibration.

The observation stations include a gauging station installed near the outlet of the watershed, which quantifies surface runoff in the basin, seven observation boreholes that measure the groundwater level throughout the valley and 3 temperature stations that provide temperature profiles up to 35 m in depth (Figure 4.1). Furthermore, several temperature sensors were installed at ground surface to measure surface temperature. Among the observation boreholes, well 02 is located in the perched aquifer and the rest are in the lower aquifer. Table 4.1 summarizes the available data from the field investigations, which include climate data, geologic and hydraulic properties.

Table 4.1 Data provided through field investigations

Category	Data	Source of Data
Geological[1]	Thickness of sediments Distribution of sediments Water table elevation and location Permafrost location and thickness	Geophysics (Resistivity)
Hydrogeological[2] Data	Physical properties (K, θ) Water levels	Slug tests Grain-size or sediment type Observation boreholes
Thermal Data[3]	Thermal conductivity Heat capacity Temperature depth profiles	Field measurements* Temperature probes Literature values
Meteorological[5]	Air temperature Precipitation (rain, snow) Snow thickness	Weather stations

*Transient thermal conductivity probes and TDR antenna
[1]Banville (2016)
[2]Murray (2016), Dagenais (2018)
[3] Buteau (2002), Dagenais (2018)
[5] Barrère (2018)

4.2.1 Climate

The regional climate of the study site is subarctic with cool and damp summers, and relatively dry and cold winters. Hudson Bay has a major influence on regional climate due to the strong winds in winter when the bay is frozen and due to the often dense fog in summer. Figure 4.3 shows measured precipitation and air temperature at the study site from 2014-05-01 until 2017-05-01.

The vegetation cover is variable in the watershed and depends on the level of drainage. It consists of lichen vegetation in high topographic and well-drained zones at the upstream part of the watershed, shrubs in convex topographic areas and gullies near the permafrost mounds showing an advanced stage of degradation, spruce vegetation in well-drained sites in the southeast part of the watershed and herbaceous plants near bodies of water (Provencher-Nolet, 2014).

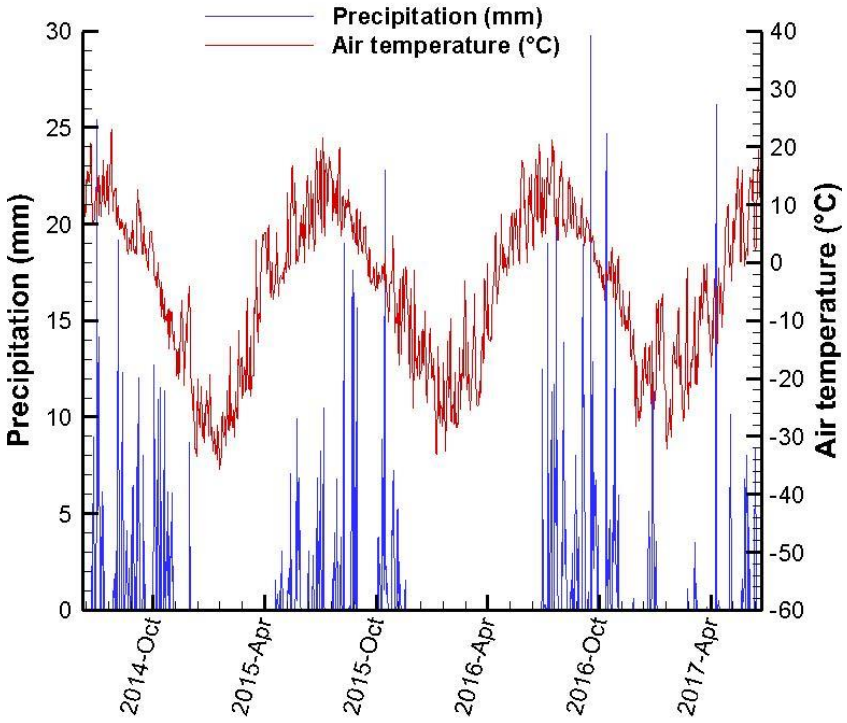

Figure 4.3 Measured precipitation and air temperature at Umiujaq from July 2014 to July 2017

4.3 Methodology

4.3.1 Numerical code

4.3.1.1 The numerical flow model HydroGeoSphere

HydroGeoSphere (HGS) is a fully-coupled 3D model that simulates the key processes of the hydrologic cycle and solves the surface subsurface flow, mass and energy transport equations simultaneously for each time step (Therrien et al., 2010). This chapter focuses on an application of the surface-subsurface flow part of the model while subsequent chapters include heat transport. For the water flow model, HGS couples the 2D depth-integrated diffusion wave approximation of the Saint Venant equation for surface water flow to the 3D variably saturated Richards' equation for the subsurface flow. The modified form of Richards' equation is (Therrien et al., 2010):

$$-\nabla.(\omega_m q) + \sum \Gamma_{ex} \pm Q = \omega_m \frac{\partial}{\partial t}(\theta_s S_w) \quad (4\text{-}1)$$

where ω_m (dimensionless) is the volumetric fraction of the total porosity occupied by the porous medium. S_w (dimensionless) and θ_s (dimensionless) are the water saturation and the saturated water content, respectively, t is time (T), Q $(L^3L^{-3}T^{-1})$ represents a source/sink, Γ_{ex} $(L^3L^{-3}T^{-1})$ is the volumetric fluid exchange rate between the porous medium and other flow domains, and q (LT^{-1}) is the fluid flux.

For surface flow, HGS solves the following diffusion-wave approximation of the Saint-Venant equation:

$$\frac{\partial \varphi_o h_o}{\partial t} - \frac{\partial}{\partial x}\left(d_o K_{ox} \frac{\partial h_o}{\partial x}\right) - \frac{\partial}{\partial y}\left(d_o K_{oy} \frac{\partial h_o}{\partial y}\right) + d_o \Gamma_o \pm Q_o = 0 \quad (4\text{-}1)$$

where K_{ox} and K_{oy} are surface conductances (LT^{-1}) that depend on the equation used to approximate the friction slopes, d_o is the depth of flow (L), h_o is the water surface elevation (L), t is time (T), Q_o is a volumetric flow rate per unit area representing external sources or sinks $(L^3L^{-3}T^{-1})$, φ_o is the surface flow domain porosity depending on rills and obstructions, and Γ_o is the water exchange rate $(L^3L^{-3}T^{-1})$ between the surface and subsurface systems.

The dual node scheme is used here to couple surface water and the subsurface porous medium. In this scheme, the hydraulic head difference between two domains and a coupling length is used in the Darcy flux relation to compute water transfer between the two domains. In using the dual node approach, the exchange term is defined by:

$$d_o \Gamma_o = \frac{k_r K_{zz}}{l_{exch}} (h - h_o) \quad (4\text{-}3)$$

where k_r is the relative permeability of the exchange layer, K_{zz} is the vertical saturated hydraulic conductivity, and $l_{exch}$is the coupling length (L).

The governing flow equations are discretized in HGS with the control volume finite element method and the resulting non-linear equations are solved by applying the Newton-Raphson linearization method. The matrix equations are implicit and are solved at each non-linear iteration until convergence. Further details of the governing equations and solution methodology are presented in (Therrien *et al.*, 2010).

In the numerical simulations carried out with HydroGeoSphere, the temperature is assumed to have an impact on both fluid properties density and viscosity (Aquanty, 2017). However, the simulations presented here did not account for soil freeze-thaw cycles and the effect of

latent heat. The hydraulic conductivity of permafrost units therefore remains constant throughout the simulation.

4.3.1.2 Implementation of winter process in HydroGeoSphere

In HGS, the governing equation for surface water flow is expanded to include both solid and liquid phases of water. The equation is not considering heat transport and the effect of latent heat. However, it considers the immobility of solid phase snow in the flow equation as:

$$\frac{\partial}{\partial t}(\rho_w d_{wv} + \rho_{snow} d_{snow}) = \frac{\partial}{\partial x}\left(\rho_w d_f K_{ox} \frac{\partial h_o}{\partial x}\right) + \frac{\partial}{\partial y}\left(\rho_w d_f K_{oy} \frac{\partial h_o}{\partial y}\right) + \rho_w \mathrm{Q_o} - \rho_w \Gamma_{\mathrm{ex}} + \rho_{snow}(q_{snow} - \mu) \quad (4\text{-}4)$$

where q_{snow} and μ_{snow} are the rates of snow precipitation and sublimation per unit surface area ($L^3 L^{-2} T^{-1}$), respectively. The depth of snow is determined by snow precipitation, sublimation and melting by temperature change:

$$\frac{\partial}{\partial t}(\rho_{snow} d_{snow}) = \rho_{snow}(q_{snow} - \mu) - \rho_{snow} q_{melt} \quad (4\text{-}5)$$

where the depth of snow is positive and the rate of melting is assumed to be proportional to a constant (α) and the difference between the air temperature (T_{air}) and threshold temperature ($T_{threshold}$) when $T_{air} > T_{threshold}$ or α=0 when $T_{air} \leq T_{threshold}$.

$$\rho_{snow} q_{melt} = \alpha(T_{air} - T_{threshold}) \quad (4\text{-}6)$$

A detailed description of snowmelt process in HGS is explained in the manual of HGS (Aquanty, 2017).

4.3.2 Conceptual model

Figure 4.4 shows the final mesh used in this study. Integrated hydrologic models simultaneously solve the surface water and subsurface flow equations. In using integrated hydrologic models, the initial condition has a significant impact on basin-averaged variables such as surface storage, subsurface storage and surface runoff (Seck et al. 2015). Careful initialization of the model can prevent misinterpretation of surface-subsurface feedback processes and reduce the bias between simulated and observed values (Ajami et al., 2014).

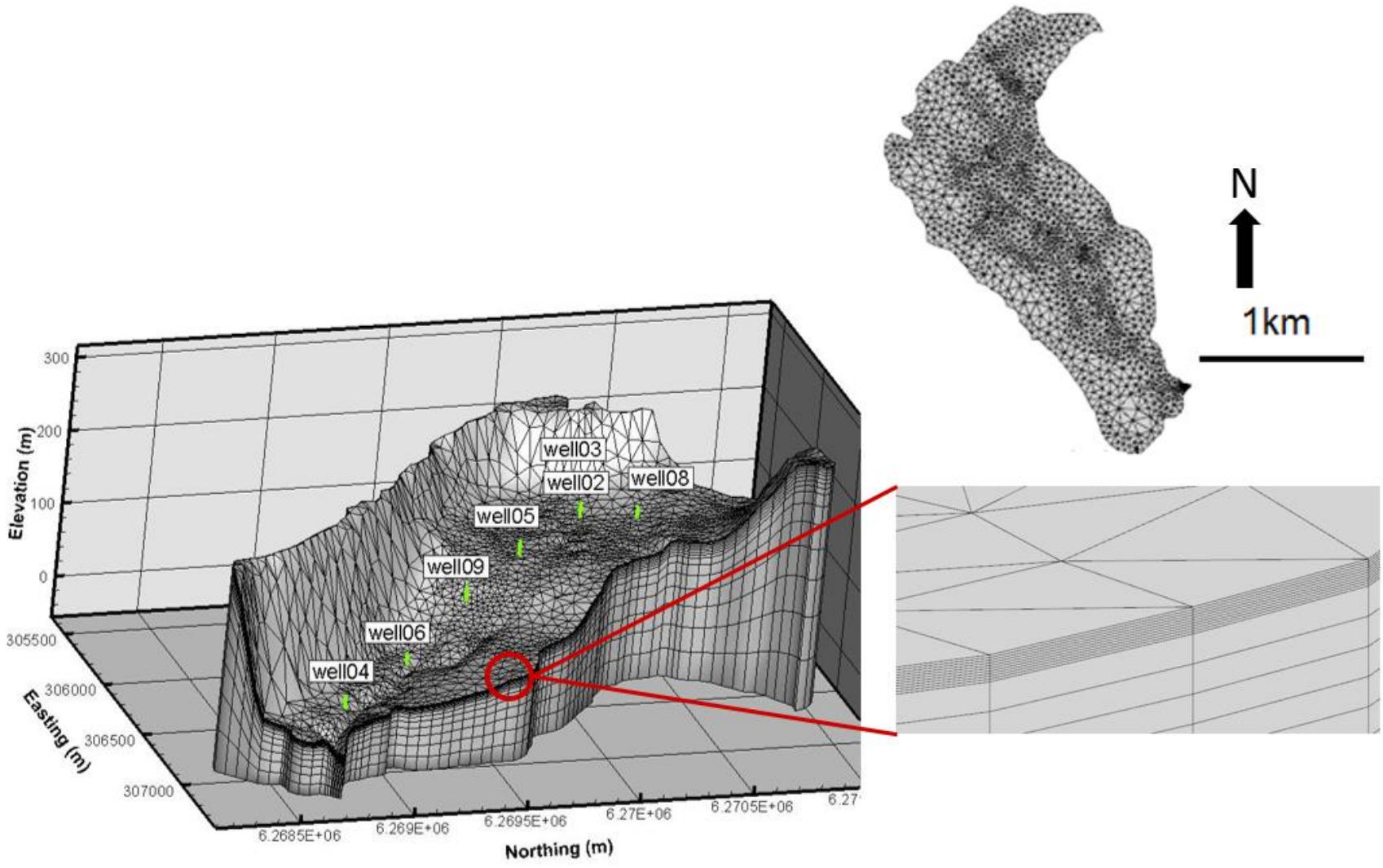

Figure 4.4 Conceptual mesh

One common approach for initializing an integrated model is through a process called spin-up (Goderniaux et al. 2009, Wood et al. 2004 and Ala-aho et al. 2015). During spin-up, the model is run for a sufficiently long time until there is a minimal drift in a chosen variable (such as subsurface storage). Then, the result of the spin-up simulation is used as the initial condition for the subsequent transient simulation. Ajami et al. (2014) showed that achieving equilibrium in subsurface storage ensures equilibrium among other variables related to groundwater flow and is therefore an indication of system-wide equilibrium.

Subsurface storage was chosen here as the variable representing the model state during the spin-up procedure and to determine when equilibrium has been reached. In order to perform the spin-up, the coupled flow model was run by applying a net average precipitation rate of 1.9×10^{-8} m/s (600 mm/yr). This represents the net average yearly precipitation rate during 2012-2016 and it is obtained by subtracting evapotranspiration from precipitation. The spin-up simulations were initiated from a fully-saturated state and were run until there was a minimal variation in the subsurface storage. Then, the final state of the spin-up model was used as the initial condition for the transient flow models.

In simulating transient water flow, the HGS model integrates hydrologic processes of the surface and subsurface domains. Boundary conditions were therefore applied to both domains. For the porous medium, a no-flow boundary condition was assigned to the bottom and lateral boundaries (representing the catchment limits), while for the surface water domain, net direct precipitation (which included both rainfall and snow) was applied to surface nodes. The net precipitation rate applied to the surface was the measured precipitation minus evapotranspiration. Since HGS solves the fully coupled surface and subsurface flow equations, recharge/discharge between the surface and subsurface domains is calculated as part of the solution to the interacting system (using the dual node approach). A critical depth boundary condition was implemented at the discharge location corresponding to the catchment outlet. This causes the water to discharge if its depth becomes greater than the critical depth. Due to the lower elevation of the nodes at the surface water outlet, water would mostly discharge through these outlet nodes. Discharge of water from surface nodes other than at the outlet was negligible.

The hydraulic conductivity was defined during calibration. Other model parameters are listed in Table 4.2 and Table 4.3. Permafrost units were assumed to be impermeable and it was further assumed that their hydraulic properties did not change with freezing and thawing.

Therefore, the hydraulic properties used for permafrost units were similar to those of an impermeable unit.

Table 4.2 Subsurface parameters

	Hydraulic properties		Unsaturated properties	
	Specific storage (m^{-1})[1]	Porosity[3]	α[2]	β[2]
Sand	1E-4	0.3	3.5	4.27
Silt	1.5E-4	0.4	0.49	1.7
Coarse sand	1E-4	0.35	3.69	3.61
Gravel	5E-5	0.25	3.55	4.13
Rock	1E-6	0.002	1.6	1.37
Permafrost	1E-6	0.002	1.6	1.37

[1]Determined from manual calibration
[2]Rosetta Software, based on grain distribution
[3]Buteau, (2002)

Table 4.3 Surface flow domain parameters

Parameter	**Value**
Coupling L (m)**	1.00E-4
Manning_silt ($m^{-1/3}s$)*	0.4
Manning_sand ($m^{-1/3}s$)*	0.8
Rill storage height (m)**	0.1
Obstruction storage height (m)**	0.1
Snow density (kgm^{-3})***	100
Melting constant ($ms^{-1}°C^{-1}$)***	5.79E-08

Sublimation (ms^{-1})***	1.46E-9
Threshold temperature(°C)***	0

* Chow (1959), ** Manual calibration, *** Aquanty (2017)

4.3.3 Calibration for hydraulic conductivity

The model had to be calibrated before being employed to predict future behaviour. A hydrologic model is calibrated by adjusting the model inputs until the model is able to simulate the observed data. Acknowledging uncertainty and non-uniqueness, one may then conclude that the model will adequately represent the behaviour of the system.

The 3D surface/subsurface water flow model was calibrated for hydraulic conductivities against hydraulic heads measured at the observation wells and the discharge rate measured at the stream outlet. The geologic units are assumed to be isotropic. Two stages were used in calibrating the model for hydraulic conductivities. In the first stage, the model was calibrated against the average measured hydraulic heads at the observation wells for steady-state flow conditions. This step is discussed in Chapter 3. In the second stage, the model was calibrated to reproduce daily measured hydraulic heads and streamflow for transient and variably-saturate flow conditions. Discontinuous permafrost units were represented as low-K units in this study. Since the effect of soil freeze-thaw is not simulated, the hydraulic conductivity of the permafrost units remains constant throughout the simulations.

The simulated hydraulic heads were compared against the measured heads at wells 4, 6, and 9 (Figure 4.1). The simulated discharge at the outlet was compared to that measured between July 2014 and July 2017. Well 02 was initially included in the calibration process. However, this well is located in the perched aquifer and the representation of the subsurface in this region is not detailed enough with the zoning method to provide an adequate match to observed values. It was therefore eliminated from the calibration in the final stages.

The parameter estimation package PEST (Doherty, 2010) was linked to HGS for the automatic calibration process.

To reduce simulation times, calibration in the transient mode used the zoning function of PEST. In the zoning method, the model domain was subdivided into 6 zones of piecewise uniform parameters. All elements in each zone had the same parameter value throughout

the calibration process. To start the calibration, an initial value was assigned to the calibration parameters. Starting with these initially defined values, PEST proceeds through an iterative process and by using the observed values, the parameters in each zone are estimated. Table 4.4 lists the allowed calibration range for each geologic unit based on a literature review.

Table 4.4 Initial estimate and range of allowed values for hydraulic conductivities for the zoning and pilot-points zoning methods

Geologic units	Initial K (m/s)	Minimum K (m/s)	Maximum K (m/s)
Sand	4.55E-4	1E-6	1E-2
Silt	1.18E-7	1E-8	1E-5
Coarse sand	1.52E-4	1E-6	1E-2
Gravel	5.03E-4	1E-4	1E-2
Rock	2.20E-8	1E-10	1E-5
Permafrost	1.00E-8	1E-10	1E-7

To calibrate the model in transient mode, significant computational time is required. In order to reduce the computational time, HGS was run in parallel mode and using PEST in its Highly Parallelized (HP) mode (Doherty and Hunt, 2010).

4.3.3.1 The pilot-points zoning method

The pilot-points zoning method was briefly described in Chapter 3. This section discusses the effect of having different numbers of pilot-points in a 3D model calibration with pilot-points zoning, which was not included in the discussion of Chapter 3.

The pilot-points zoning method is a combination of the zoning and pilot-points methods. In the pilot-points method, the same range of hydraulic conductivity values is assigned to each of the pilot-points. In the pilot-points zoning method, the allowed hydraulic conductivity for

each pilot-point is restricted to a range based on the spatial distribution of points and the proximity of the various hydrostratigraphic units defined from field measurements. This means that the position of points in the model domain is compared to the geology of the subsurface. Accordingly, based on the hydrostratigraphic zone, minimum and maximum hydraulic conductivity values are assigned to pilot-points. For instance, for the points spatially positioned in the sand unit, the model will use hydraulic conductivities between 1E-6 and 1E-2 m/s (Table 4.4). This method allows tailoring pilot-points using the geology of area.

Two sets of pilot-points were used to investigate this method. In Model 1, 55 points in 5 layers (275 points in total) were used for pilot-points zoning to calibrate the model, which is the same number of points used for the pilot-points zoning method explained in Chapter 3. In model 2, 55 points in 10 layers (550 in total) were also used to calibrate the model using the pilot-points zoning method. The comparison was made using the two models with similar grid and 5 and 10 sublayers (i.e., Model 1 and Model 2). Values from Table 4.4 are used as the initial and boundary values in the PEST control file for the calibration with the pilot-points zoning method. This calibration assumed steady-state water flow.

4.3.4 Sensitivity analysis

A sensitivity analysis was conducted against the measured hydraulic heads. In the first stage, the sensitivity analysis was conducted assuming steady-state conditions by including only the hydraulic conductivity of each geologic unit. These sensitivities were obtained while calibrating the model using the zoning method explained in Chapter 3. In the second stage, the sensitivity analysis was performed for transient flow and by including many of the effective parameters in a variably saturated surface water - groundwater flow system. Table 4.5 and Table 4.6 tabulate the parameters included in the sensitivity analysis along with the minimum and maximum value for each parameter.

Table 4.5 Subsurface parameters used in the sensitivity analysis

Material	K (m/s)*		S_s (m^{-1})**		θ_s (-)***		α (m^{-1})		β (-)		Rs	
	min	max	min	max	min	max	min	max	min	max	min	max
Rock	1e-10	1e-7	3e-6	7e-5	0.15	0.2	1e-5	10	1	10	1	10
Coarse Sand	1e-6	6e-3	1e-4	1e-3	0.25	0.5	1e-5	10	1	10	1	10
Till	1e-4	3e-2	5e-5	2e-4	0.25	0.4	1e-5	10	1	10	1	10
Silt	1e-0	5e-5	1e-3	3e-3	0.35	0.5	1e-5	10	1	10	1	10
Sand	1e-6	6e-3	1e-4	1e-3	0.25	0.5	1e-5	10	1	10	1	10
Perma-frost	1e-10	1e-7	3e-6	7e-5	0.35	0.5	1e-5	10	1	10	1	10

* Isotropic hydraulic conductivity. Domenico and Schwartz, 1990
** Batu, 1998
*** Freeze and Cherry (1979)

Table 4.6 Surface parameters used in the sensitivity analysis

parameter	**Min**	**max**
Coupling L (m)	1.00E-4	1.00
Manning_silt $(m^{-\frac{1}{3}}s)$	1	7
Manning_sand $(m^{-\frac{1}{3}}s)$	1	7

4.3.5 Uncertainties and limitations

Some parameter values assumed for material properties were obtained from a literature review and thus are somewhat uncertain. In addition, the main uncertainties and limitations in the model are listed below:

1. To better represent the geology of the study area, the model elements were linked to the GOCAD model to obtain the corresponding geology. The dimensions of the model elements played an important role on the accuracy of the hydrostratigraphy as represented in the model. For example, if the model element thicknesses were greater than the thickness of a geologic layer, the model would not represent the layer properly. Conversely, having finer elements increased the simulation time. Therefore, the final sublayer thicknesses were assigned to represent the study area with reasonable accuracy without significantly increasing the simulation time. Furthermore, the geologic model developed from field investigations included assumptions and data interpolation which would affect the model and simulation results.
2. A no-flow boundary condition was assumed at vertical boundaries around the catchment. However, previous studies in this area suggested that the boundary rock units could be fractured which could allow inflow and outflow. Since the existence, position, and properties of these fractures are uncertain, they were not considered in this study.
3. Another uncertainty in the assumed boundary conditions is the precipitation data used as the boundary condition for the surface. Although the precipitation time series was measured in the study area, its accuracy is unknown. It was initially thought that the processed precipitation would have led to better simulation results and the measured precipitation data were therefore processed according to the method explained in Chapter 1. However, because of significant measurement uncertainty for precipitation data, especially in winter (Lemieux et al., 2019), the processed data tended to be high and was not in agreement with climate conditions in Umiujaq. Furthermore, running the simulations with the processed precipitation gave a poorer fit to observed values, compared to the raw data. Therefore, in the final simulation, the model was run only with the raw precipitation data.

4.4 Results and discussion

4.4.1 Results of model calibration

The model calibration results under steady-state conditions are discussed in Chapter 3. In order to produce the daily hydraulic heads, hydraulic conductivities were calibrated to reproduce the observed daily hydraulic heads. Table 4.7 shows results for hydraulic conductivities for the different units after calibration under transient flow conditions.

Table 4.7 Calibrated hydraulic K* under transient conditions

Geologic Unit	**Hydraulic conductivity (m/s)**
Sand	5.9E-4
Silt	1.0E-6
Coarse sand	2.40E-4
Gravel	3.4E-4
Permafrost	6.7E-8
Rock	2.7E-10

* Hydraulic conductivity is assumed isotropic.

to Figure 4.9 show the geologic units in the 3D model, at selected cross sections throughout the catchment, along with hydraulic conductivities, simulated flow velocity, hydraulic heads, and depth to groundwater table. The bedrock unit is not shown in these figures.

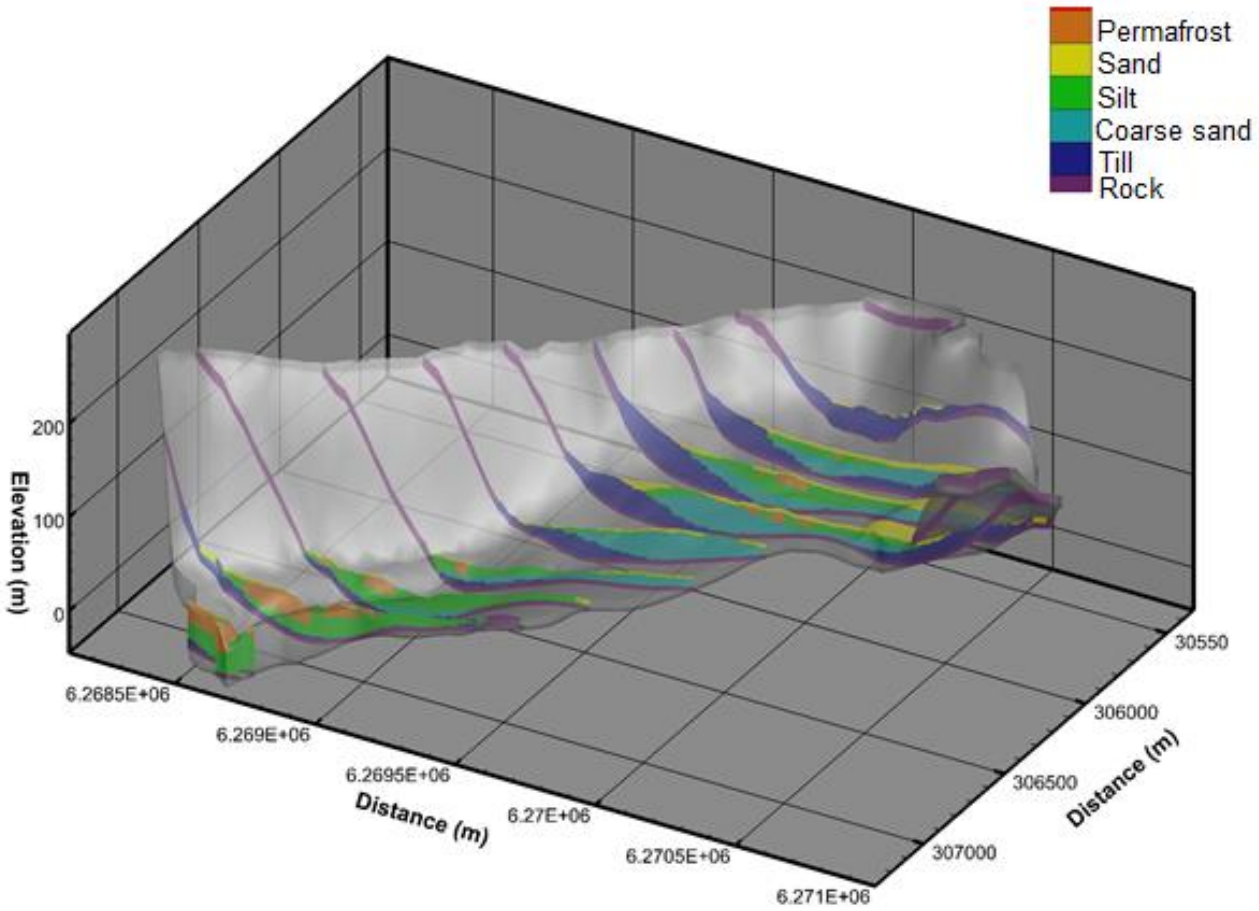

Figure 4.5 Subsurface structure of the 3D model

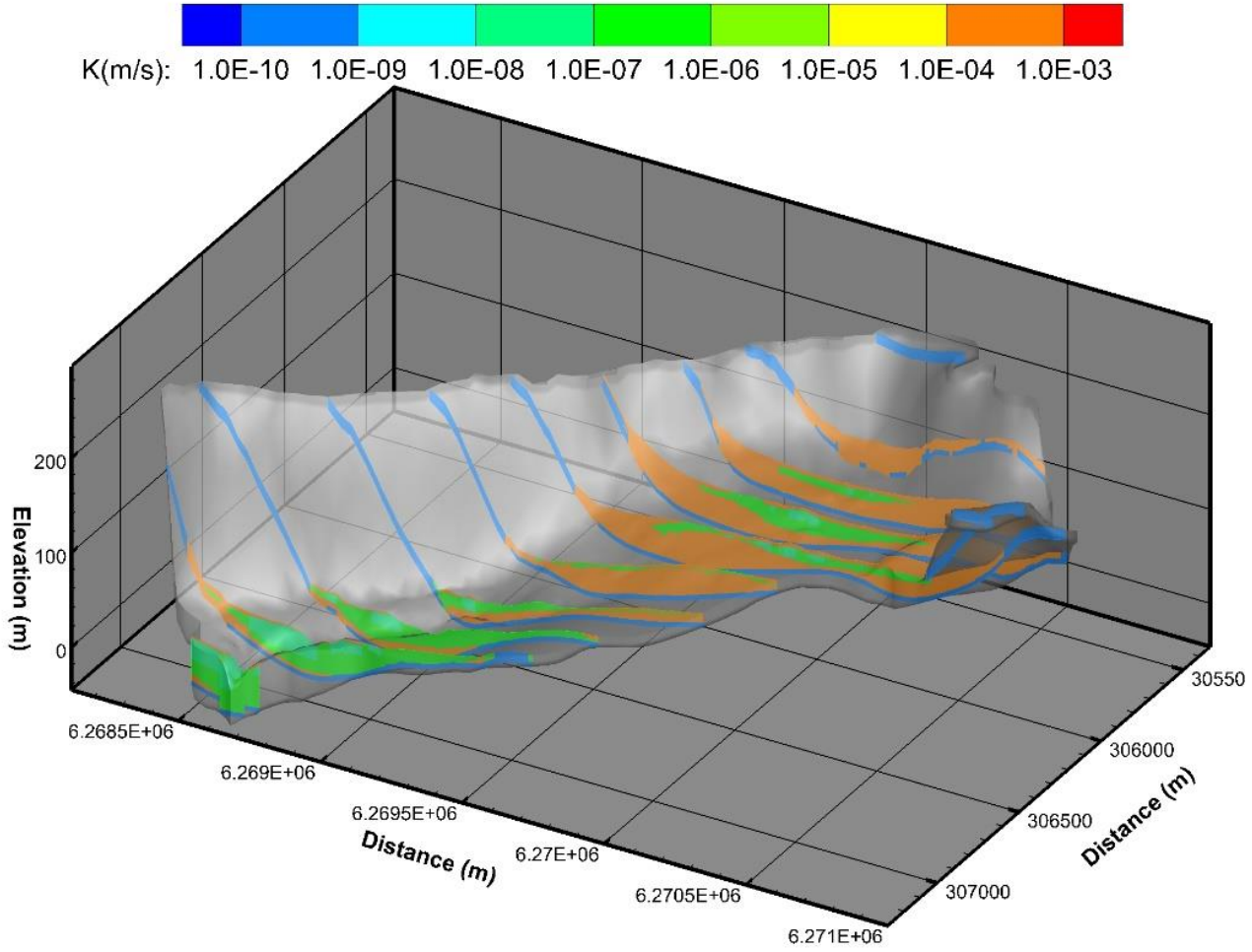

Figure 4.6 Calibrated hydraulic conductivities

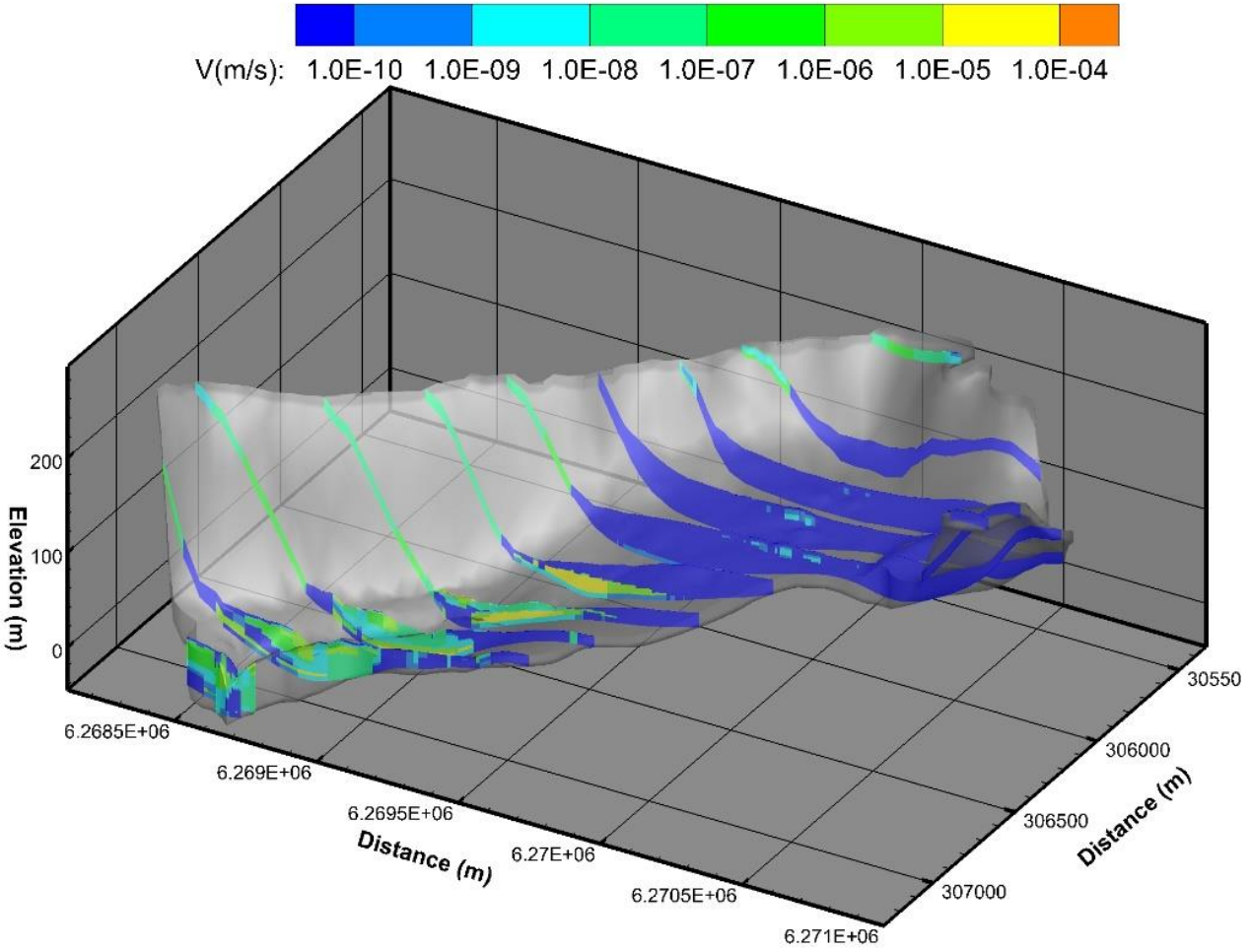

Figure 4.7 Simulated flow velocity at the end of the simulation (July 2017)

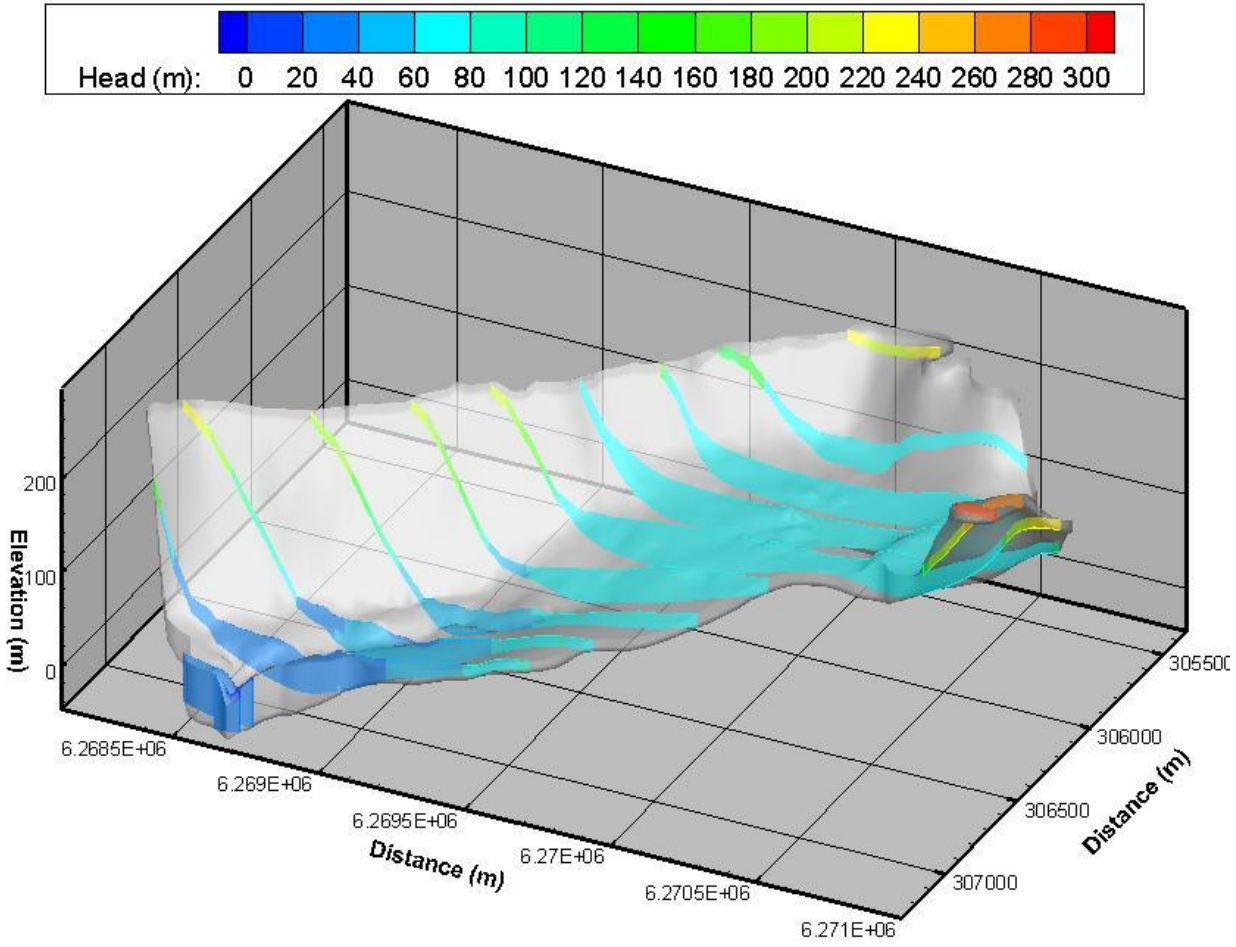

Figure 4.8 Simulated hydraulic heads at the end of the simulation (July 2017)

Figure 4.9 to Figure 4.11 show simulated hydraulic heads, water depth and flux exchange at the surface domain. Positive flow exchange shows the discharge areas, where negative flow exchange shows recharge to the subsurface. Flow exchange from subsurface to surface occurs in and around rivers, and in other areas the direction of flow exchange is from the surface to subsurface.

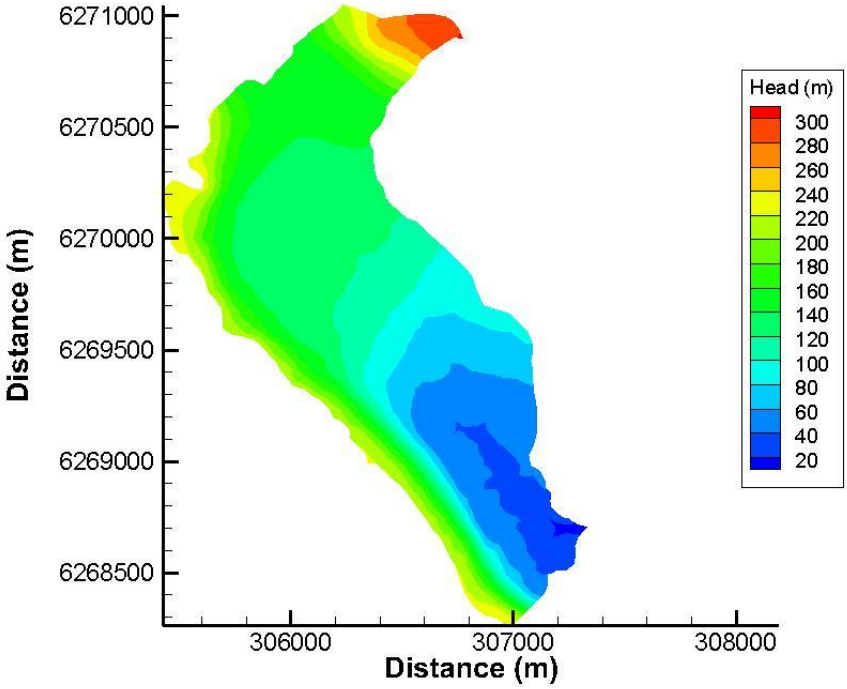

Figure 4.9 Hydraulic head in the surface water domain at the end of the simulation (July 2017)

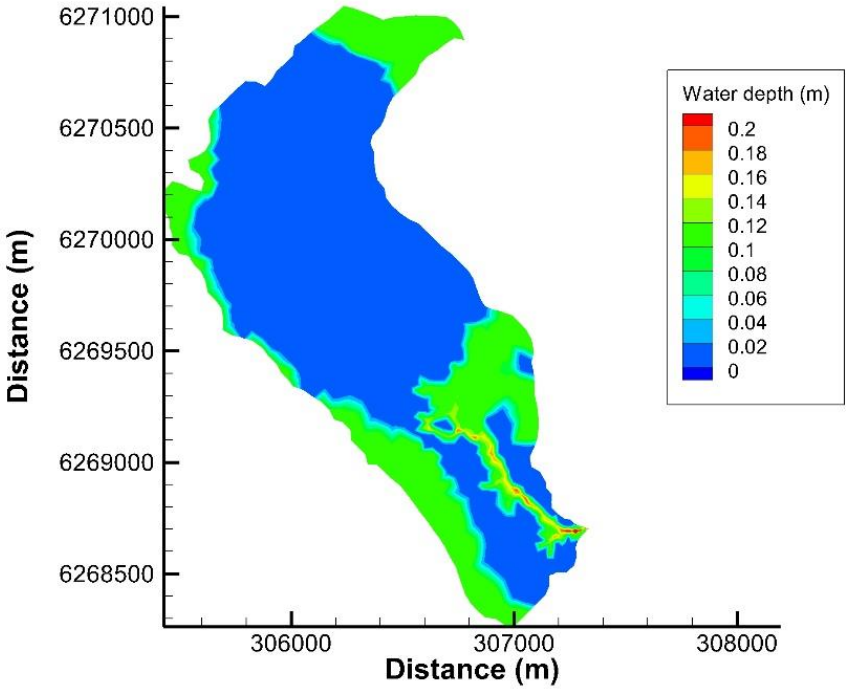

Figure 4.10 Surface water depth at the end of the simulation (July 2017)

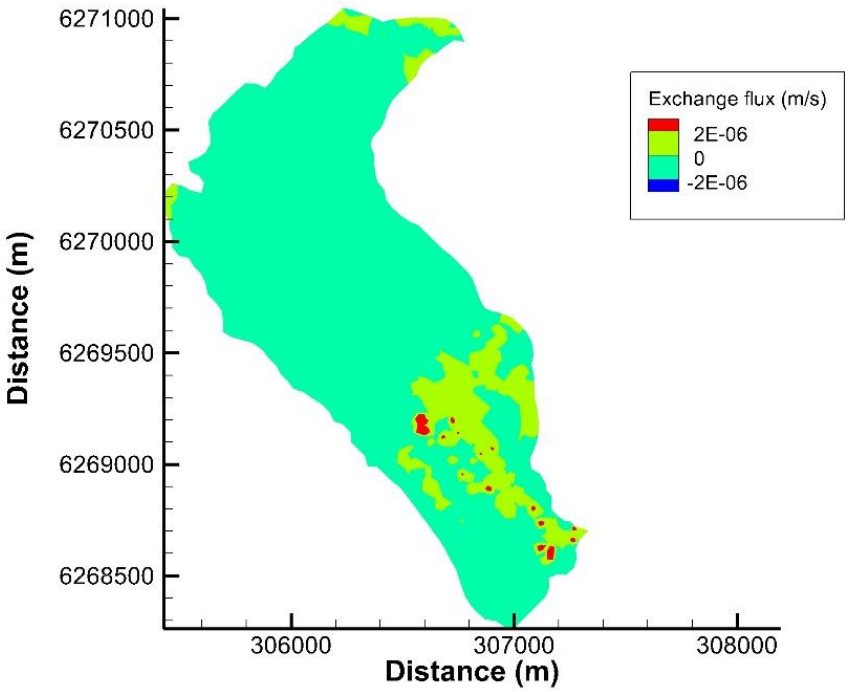

Figure 4.11 Flux exchange between the surface and subsurface domains at the end of the simulation (July 2017)

Figure 4.12 compares simulated and observed hydraulic heads at wells 04, 06 and 09 for the period July 2014 – July 2017. For the sake of comparison, the simulated time series at wells 04 and 06 are shifted down along the y-axis by 5 m. For wells 04, 06 and 09, the simulated heads show peaks during October and September in years 2014 to 2016. In addition, minimum simulated hydraulic heads occur during the months of May and July. Similar trends in maximum and minimum observed hydraulic heads are shown in Figure 4.12. However, the maximum and minimum simulated head values appear slightly earlier compared to the observed heads. In addition, the temporal variations in the simulated hydraulic heads at well 09 are considerably sharp while smooth variations were observed for wells 04 and 06 during the study period. Furthermore, the simulated and observed head scales are clearly different. This difference is significant for well 09, while it is smaller for wells 06 and 04. A reason for the differences between the observed and simulated hydraulic heads might be related to resolution of the confining unit. The geological GOCAD model used in this study was simplified and the numerical model had a relatively coarse mesh to

reduce computational time. This might have compromised the accuracy of the layer geometry in the model and resulted in shifts of hydraulic head between the confined and unconfined aquifers.

Even though the simulated and observed heads do not match well for wells 04 and 06, the differences in the simulated hydraulic heads between these two wells, at the same times (i.e. representing the hydraulic gradient) are similar to the observed differences. For example, in 2015, the observed hydraulic head difference between well 06 and well 04 varies between 2 m and 10 m while the simulated difference is between 2 m and 13 m. Therefore, the accuracy of the model in predicting and simulating the horizontal fluxes is considered acceptable, particularly for the area located between wells 04 and 06.

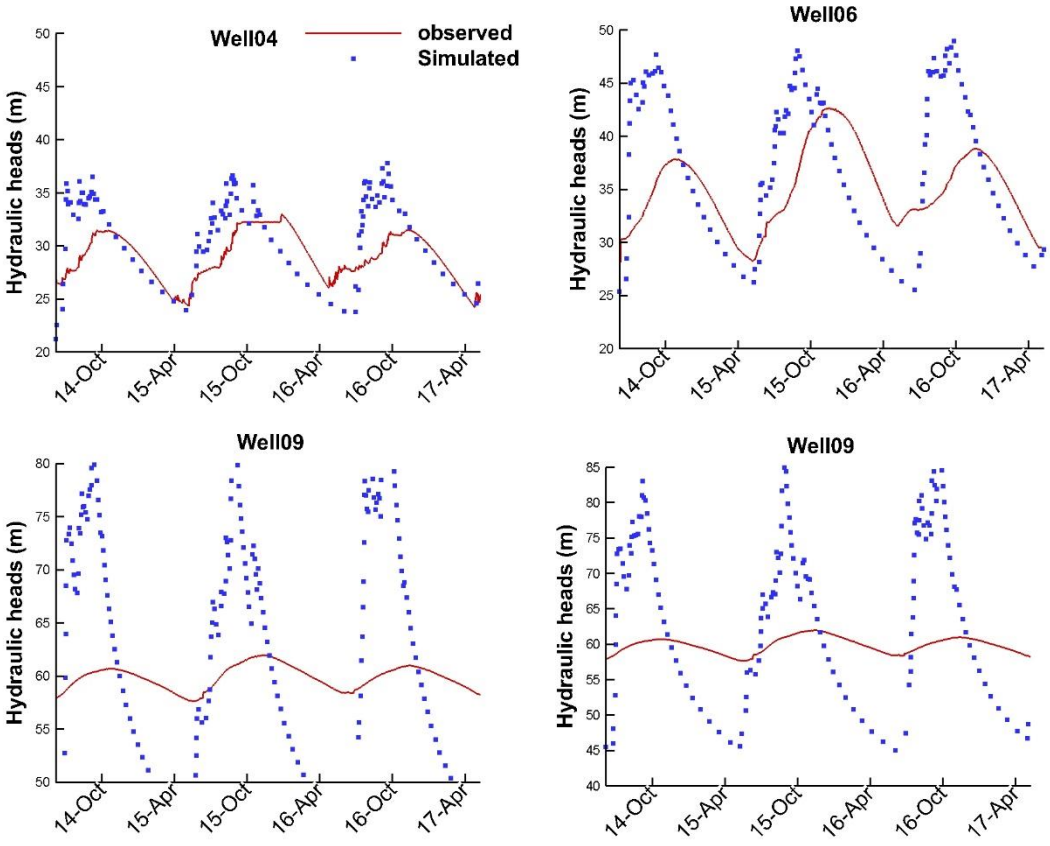

Figure 4.12 Simulated and measured hydraulic heads at wells 4, 6 and 9 (in similar intervals as wells 4 and 6, and in full extent)

Figure 4.13 shows simulated water saturations at wells 04, 06 and 09 for different years. Well 09 is located in the unconfined portion of the aquifer and its simulated saturation varies between 0.05 and 1.0. In contrast, wells 04 and 06 are located within the confined part and are always saturated. Field observation data by Lemieux et al (2019) show that wells 04 and 06 are in the confined aquifer and well 09 is located in the unconfined aquifer. Although the model properly shows that well 09 is located in the unconfined part of the aquifer, the simulated heads vary more than expected (Fig. 4.5). Considering that the subsurface structure at Umiujaq is highly heterogeneous, using a limited number of geologic zones in the calibration process by PEST can be a reason for not achieving a good fit at well 09.

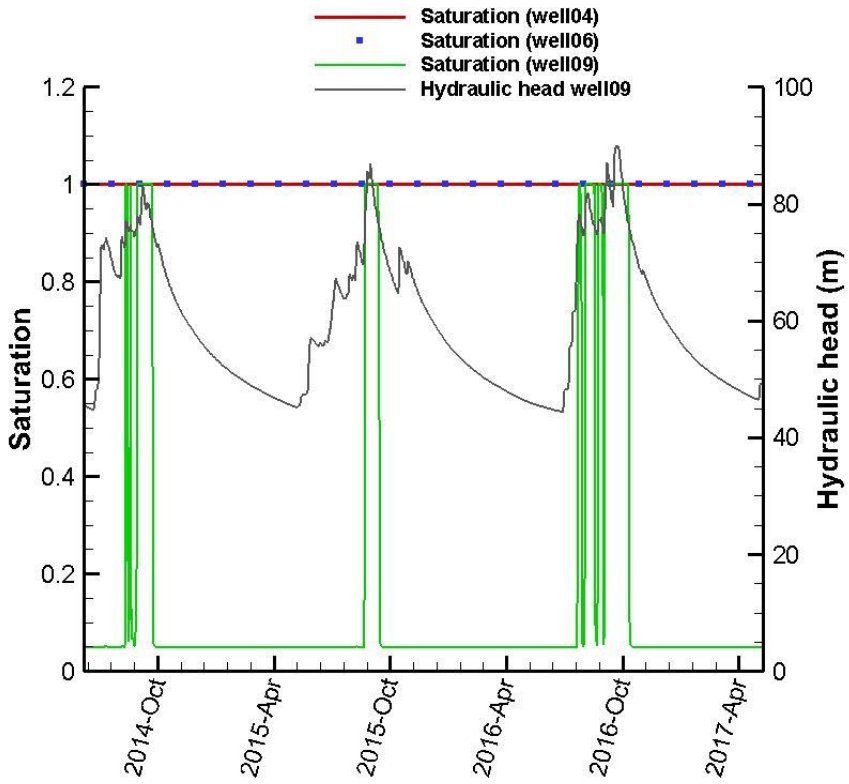

Figure 4.13 Simulated water saturation at the three observation wells and the simulated hydraulic head at well 09

Figure 4.14 compares the simulated and observed hydrographs for the three-year period. The hydrographs show that the agreement between the simulated and observed discharge is reasonable for the period between July and April. This suggests that the model is correctly simulating the water flow behaviour in the entire catchment and at the surface in this period. However, the observed hydrograph shows increases from April to July while there are no significant changes in simulated values at this period. This is in a period of snowmelt, which

might be infiltrating to the subsurface rather than flowing towards the outlet at surface in the model. This might be also a reason for the high-simulated hydraulic heads at well 09. The differences between observed and simulated hydrographs can be due to the controlling effect of surface properties, such as the Manning coefficient and obstruction storage, on the simulated hydrograph in summer. During the calibration by PEST, only average Manning values were considered in the surface domain and other surface properties (such as variable vegetation cover, which is seen in Umiujaq) were not included in the calibration process.

Due to limitations in computation time, the zoning method was used in this study for calibration as explained in Section 1.3.3. However, this method has some limitations, the main one being that the calibration process does not have the freedom to accurately generate the heterogeneity of the geological units. Considering that the study area is highly heterogeneous, this is a significant limitation, particularly for wells 02 and 09. For example, as discussed in Section 1.2, well 02 is located in the perched aquifer that needs a finer locally detailed subsurface structure. In this case, the pilot-points method could be used to further improve the calibration.

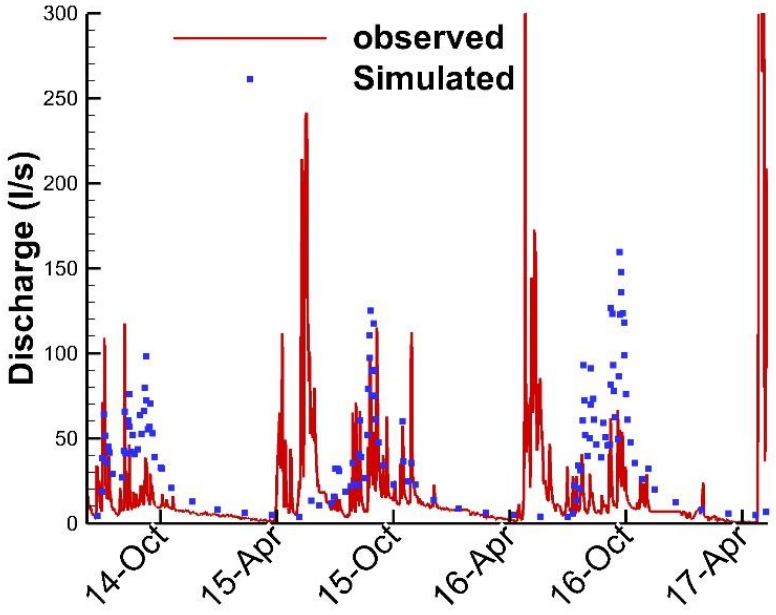

Figure 4.14 Simulated and measured hydrograph from the model calibration

4.4.1.1 The effect of finer sublayers on calibration by pilot-points zoning

In this section, the effect of pilot-point layer refinement on the calibration is studied for the pilot-point zoning method. The calibration was conducted for Model 1 and Model 2 with 5 and 10 pilot-point layers, respectively, each containing 55 pilot-points. Therefore, more pilot-points were used for Model 2. Both models were calibrated against the average hydraulic heads at wells 02, 04, 06, and 09. The number of sublayers in the model is similar to the number of layers of pilot-points.

Figure 4.15 compares hydraulic conductivities in the layer cross-sections for the two models while Figure 4.16 compares the average simulated steady-state hydraulic heads from the two models against the average observed values. Model 2 shows a more refined subsurface structure compared to Model 1. In addition, a layer of permeable material between two layers with lower permeability is obtained for Model 2. Figure 4.15 also shows the velocity vectors for the two models. In both models, the direction of flow in the low permeability zones is downward, towards the layer with higher permeability.

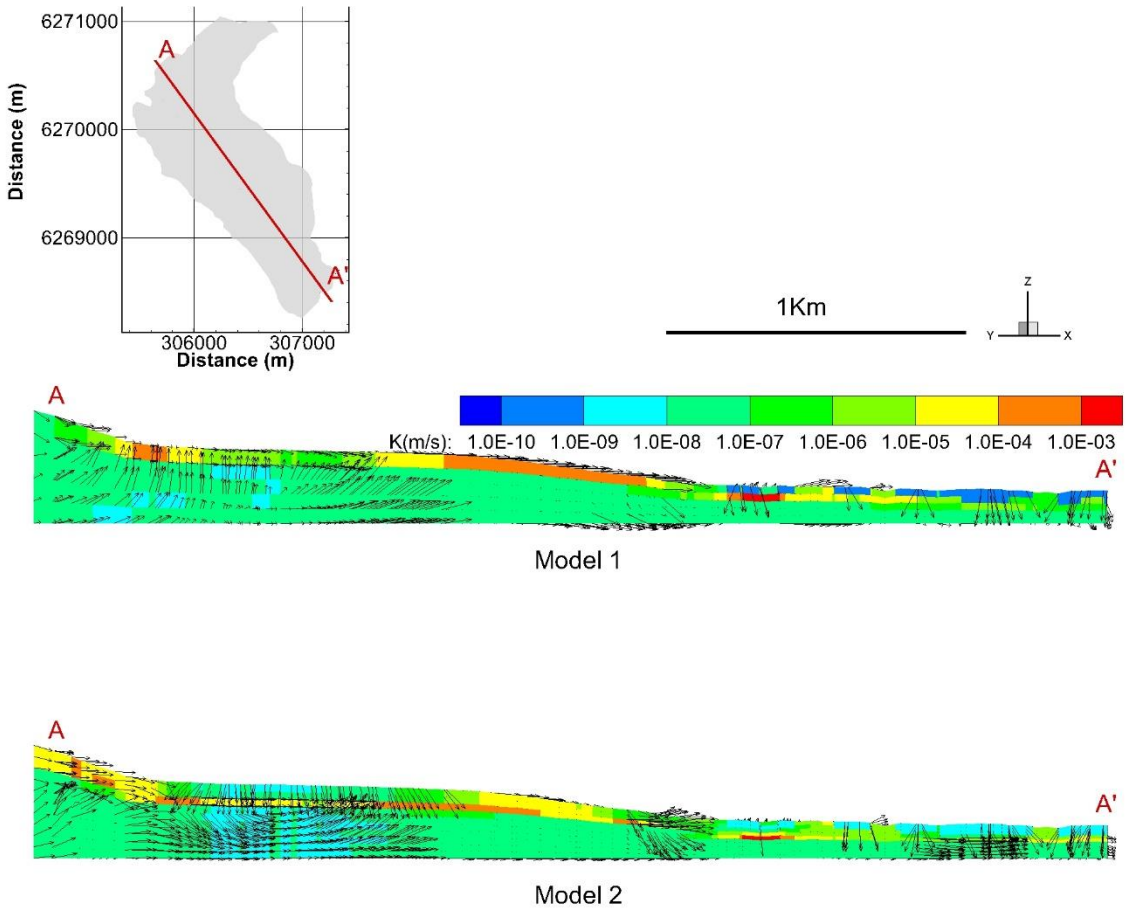

Figure 4.15 Calibrated hydraulic conductivity distribution and flow vectors from two models with different numbers of pilot-point layers. The presented cross-sections are not aligned with the flow direction, which means that there can be flow components perpendicular to the cross section.

The model uses the interpolation of values at pilot-points to calculate the hydraulic conductivity for each model element. When there are more pilot-points in the model, there are more points adjacent to each element. Therefore, in the PEST calibration, a greater range of hydraulic conductivity is included in the interpolation, to calculate the hydraulic conductivity for each model element. Consequently, the model can develop a more detailed subsurface structure and thus can more accurately include the permeable layer. Clearly, Model 2 shows a thin permeable layer under the layer with less permeability. This is in agreement with the actual subsurface structure, which contains a thin permeable layer of sand and gravel under the layer of lower permeability silt (Figure 4.2). In Model 1 with fewer pilot-points (5 layers), the calibrated hydraulic conductivity field is less refined.

For wells 04, 06 and 09, the model with 10 layers predicts heads very close to the observed data, while for the model with 5 layers, there are clear differences between the predicted and observed heads (Figure 4.16). For well 02, neither model can properly predict the observed data. However, for the model with 10 layers, the difference between the prediction and observation is less compared to the model with 5 layers. Therefore, it can be concluded that the model with 10 layers of pilot-points, which gave a better representation of hydrostratigraphy, yields better fits to the observed hydraulic heads.

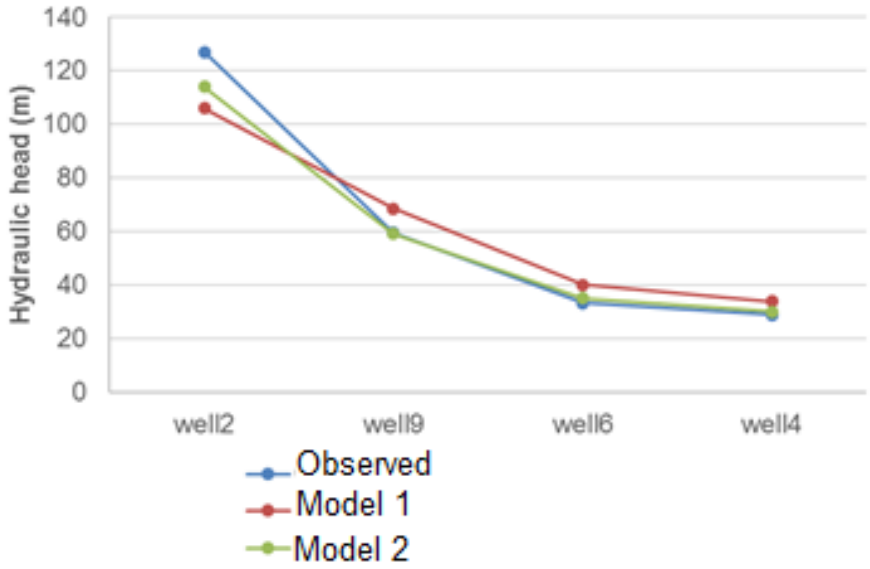

Figure 4.16 Comparison of simulated hydraulic heads under steady-state conditions using two pilot-point-zoning models against the observed values

Table 4.8 compares the coefficient of efficiency E and the mean absolute error (MAE) for the two models. The coefficient of efficiency, which ranges from minus infinity to 1.0, with higher values indicating better agreement, is defined as

$$CE = 1 - \frac{\sum_{i=1}^{N}|O_i - P_i|}{\sum|O_i - \bar{O}|} \quad (4\text{-}6)$$

while MAE describes the difference between the model simulations and observations in the units of the variable:

$$MAE = N^{-1}\sum_{i=1}^{N}|O_i - P_i| \quad (4\text{-}7)$$

where O_i, P_i and $\bar{O}$ are observed data, computed values and mean value of observed data, respectively and N is the number of observations.

The Model 1 with 10 layers produced significantly less error compared to Model 2 with 5 layers. In addition, the model with 10 layers is more efficient in calculating the hydraulic heads due to higher coefficient of efficiency.

Table 4.8 Comparison of model efficiency and error between models of different sublayers in the pilot-points zoning method

Number of sublayers	**5 layers**	**10 layers**
CE*	0.68	0.87
MAE (m)**	10.49	4.13

* Coefficient of Efficiency

** Mean Absolute Error

Although using a higher number of pilot-points improves the model efficiency, it increases the computation time. The number of pilot-points and thus the number of unknowns in the calibration was 275 and 550 for the model with 5 and 10 layers of pilot-points, respectively. In this simulation, PEST ran the model twice for each pilot-point. Therefore, Model 2 required twice the computation time than Model 1.

4.4.2 Sensitivity analysis

The model sensitivity analysis was performed in two stages. In the first stage, the sensitivity of the steady-state hydraulic heads with respect to the hydraulic conductivity of the geologic units was evaluated at the observation wells. In the second stage, the sensitivity analysis was conducted under transient unsaturated conditions by considering unsaturated characteristics, surface properties, specific storage and porosity.

Figure 4.17 shows the sensitivity of hydraulic heads to the hydraulic conductivity of the hydrostratigraphic units at the observation wells under steady-state flow conditions (the first stage). Sensitivity for each well is scaled by dividing the sensitivity of each parameter to the cumulative sensitivity. The sensitivities can be explained by considering the position of the wells with respect to their depth. For example, although wells 02 and 03 are both located at site 2 (Figure 4.1), they show different sensitivities to hydrostratigraphic unit properties. Well

02 is closer to the surface, in the sand layer, (Figure 4.2) and shows a higher sensitivity to the hydraulic conductivity of sand (approximate sensitivity of 50% to hydraulic conductivity of sand and 20% to hydraulic conductivity of silt). In comparison, well 03 is in the deeper silt hence shows a higher sensitivity to the silt layer properties (with a sensitivity of about 40% to the hydraulic conductivity of silt and 30% to hydraulic conductivity of the sandy gravel). It is worth mentioning that well 03 was eliminated in the following stages of the study due to poor well log data. Furthermore, well 04 is surrounded by permafrost mounds embedded in the silt, and thus shows a higher sensitivity to the hydraulic conductivity of the silt layer (50%). Overall, the calibration showed low sensitivity to hydraulic conductivity of permafrost and rock. The sensitivity to hydraulic conductivity of permafrost might be low because the permafrost blocks are discontinuous and dispersed throughout the catchment.

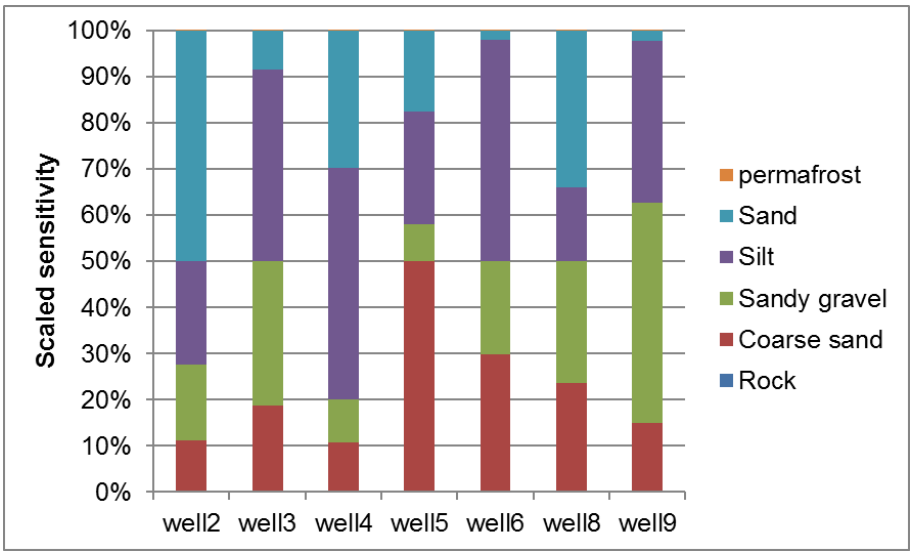

Figure 4.17 Sensitivity of hydraulic heads at observation wells to the hydraulic conductivity of each hydrostratigraphic unit, in the steady-state simulation

In the second stage, the sensitivity of hydraulic heads to the surface and subsurface parameters was computed for transient flow. Figure 4.18 shows the overall sensitivity of the model, obtained by PEST, to each variable. In general, the unsaturated van Genuchten parameters (α, β, and r_s) and hydraulic conductivities (K) show the most dominant effect on the hydraulic heads and water flow. The surface water flow parameters (i.e. coupling length and Manning coefficients) have the least effect on the hydraulic heads. This is because surface water flow only exists in the downstream part of the catchment, which is limited to wells 04, 06 and 09. It is worth noting that the overall sensitivity analysis has been conducted

for all wells including wells 03, 05 and 08. Later it became clear that these wells were either dry or frozen, thus including them in the sensitivity analyses could have introduced errors.

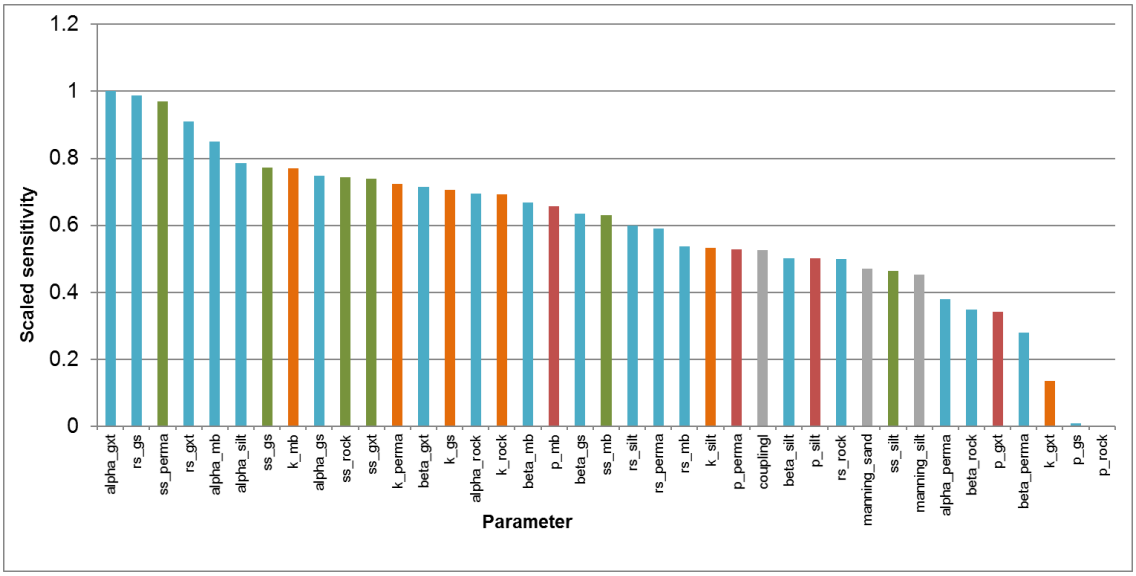

Figure 4.18 Sensitivity of the transient model to parameters in transient flow simulation.

Figure 4.19 compares the sensitivity analysis of wells 02 and 04. Well 02 is located in the upstream part of the catchment while well 04 is downstream. Figure 4.19 ranks the parameters from the most sensitive (at the bottom of the graph) to the least sensitive (at the top of the graph). The sensitivity percentage (relative to the most sensitive parameter) is shown by the bar thickness. It can be seen in Figure 4.19 that both hydraulic heads at well 02 and well 04 are sensitive to the subsurface van Genuchten parameters. However, the sensitivity of well 04 to surface water parameters such as the Manning coefficient and the coupling length is higher compared to well 02. For example, sensitivity to the Manning coefficient in the sand for well 04 is 6% versus 1.15 % for well 02. This is due to the fact that well 04 is located in the downstream part of the catchment where surface water flow is more significant. In addition, the sensitivity of well 02 and 04 in the transient flow simulation (Figure 4.19) shows a similar trend to the simulation under steady-state conditions (Figure 4.17). For example, both analyses show that well 02 is more sensitive to the hydraulic conductivity of the sand layer, whereas well 04 is more sensitive to hydraulic conductivity of the silt unit.

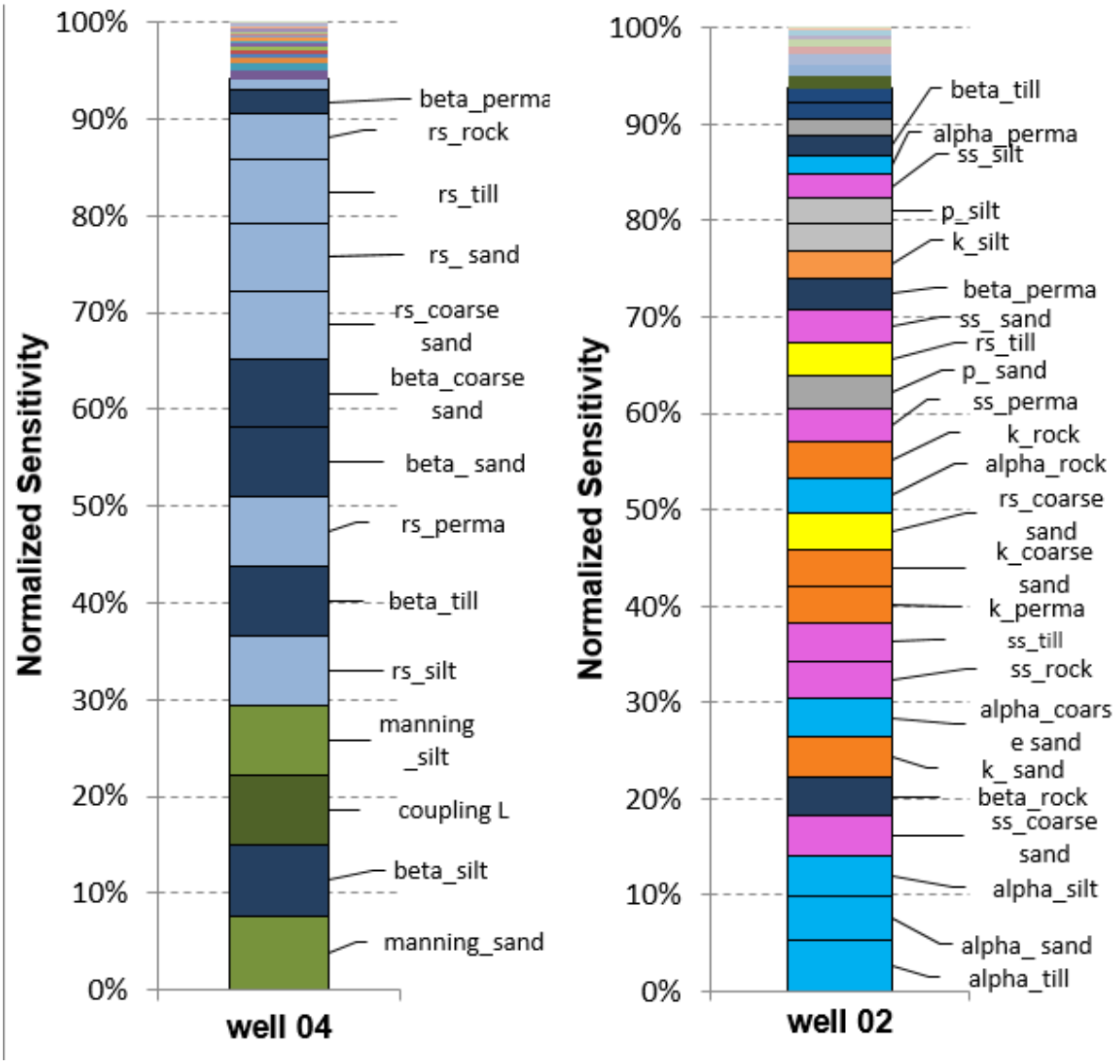

Figure 4.19 Comparison between the sensitivity results for hydraulic head at well 02 in the upstream part of the catchment and for hydraulic head at well 04 in the downstream part, using the transient simulation.

The computational effort required to calibrate the model for steady-state flow was much less than for transient flow. Furthermore, the calibration method (zoning, pilot-points, or pilot-points zoning) has a significant influence on the required computation time and CPU usage. Running the model in steady state and transient conditions required 5 seconds and 3-6 hours, respectively. PEST ran the model twice for each calibrating parameter. Therefore calibrating the model using a steady-state simulation and the zoning method required the

least amount of computation time, whereas the transient calibration using the zoning method required the most computation time among simulations explained in this chapter.

4.4.3 Additional simulation studies

Throughout the process of model calibration, the effects of several important choices regarding model set-up were tested, including those related to model structure, boundary conditions and applied field data. Although modifying these conditions did not improve the model calibration, they are briefly explained here.

- The measured precipitation data include errors, for example, due to the effect of wind. Initially the precipitation data were processed to consider these errors. However, the simulated results using the processed precipitation gave a poorer fit to observed heads compared to the model with the raw precipitation data. Therefore, the simulations were conducted using the raw data.
- The effect of the unsaturated water content curves on hydraulic heads was tested by using different unsaturated zone characteristics. These simulations aimed more specifically to improve the fit at well 09. However, even using extreme values for unsaturated zone characteristics did not have a significant effect.
- An alternative exit flow boundary condition was tested to try to improve the model efficiency, which included considering discharge from the subsurface boundary, at the nodes below the outlet. To produce subsurface discharge, a constant head boundary condition was applied to the nodes below the outlet. However, this assumption reduced the model efficiency.
- The measured hydraulic heads at well 02, located in the perched aquifer, were included in the calibration process. Due to the high dependency of these heads on the local subsurface structure, it was not possible to obtain a good fit to the observed heads.
- Surface parameters were initially included in more detail by taking into account different vegetation cover and surface obstruction. However, due to further complexity and higher computation time, these features were eliminated from the calibration process.

4.5 Summary and conclusions

In this study, a 3D coupled surface-subsurface flow model using the HGS code was developed for the cold-region study area of Umiujaq in northern Quebec, Canada.

The model was calibrated against the measured hydraulic heads and the hydrograph at the observation wells. Furthermore, sensitivity analyses were carried out to evaluate the sensitivity of the model to different surface and subsurface characteristics.

The mesh structure and the element size can have an impact of model calibration. For instance, the mesh should ideally be discretized very finely along the vertical dimension to represent the thin permeable layer below the silt layer in the downstream section of the model. However, generating a mesh with very thin vertical layers greatly increased computational times and made the simulation impractical. Therefore, a balance had to be found between generating a mesh that lead to reasonable run times and representing small-scale layers and heterogeneities.

For wells 04 and 06, located in the confined aquifer, the model predicts the fluctuations of hydraulic head time series better compared to well 09 in the unconfined aquifer. For well 09 the simulated heads show a poorer fit to the observation values.

Comparing the simulated and observed hydrographs shows that the model provides a better fit to the observed hydrographs in winter than in summer. This can be due to the controlling effects of surface properties, such as the Manning coefficient and obstruction storage on the surface runoff, which are more important in summer than in winter. Spatial variation of surface properties was not included in the model. As described in Section 2.2.5, the winter condition was considered by dividing the precipitation into liquid and solid phases. Assuming the solid phase to be immobile, the surface properties have less effect on the obtained hydrograph in winter.

Evaluating the sensitivity of the hydraulic heads at the observation locations shows that the wells in the downstream part of the study area are more sensitive to surface water properties (Manning coefficient and coupling length). This is due to the greater presence of surface water flow in the downstream part of the study area. Upstream wells are more sensitive to subsurface properties, for example to the hydraulic conductivity and specific storage. It should be noted that there is no permanent surface water flow in the upstream region. Also,

the model showed less sensitivity to rock and permafrost units. This can be because there is no water flow and observation in these units.

The water flow model explained in this chapter provides a basis for the coupled water flow-heat transport simulation of this PhD study, which is presented in Chapters 5 and 6. This is the first coupled 3D groundwater – surface water flow model developed for this catchment and includes realistic hydrostratigraphic units, which provides a more realistic 3D representation of the hydrogeologic flow system compared to previous studies of this study area. The model provides better results for hydraulic heads in the confined aquifer and in the stream hydrograph, than in the unconfined aquifer. However, a better fit to observed values can be obtained by further refining the representation of the geological units in the model and by using a finer discretization.

4.6 Recommendations and future studies

Based on the results of the flow model, the following additional investigations are suggested for future work:

- Apply more detailed surface characteristics (for instance considering the effect of different vegetation types) in the model to simulate surface water flow more realistically and improve the fit of the simulated hydrograph.
- Include a more detailed representation of the subsurface around wells 02 and 09, and refine the model around the unconfined and perched aquifers.
- Use a calibration method with more flexibility, for example pilot-points to improve the fit to observed heads and hydrograph values under transient conditions. However, calibrating the hydraulic conductivity values under transient conditions using pilot-points requires a fast CPU and more computation time.
- The effect of adding different number of pilot points around the permafrost units can be investigated to improve calibration by the pilot point- zoning method.
- Improve the quality of precipitation data in Umiujaq, which is an important input parameter in the simulation of water flow.
- Further investigation of the flow system in Umiujaq could be carried out using a finer discretization to obtain a better fit to observed head and hydrograph values.

5 Effect of spin-up in heat transport simulations at the catchment scale

5.1 Introduction

In integrated surface and subsurface hydrologic models, the choice of initial values for the independent variables, such as the initial soil moisture content or for dependent variables such as the subsurface temperature and heads, can affect the partitioning of water and energy (Rodell et al., 2004; Ajami et al., 2014). To reduce the impact of such initial conditions on simulation results, a model spin-up is initially required to reach equilibrium with respect to the water and energy balances (Wood et al., 1998), corresponding to a minimal artificial drift in the model state (Ajami et al., 2014). Seck et al. (2015) define the equilibrium state as a point at which the state of the model at the end of a current run is the same as that at the end of the previous run. The result from the model spin-up is then used as the initial state, or conditions, for subsequent simulations.

Ajami et al. (2014) and Seck et al. (2015) have investigated model spin-up and the impact of initial conditions on fluid flow simulations with integrated surface and subsurface hydrologic models. They proposed various strategies for model spin-up and identified the impact of boundary conditions on the choice of initial conditions. For example, Seck et al. (2015) showed that the occurrence of precipitation events reduces the influence of the initial condition on simulation results. Likewise, heat transport simulations also require careful selection of initial temperatures. Rühaak et al. (2015) and Dagenais et al. (2020) used binary temperature distributions – a uniform initial background temperature for the thawed regions and a uniform initial temperature for the permafrost blocks - to simulate heat transport in permafrost systems susceptible to freeze and thaw. In Dagenais et al. (2018, 2020), the initial condition was set in the year 1900, far enough away in time from the calibration period (~ 110 years) such that the assumed initial temperature condition, at least outside of the permafrost zones where T>0, would have less effect. The initial permafrost distribution (where T<0) was also very important to the calibration since permafrost still exists in the study area. The initial time t=0 was also about 50 years before any observed air temperatures were available.

Rock and Kupfersberger (2018) developed a 3D heat transfer model for a shallow aquifer. They derived the initial groundwater temperature in their 3D heat transport model from the average observed temperatures during the simulation period. In Shanafield et al., (2016), initial temperatures were calculated from average observed temperatures at given depths in the subsurface. They were thus able to capture the warmer antecedent temperatures observed in the deepest parts of the subsurface, prior to the modelling. Smith and Riseborough (2010), Frampton et al. (2011), and Tiliță et al. (2018) used a steady-state temperature distribution as the initial condition for transient heat transfer simulations.

Previous studies on the effect of initial conditions on an integrated model have mostly focused on water flow models. Langford et al. (2020) has compared steady-state and transient scenarios in obtaining the initial condition in modeling permafrost thaw. Their results show that a model initialized with transient spin up yields better results than steady-state permafrost initial condition. The aim of this study was to compare the effect of different initializations in the transient state, which are commonly used in basin-scale simulations of heat transport, and to introduce a method to reduce the effect of imposed initial temperatures on the subsequent simulations.

The first objective of this study was to compare the effect of different strategies commonly used as the initial condition in the heat transfer simulations. The second objective of this study was to determine how best to reduce the effect of initial temperature assumptions in the heat transfer model and compare the results to previous methods. A coupled water flow and heat transport model of a real study site was developed to test the effect of these initial temperature conditions. This model was used to study the resulting system dynamics as a function of initial conditions and the relative impact of initializations on variables of interest.

5.2 Methods and materials

5.2.1 Study area

The study area is a catchment in the Tasiapik valley near the village of Umiujaq, within the discontinuous permafrost zone in northern Quebec, Canada (Figure 5.1). The valley is bordered by a cuesta and the Umiujaq hill on its southwest and northeast sides, respectively. The catchment covers an area of 2.23 km^2 and contains a small stream that flows into Tasiujaq Lake. A steep slope connects the relatively flat upstream and downstream parts of

the valley and the elevation difference reaches 100 m between the upstream and downstream parts.

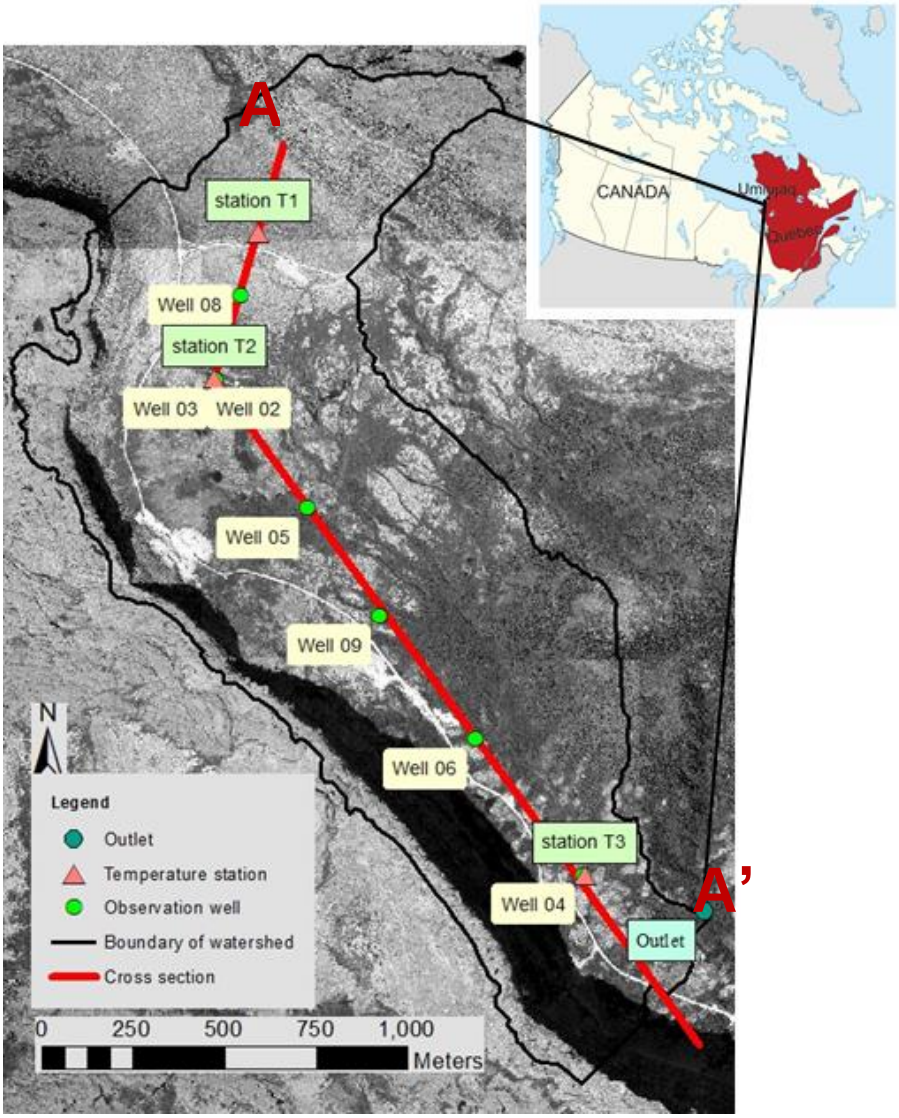

Figure 5.1 Catchment boundary and location of measurements. The red line shows the location of the vertical cross-section A-A' shown in Figure 5.3.

The regional climate is subarctic with cool and damp summers and relatively dry and cold winters. Hudson Bay has a major influence on the regional climate due to the strong winds in winter when the bay is frozen and due to the dense fog in summer. Measured air temperature, precipitation, and land surface temperature for the catchment for the period 6th July 2014 to 5th July 2017 are shown in Figure 5.2. The mean annual air and land surface temperatures for this period were -4.5 and 0.6 °C, respectively. Generally, the period

between October and April is the coldest, with average negative temperatures, and temperatures above zero are typically from May to September. The mean annual total precipitation, rain and snow, was 760 mm for the period 2014-2017.

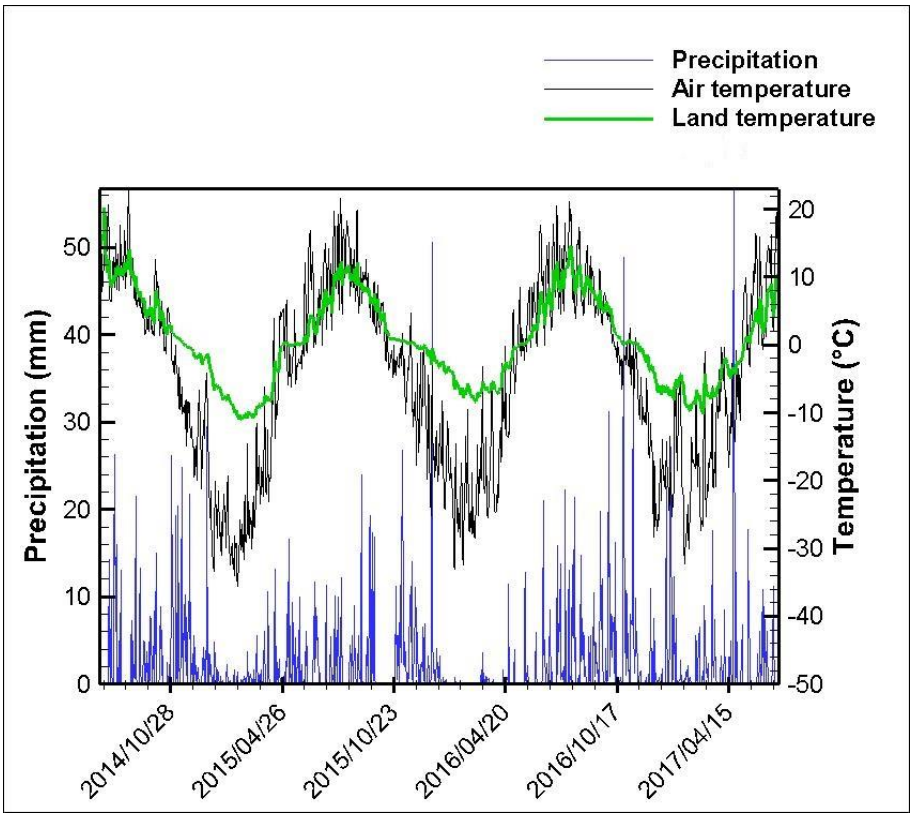

Figure 5.2 Measured air temperature, precipitation, and average land surface temperature in Umiujaq for the period of 6th July 2014 to 5th July 2017

Detailed geological and hydrogeological field investigations have been conducted in the catchment since 2013. Six distinct hydrostratigraphic units have been identified and are shown in Figure 5.3 for a vertical cross-section. The bedrock is overlain by a till unit, which consists of moraine deposits. The till is overlain by a coarse sand unit, which is in turn overlain by a marine silt unit. This silt unit is thicker towards the downstream part of the catchment and it is not present over the whole catchment. Permafrost blocks are irregularly distributed with the silt unit, predominantly in the thickest part of the silt unit downstream of the catchment. Finally, a thin sand unit, consisting of littoral and intertidal sediments, covers the upstream part of the catchment.

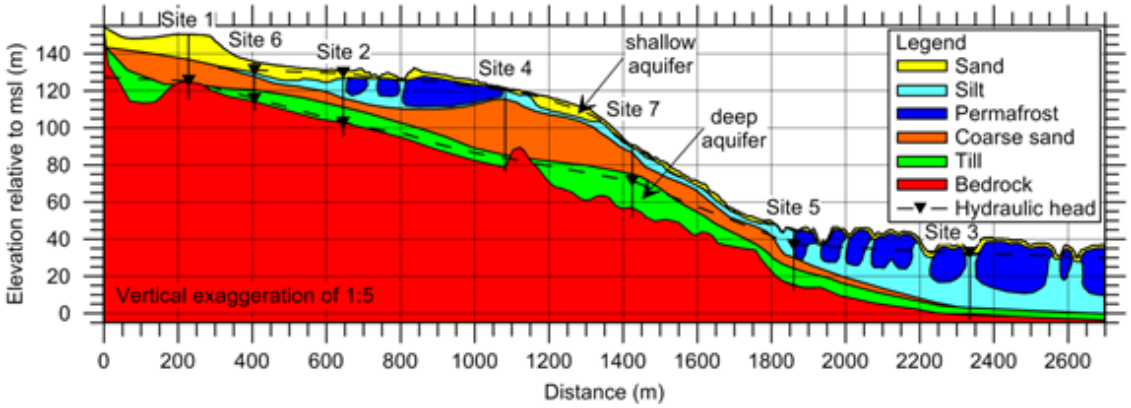

Figure 5.3 Vertical cross-section A-A' showing the hydrostratigraphic units (Fortier et al., 2019).

A gauging station was installed near the stream outlet and seven observation wells were installed within the catchment (Figure 5.1). Three multi-level temperature stations, stations T1, T2 and T3 shown in Figure 5.1, measure subsurface temperatures down to a depth of 35 m. Furthermore, the land-surface temperature is monitored with 38 probes installed at a depth of 10 cm and located throughout the catchment (Figure 5.4).

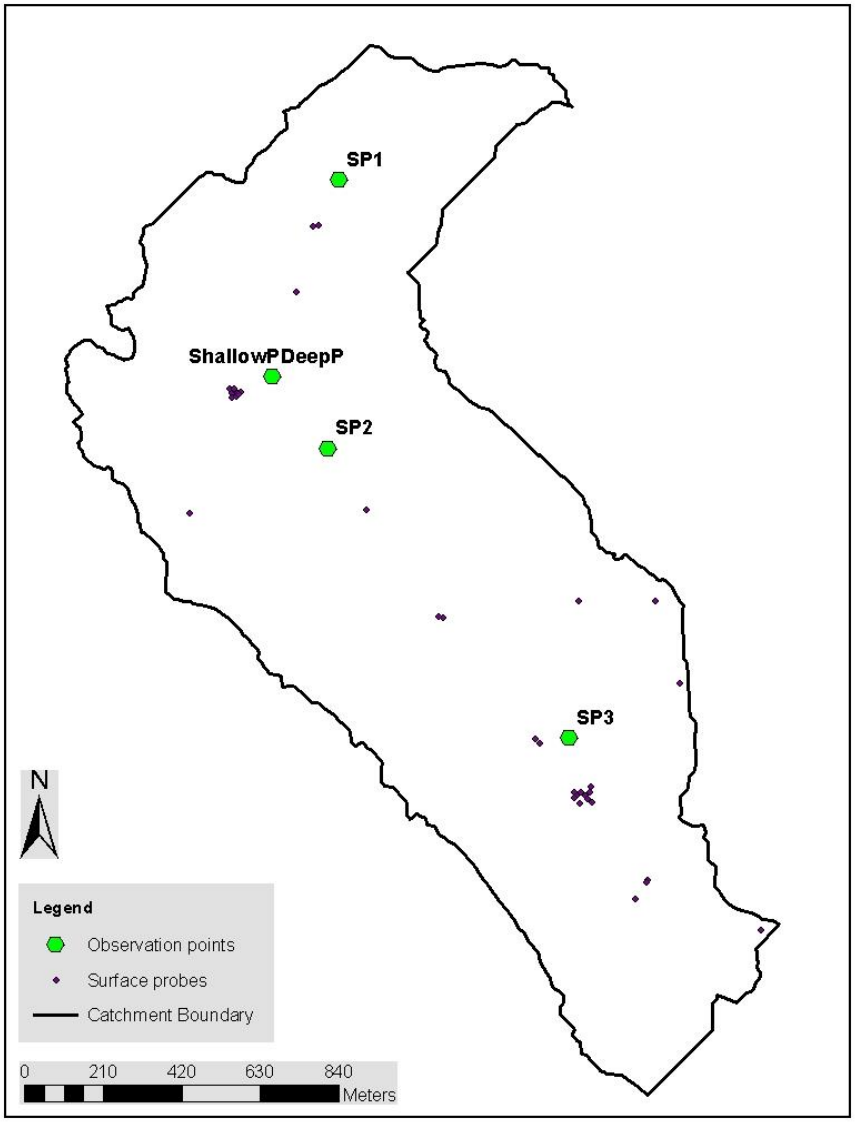

Figure 5.4 Location of surface probes and fictitious observation points

5.2.2 Numerical model

The coupled 3D water flow and heat transport model was developed with the HydroGeoSphere (HGS) code. HGS solves 2D surface flow, using the diffusion wave approximation, simultaneously with 3D variably-saturated groundwater flow, using Richards' equation. Freeze-thaw and latent heat were not included in the simulation, however, the effect of solid precipitation was differentiated from liquid precipitation, as discussed in section 2.2.5. The control volume finite element method is used to discretize the flow equations, which are solved iteratively with the Newton-Raphson method. Using the

computed flow solution at a given time step, the model solves advective-conductive heat transport for both the surface and subsurface domains. The governing equations for variably-saturated flow and heat transport, and their implementation in HGS, are described in detail in Aquanty (2017).

5.2.3 Model conceptualization

5.2.3.1 Model parameters

The catchment boundary, land elevation and the location of streams were defined by processing the digital elevation model using ArcGIS. The surface of the catchment was discretized with the automated 2D triangular mesh construction procedure described by Käser et al. (2014). The resulting 2D mesh contains 1,703 nodes and 3,205 triangular elements. To generate the 3D subsurface mesh, the 2D mesh was replicated along the vertical direction, with a finer vertical spacing close to ground surface. A total of 30 sublayers were generated along the vertical direction, with 20 sublayers equally spaced between ground surface and a depth of 5 m, and 10 sublayers equally spaced between a depth of 5 m and an elevation of -40 m. The resulting 3D mesh contains 52,793 nodes and 96,150 triangular prism elements.

A GOCAD model was developed to represent the 3D spatial distribution of the six hydrostratigraphic units described above (Fortier et al., 2019 and Banville, 2016). A Python code was used to map the spatial distribution of the units in the GOCAD model onto the HGS 3D subsurface mesh. Hydraulic conductivities of the units were obtained from calibration according to the method described in Chapter 4. Unsaturated properties were calculated from grain size distributions with the Rosetta Software. Thermal conductivity and specific heat capacity were measured in the field using transient thermal conductivity probes and TDR antenna (Buteau, 2002). Hydraulic and thermal properties for the units are shown in Table 5.1. In the numerical simulations carried out with HydroGeoSphere, the temperature is assumed to have an impact on both fluid density and viscosity (Aquanty, 2017). However, the simulations did not account for soil freeze-thaw cycles and the effect of latent heat.

Table 5.1 Hydraulic and thermal properties of the hydrostratigraphic units

	Hydraulic properties			Unsaturated van Genuchten properties			Physical and thermal properties	
	Hydraulic conductivity (m/s)[1]	Specific storage[1](1/m)	Porosity[3]	α[2]	β[2]	Thermal conductivity - [3,4](J/m/s/°C)	Specific heat [3] (J/kg/°C)	Bulk density[5] (kg/m^3)
Sand	1.74E-4	1E-4	0.3	3.7	3.6	2	2480	1690
Silt	1E-6	2E-3	0.4	1.6	1.4	1.9	2550	2100[3]
Sandy gravel	1.08E-5	1E-4	0.35	3.7	3.6	2	2480	1690
Gravel	1E-5	1E-4	0.25	3.6	4.1	2	1764	1912
Rock	2.7E-10	1E-6	0.002	1.6	1.4	2.28	1340	2800
Permafrost	6.74E-8	-	0.002	1.6	1.4	2.6	1980	1600[3]

[1]Calibration; hydraulic conductivity represents the unfrozen, saturated value
[2]Rosetta Software, based on grain distribution
[3](Buteau, 2002); representing bulk values of the porous medium under saturated conditions
[4](Dagenais *et al.*, 2017)
[5](Leblanc, 2013)

5.2.3.2 Boundary conditions

Evapotranspiration was calculated manually and subtracted from the precipitation time series to obtain the net precipitation. The daily net precipitation (total precipitation minus evapotranspiration) was applied to the surface flow domain as a top flux boundary condition. A critical depth boundary condition for surface flow was assigned to the outlet of the catchment. For the subsurface, the boundaries were assumed to represent either groundwater flow divides or impermeable boundaries and were thus represented as no-flow boundaries (Figure 5.5).

For surface heat transport, the observed transient temperatures at land surface were applied as a first-type boundary condition to the surface nodes. Land surface temperatures were obtained by computing the average of the soil temperatures measured by probes installed close to the surface (Figure 5.4). As a result, the spatial distribution of land surface temperature was assumed constant. For every time step, the average temperature measured by the probes at the corresponding time was assigned to the surface of the entire catchment. The assigned surface temperature was therefore temporally variable. Heat

transfer between the land surface nodes and porous media nodes occurs through the dual node condition. The dual-node approach uses a first-order flux relation to transfer heat between surface and subsurface. The lateral subsurface boundaries were assigned a zero temperature gradient, which assumes that horizontal conductive heat transport across the boundaries is negligible. A geothermal flux of 0.032 W/m^2 was applied along the bottom boundary, consistent with the value presented in Buteau (2002).

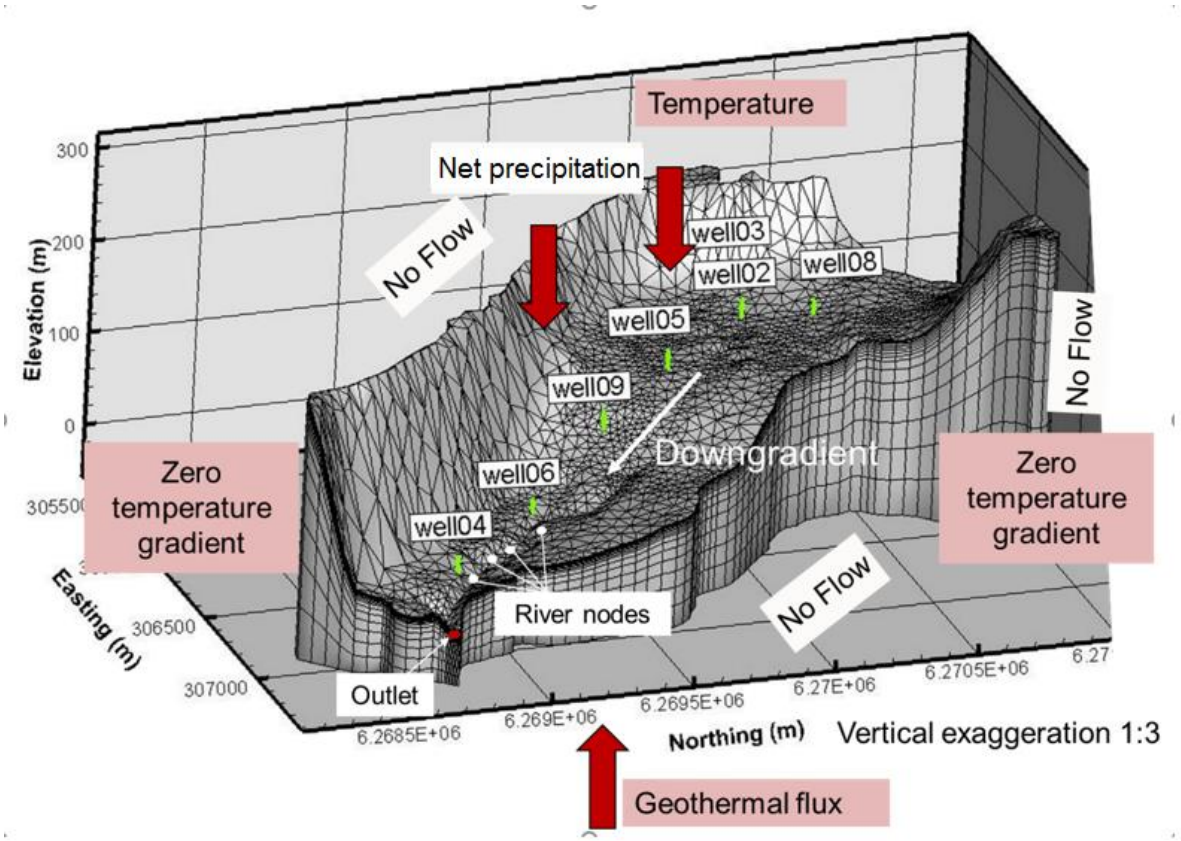

Figure 5.5 Boundary conditions applied for heat transport and water flow simulations.

5.2.4 Initial conditions and model spin-up

For the coupled surface water and groundwater flow simulation, a two-step spin-up was used. To eliminate the initial condition of water flow affecting the results, a spin up simulation was done for the water flow model before adding the heat transport simulation. Therefore, the flow model was first run to steady state with a constant precipitation rate equal to 1.9 x 10^{-8} m/s (approximately 600 mm/year) applied to the surface flow domain, which corresponds to the average annual precipitation. Using these steady-state flow results, the flow model was then run for one year with the raw precipitation data over the period of 6th

July 2013 to 5th July 2014, after manually accounting for evapotranspiration (the raw precipitation data is discussed in more detail in Chapter 4). This second flow simulation provided the initial conditions for the surface water depth and hydraulic heads for the three-year coupled flow - heat transport simulations (6th July 2014 to 5th July 2017) using different initial temperature conditions.

Since one objective of this study was to investigate the impact of initial temperatures used for the heat transport simulations, the following four scenarios were considered for the three-year coupled simulation:

1) A uniform temperature of -5°C was assigned initially to the subsurface, corresponding to cold initial conditions (scenario IC-5).
2) A uniform temperature of +5°C was assigned initially to the subsurface, corresponding to warm initial conditions (scenario IC+5).
3) A depth-variable temperature profile was assigned initially to the subsurface (scenario ICProfile). The profile was computed by assuming a temperature of 5°C at ground surface and an increase of 0.016°C/m with depth, computed from the average geothermal flux and thermal conductivity equal to 0.032 W/m^2 and 2.0 W/m°C, respectively.
4) In contrast to the previous scenario, the fourth scenario involved a model spin-up for the heat transport simulation, until equilibrium was reached (scenario ICSpin). The spin-up step started from an initial temperature of -5°C and continued until equilibrium. The equilibrium state is considered to be achieved when the change in stored energy (for example the energy stored in the first day of the first year minus the energy stored in the first day of the second year) is constant, and the relative change in energy stored after a year of simulation is less than 0.5%. The final computed temperatures were then used as initial temperatures for the three-year simulation.

The initial temperature of the permafrost units in all simulations was set to -2.5 °C, which corresponds to their average measured temperature (Buteau, 2002).

Since the model fully couples water flow and heat transport, these processes were run simultaneously to obtain the initial flow and temperature conditions in the ICSpin scenario. However, for the three other simulations without spin-up for heat (i.e., IC-5, IC+5, and ICProfile), the two-step spin-up was carried out for water flow, before simulating heat

transport. By doing so, the effect of not having spin-up for water flow is eliminated and the investigation was restricted to the effect of initial temperature only.

5.2.5 Persistence of the impact of initial temperatures

To study the persistence of initial subsurface temperatures, the first two scenarios corresponding to the cold and warm starting conditions (scenarios IC-5 and IC+5) were used in a new simulation. The two-step spin-up for water flow was applied to both simulations and the models were run for 40 years. For both scenarios, a single heat transport simulation was run recursively for a one-year period corresponding to 6th July 2014 to 5th July 2015, using the corresponding meteorological data. The model was assumed to reach equilibrium, or pseudo steady-state, when the difference in total energy stored in the catchment was less than 0.5% between two recursive (year-long) runs. The spin-up time was quantified with a percent-based cut-off time (PC time, Goncalves et al., 2006), which is defined as the time necessary for yearly changes in averaged model parameters to reach the equilibrium state.

5.2.6 Numerical solution parameters

For the flow simulations, the Newton-Raphson absolute and residual convergence criteria were 1 x 10^{-3} m and 1 x 10^{-3} m^3/s, respectively. A target variation of 1 m in hydraulic head between successive time steps was specified for the adaptive time stepping (Therrien *et al.*, 2010) and the time step size was limited to 1 day. The models were run in parallel mode on a 32.0 Gb RAM workstation with 4 CPU cores at 3.20 GHz. The total simulation time varied from 1 day to 7 days for each model run.

To evaluate the impact of the initial temperatures for all scenarios, three model observation points (SP1, SP2, SP3) were located in the upstream, middle and downstream portions of the catchment, at 5 meters below ground surface (Figure 5.4). Two additional observation points (ShallowP and DeepP) were located at the same horizontal location as observation well 2 but at depths of 3.77 m and 31 m, respectively, to assess the vertical variability of simulated temperatures (Figure 5.4). The total subsurface energy storage was also computed to assess the impact of initial temperature at the scale of the entire catchment.

5.3 Results

5.3.1 The impact of initial temperatures (Scenarios IC-5, IC+5, ICProfile)

Simulated temperatures at the three observation locations (SP1, SP2, and SP3) for the three-year period are shown in Figure 5.6a for scenarios IC-5, IC+5, and ICProfile. The results shown in Figure 5.6a clearly indicate that the simulated temperatures depend on the initial temperatures assigned to the subsurface. The scenario with the colder initial temperature (IC-5) produced simulated temperatures lower than for scenarios with higher initial temperatures (IC+5 and ICProfil). On the other hand, simulated temperatures for scenario IC-5 tend to increase with time at the observation points, while they decrease for the other two scenarios. Figure 5.6a shows that the simulated time-series tends toward an equilibrium temperature between the initially assumed temperatures at these locations. This causes the temperature time series to decrease for IC+5 and ICProfile and to increase for IC-5. Furthermore, the rate of temperature change for IC-5 is lower than for IC+5 and ICProfile, suggesting that equilibrium temperatures are closer to the IC-5 initial temperatures.

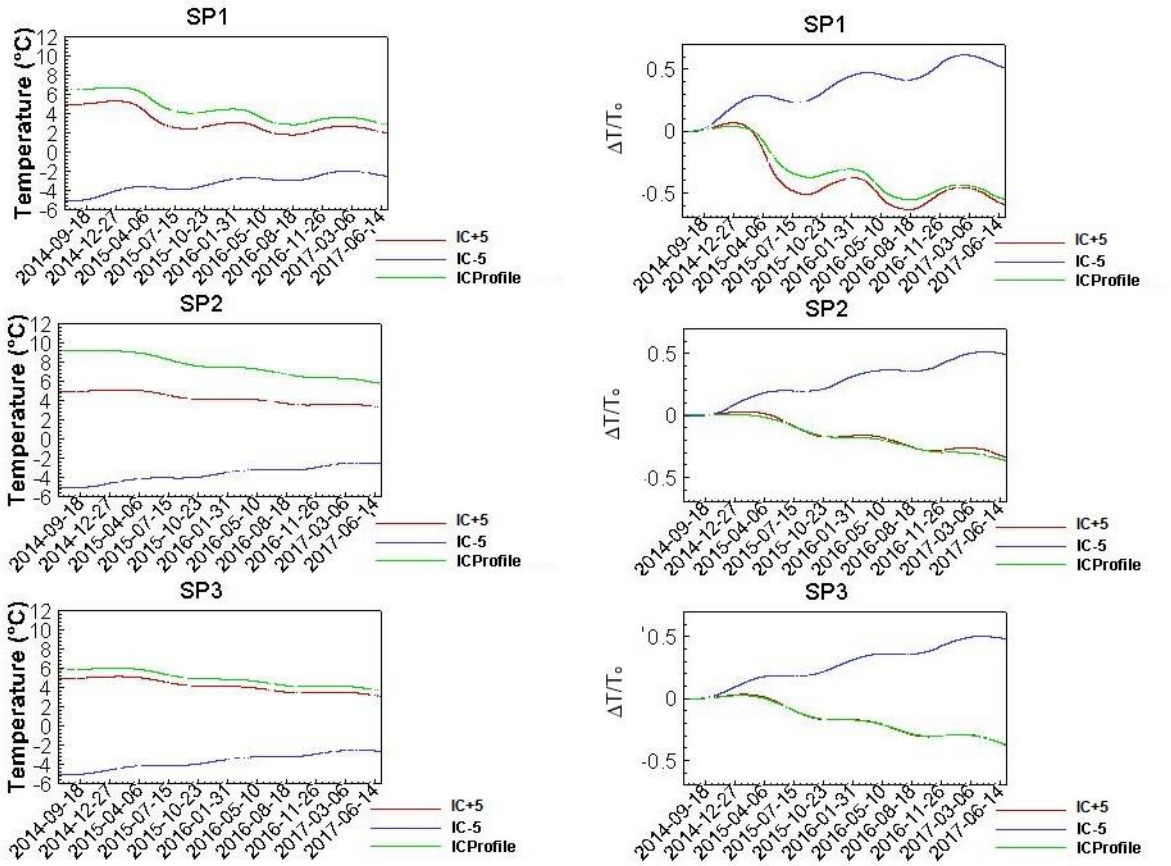

Figure 5.6 Simulated results showing a) temperatures and b) relative temperature changes (see Eq 5-1) at the three model observation points (SP1, SP2 and SP3) for scenarios IC+5 (red), IC-5(blue), and ICProfile (green).

A relative temperature change was also calculated with the following equation:

$$Relative\ Change = \frac{T - T_{initial}}{|T_{initial}|} \quad (5\text{-}1)$$

where $T_{initial}$ is the initial temperature for each scenario (i.e., -5°C, 5°C or the initial temperature at the observation points for ICProfile) and T is the simulated temperature. The relative temperature change, shown in Figure 5.6b for the three observation locations and the three scenarios, reveals a different temporal dynamic for the warm and cold initial temperatures. For example, the relative temperature change increases for IC-5 for the period between the end of January to May, while it initially stays constant and then slightly decreases for ICProfile and IC+5.

The temporal variations in simulated temperatures can be explained based on the temperature difference between the surface and subsurface domains. For scenarios IC+5

and ICProfile, the subsurface was initially warmer and the temperatures tended to decrease with time and would have eventually reached equilibrium. The model therefore loses heat from the subsurface to the surface. During the cold seasons, since the temperature at the surface is lower than the temperature in the subsurface, heat is transferred from the subsurface to the surface, which decreases subsurface temperatures. On the other hand, for scenario IC-5, the model mostly gains heat due to the lower initial subsurface temperature. For example, when temperatures at land surface are above -5 °C in winter, the subsurface domain is still colder than the surface domain, which causes heat transfer from the surface to subsurface. Once the surface temperature drops below the subsurface temperature, heat transfer is reversed and the subsurface temperature decreases. Therefore, the temperature change in IC-5 is less in winter compared to IC+5 and ICProfile.

The simulated temperatures at two different depths are shown in Figure 5.7 for the three scenarios IC-5, IC+5 and ICProfile. ShallowP is located close to ground surface and the simulated temperatures show temporal variations similar to the ground surface temperature assigned to the surface domain. The thermal dynamics at ShallowP are also similar to that at SP1, SP2, and SP3 located above the seasonal depth (the depth below surface where variation in land-surface temperature has an effect). In contrast, since the change in surface temperatures does not penetrate below the seasonal depth, the simulated temperature at DeepP remains constant and equal to the initial temperature for three years of simulation.

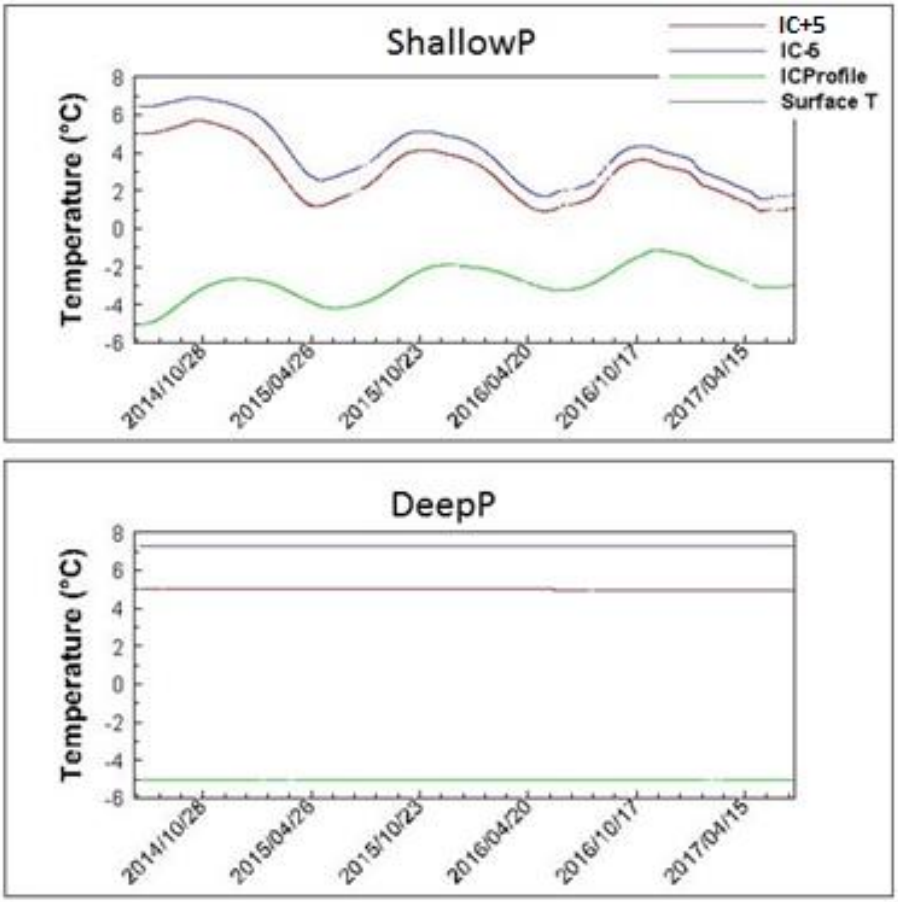

Figure 5.7 Simulated temperatures at ShallowP and DeepP for scenarios IC-5, IC+5, and ICProfile.

The total change in energy stored was used as an indicator of the overall state of the model. The relative change in total energy stored (∆Er) in the catchment is shown in Figure 5.8. The relative change in energy (∆Er) was obtained using the following equation:

$$\Delta \mathrm{Er} = \frac{\Delta E - \Delta E_{initial}}{|\Delta E_{initial}|} \tag{5-2}$$

where $\Delta E_{initial}$is the total energy stored at the beginning of the simulation.

For the three scenarios, ∆Er decreases after 3 years of simulation because the subsurface thermal condition tends towards thermal equilibrium with time. The comparison of ∆Er for IC+5 and IC-5 shows an inverse system response to imposed surface temperature. During the cold season, approximately from October to May, the energy stored for IC+5 and ICProfile decreases, while it increases for IC-5. The opposite happens in summer, from approximately June to September, when the energy stored decreases for IC-2 and increases

for IC+5 and ICProfile. This is the effect of temperature differences between the surface and subsurface. When the temperature difference is lower, the energy stored is lower and vice versa.

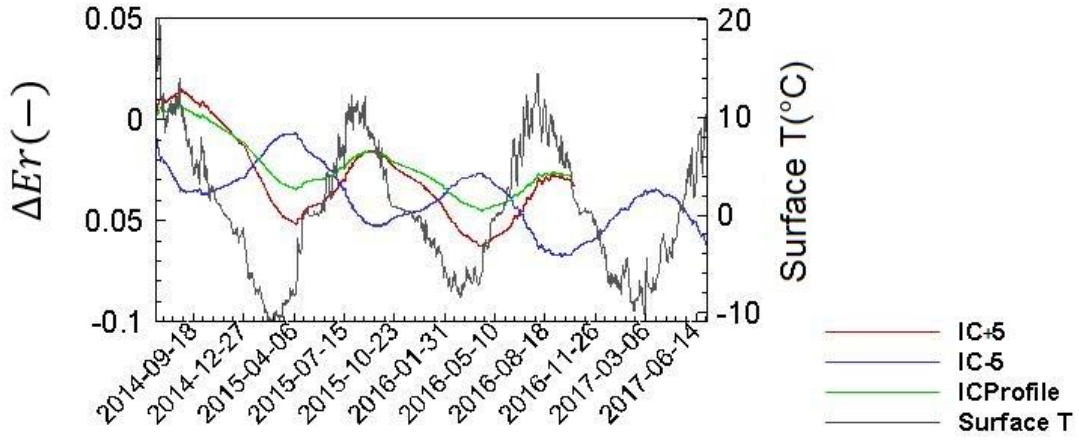

Figure 5.8 Relative change in energy stored for the different scenarios, as well as surface temperature.

5.3.2 Persistence of the effect of the initial temperature

As mentioned previously, for both IC-5 and IC+5 scenarios, the model was run in 40-year recursive simulations with runs of 1-year meteorological data to obtain the spin-up trends for the cold (IC-5) and warm (IC+5) initial conditions. For these 40-year simulations, the total energy stored decreases for both scenarios (Figure 5.9a and Figure 5.9c). The magnitude of the energy change between consecutive years becomes smaller as the number of simulated years increases.

The difference in energy stored in the first day of each simulated year was calculated for IC-5 and IC+5 which are shown in Figure 5.9b and Figure 5.9d as percent differences (For example the energy stored in the first day of the first year minus the energy stored in the first day of the second year). The energy stored drops by 1.4% in the first year of simulation for IC-5, whereas it drops by 2.2% for IC+5. While the rate of yearly energy change is higher for IC-5 than for IC+5 in the initial years, the difference diminishes significantly throughout the 40 years.

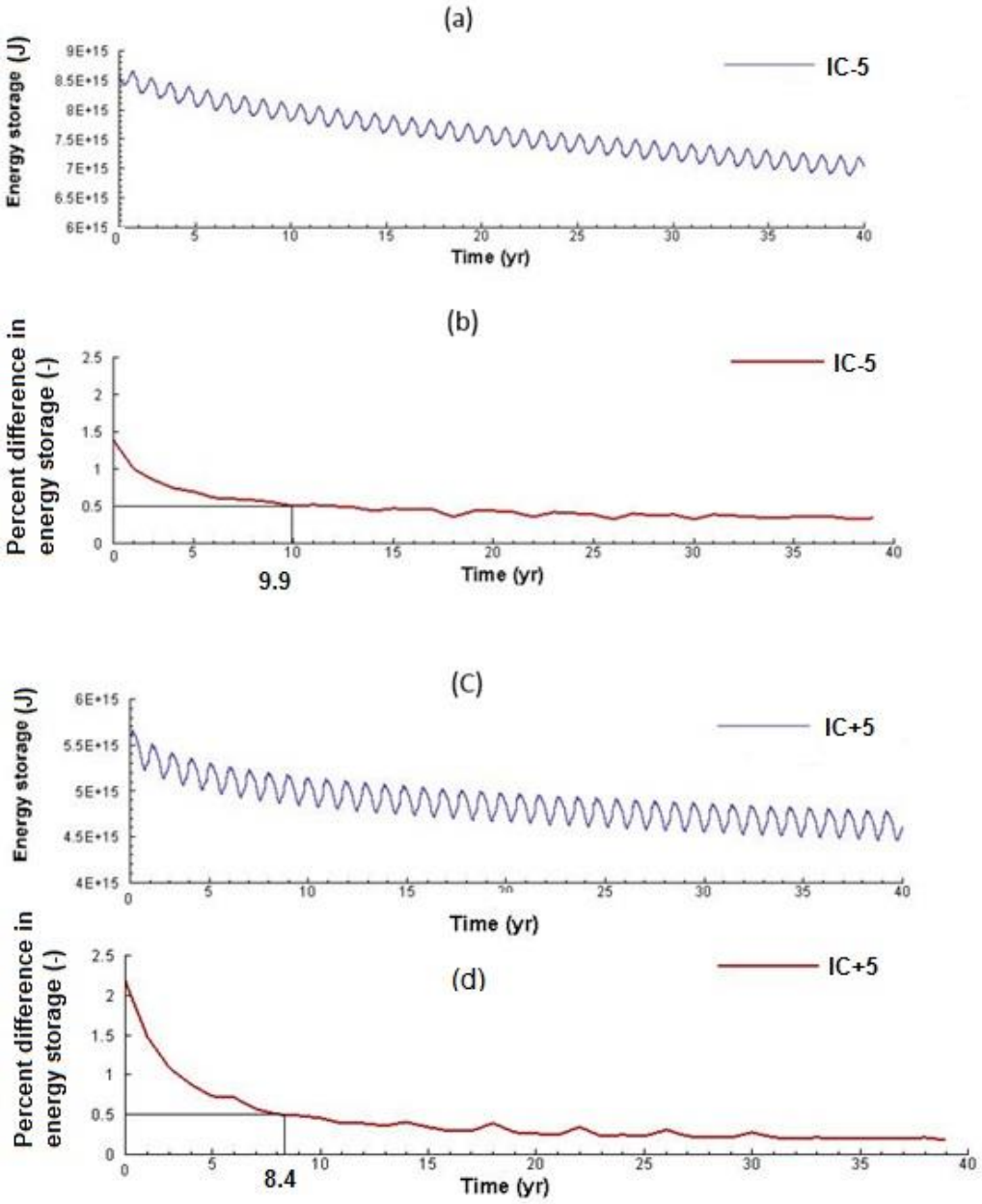

Figure 5.9 Persistence of the effect of initial condition for IC-5 and IC+5.

Using the criterion mentioned previously that thermal equilibrium is assumed to have been reached when the relative (percent) difference in energy storage between recursive (yearly) runs is less than 0.5%, scenarios IC-5 and IC+5 reach equilibrium state after 9.9 years and 8.4 years, respectively. By the 40th year, the percentage difference drops to 0.3% and 0.2%, respectively. The rate of energy drop is sharper at the beginning of the simulations and it becomes smaller towards the end.

As described above, it took the IC-5 scenario approximately 10 years to reach equilibrium. Since the model ICSpin (explained in Section 5.2.4) started from an initial temperature of -5 °C, the model was run for 10 years to reach equilibrium. At this stage, it was assumed that the model ICSpin is in equilibrium. At this stage of the model ICSpin, the variable temperature of July 2014 to July 2017 was applied to this model and the results were compared to other scenarios, as explained in Section 5.3.1.

5.3.3 Evaluating the effect of model spin-up on the simulated thermal regime

The simulated temperatures for the ICSpin scenario for the three-year period (6th July 2014 to 5th July 2017) are shown in Figure 5.10 for the three model observation locations SP1, SP2, and SP3. Since the model was initially at thermal equilibrium after the spin-up step, the average temperature for the three-year period remains almost constant. This result is different than that for the other 3 scenarios, without spin-up, where the simulated temperatures either showed an increasing or decreasing trend, depending on the choice of initial temperatures (Figure 5.6).

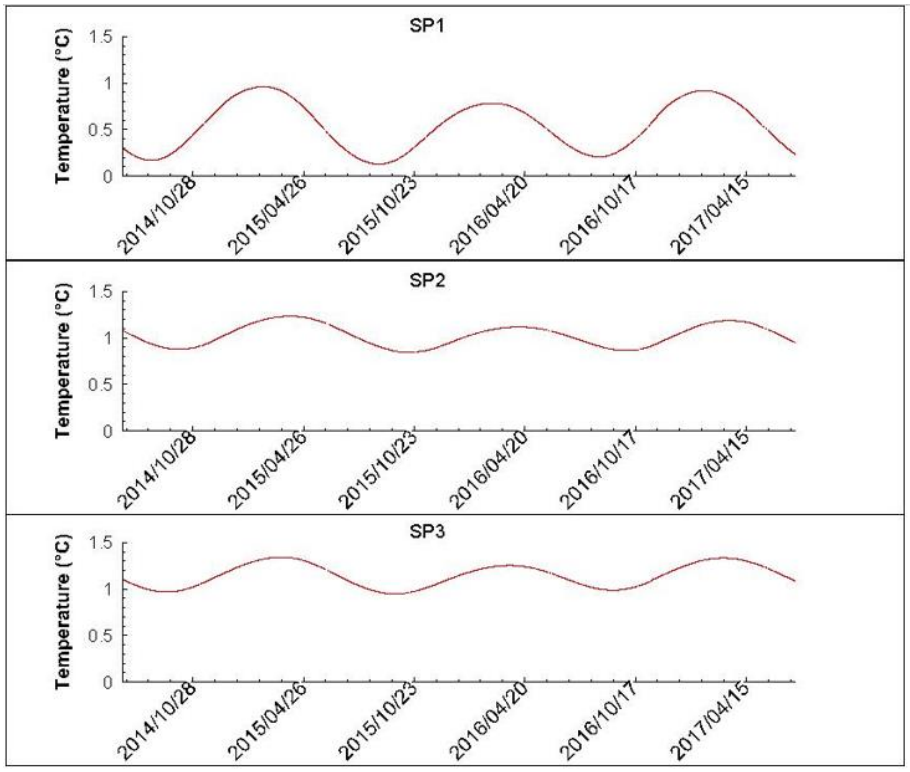

Figure 5.10 Simulated temperatures for scenario ICSpin at three observation locations for the period 6th July 2014 to 5th July 2017.

The observed and simulated temperatures at stations T1 and T2 are shown in Figure 5.11 for March (cold month) and September (warm month) in 2015 and 2016. Overall, the ICSpin scenario provides a better fit to the observed temperatures, especially below the seasonal depth (approximately 6 m). The results show that the models without spin-up tend toward the initially assumed temperatures at depths below 6 m (the seasonal depth), regardless of the initial temperature. For instance, IC-5 and IC+5 tend to -5°C and 5°C, respectively, below the seasonal depth.

Since the initial temperatures for the ICProfile scenario were not in equilibrium with the heat transport boundary conditions, this scenario gave a poor fit to observed temperature profiles.

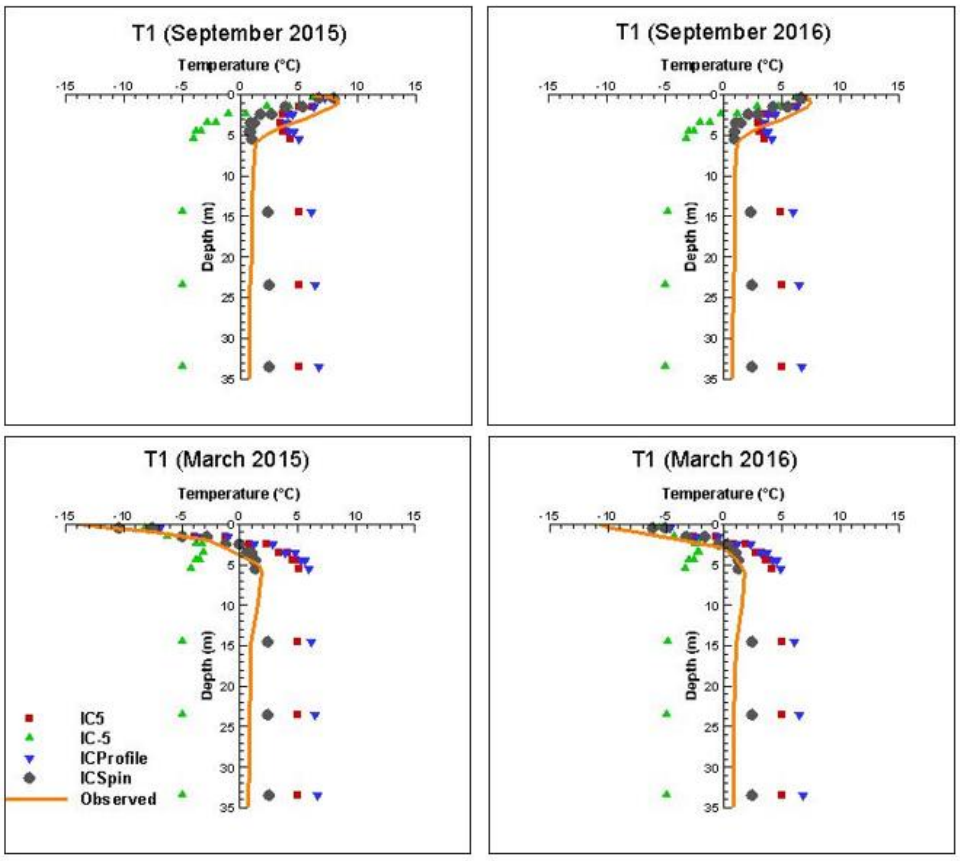

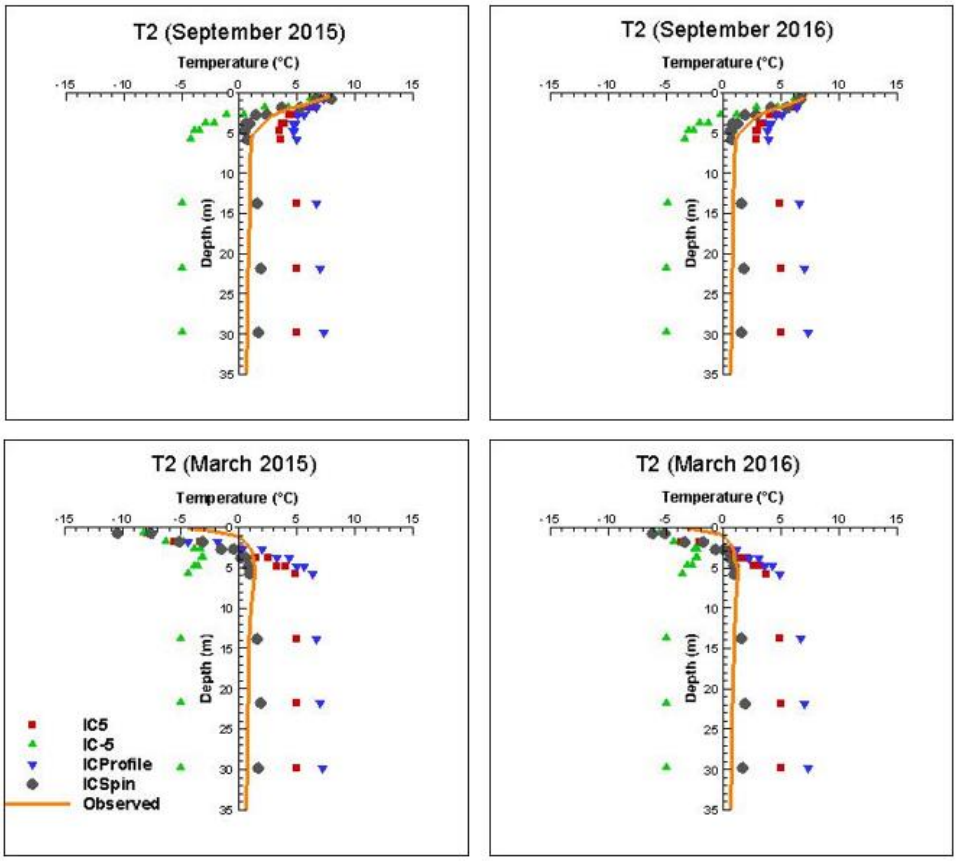

Figure 5.11 Observed and simulated temperature profiles in March (cold month) and September (warm month) 2015 and 2016 at T1 and T2 for IC-5, IC+5, ICProfile, and ICSpin.

5.4 Discussion

The simulations show that the initial temperature condition assigned to the model affects subsequent simulated temperatures, since the thermal dynamics between the subsurface and surface domains depends on their temperature difference. Heat migrates from warmer domains to cooler domains and the amount of exchanged heat is proportional to the temperature difference and heat capacity. The heat exchange between the subsurface and surface can be computed explicitly with an integrated model like HGS. In non-integrated models, important assumptions are made to simulate the process of heat exchange between surface and subsurface domains, which potentially increases the error and uncertainty in the results.

In addition, the resulting temperature depends on depth. For locations below the seasonal penetration depth of the land surface temperature signal, the simulated temperature takes

longer to be affected by the applied boundary condition compared to shallower locations. Therefore, for simulations without spin-up, the temperatures at greater depths remain similar, for longer times, to the initial temperatures assigned to the model.

Simulations show that initial state of the model affects the time it takes to reach equilibrium. For the scenarios tested here, it took longer to reach equilibrium with colder initial temperatures than with warmer initial conditions.

Comparison of observed and simulated temperatures at the field measuring stations show that, below the seasonal depth, the temperatures simulated by the models without spin-up remained similar to the initial temperature, regardless of the scenario. A similar result was shown in Figure 8 for observation point DeepP (which is below the seasonal depth). At depths below the seasonal depth, the effect of the applied geothermal flux is predominant. Temperatures remain similar to the initial values because the models without spin-up require time to adjust to the boundary conditions, including the bottom geothermal flux boundary, before they reach equilibrium. It took 9.9 years and 8.4 years for IC-5 and IC+5, respectively, to reach equilibrium, which demonstrates that spin-up is the best option to accurately reproduce the geothermal gradient in the shortest simulation time and eliminate the effect of initially assumed values.

Some simplifying assumptions were used in the simulation. Other than assumptions explained in Section 4.3.5, the simulations did not account for soil freeze-thaw cycles and the effect of latent heat. Therefore, the variability of hydraulic and thermal conductivities of units due to freezing and thawing processes was not considered.

5.5 Summary and conclusions

The effect of initial temperature on the thermal dynamics of a catchment with discontinuous permafrost was investigated with an integrated surface and subsurface hydrologic model. Four different scenarios for the initial temperature distribution were tested with respect to their impact on simulated subsurface temperatures and stored energy. In addition, recursive simulations were designed to evaluate the spin-up time and the persistence of the effect of initial temperatures. The difference in stored energy was used as an indication to evaluate when the equilibrium state was reached. The spin-up step in this study started from the initial temperature of -5°C, and took approximately 10 years to equilibrate.

Simulations show that the initial temperature conditions assigned to the subsurface domain can significantly influence the subsequent simulated temperatures. These trends are related to the thermal dynamics between the surface and subsurface domains, which depends on their temperature difference. Simulations further show that the effect of initial temperatures decreases for longer simulation times. Therefore, if the model is run long enough until it reaches equilibrium (in this study the model was run for 10 years), the effect of the initially assumed temperatures eventually fades. Therefore, models initiated with equilibrium temperatures will provide results that are more representative.

In addition, the study investigated the effect of the initial temperature on the variation of simulated temperatures with depth. The main difference between simulated temperatures for the scenarios tested appeared at elevations below the seasonal depths. In the models without spin-up, the simulated temperatures below the seasonal depth remained at the initially assumed values.

6 A 3D integrated water flow and heat transfer model for the Tasiapik Valley catchment in Umiujaq, Nunavik, Canada

The rate of permafrost degradation in Nunavik has increased significantly over the last two decades due to climate warming (Fortier and Aube-Maurice, 2008). The effect of climate change on the subsurface thermal regime in the Tasiapik Valley has been previously simulated with a 1D model (Buteau et al., 2004) and a 2D vertical model (Dagenais et al., 2020). In this study, a 3D integrated water flow and heat transport model has been developed to further investigate the thermal regime in the northern catchment of Umiujaq.

The land-surface temperature represents an important boundary condition when modelling the thermal budget of the shallow subsurface because it affects heat exchange between the surface and subsurface domains (Haynes et al., 2018 and Luo et al., 2018). Most modelling studies involving heat transfer use the spatially-averaged surface temperature. In this study, different methods to obtain the land-surface temperature are investigated and compared.

6.1 Methods and materials

6.1.1 Study area

The study area is a 2 km^2 catchment located in a valley near the village of Umiujaq in northern Quebec, Canada, in the discontinuous permafrost zone (Figure 6.1). Detailed geological and hydrogeological field investigations have been ongoing since 2013 to investigate permafrost degradation due to climate warming. Six hydrostratigraphic units have been identified in the valley (Figure 6.2). The bedrock is covered by a till layer, which consists of coarse-grained glacial and glaciofluvial sediments. The till layer is in turn overlain by a thick coarse-grained glaciofluvial deposit (sandy gravel unit), which lies below a frost-susceptible silty marine unit. Finally, a thin sandy layer covers most of the upstream part of the catchment.

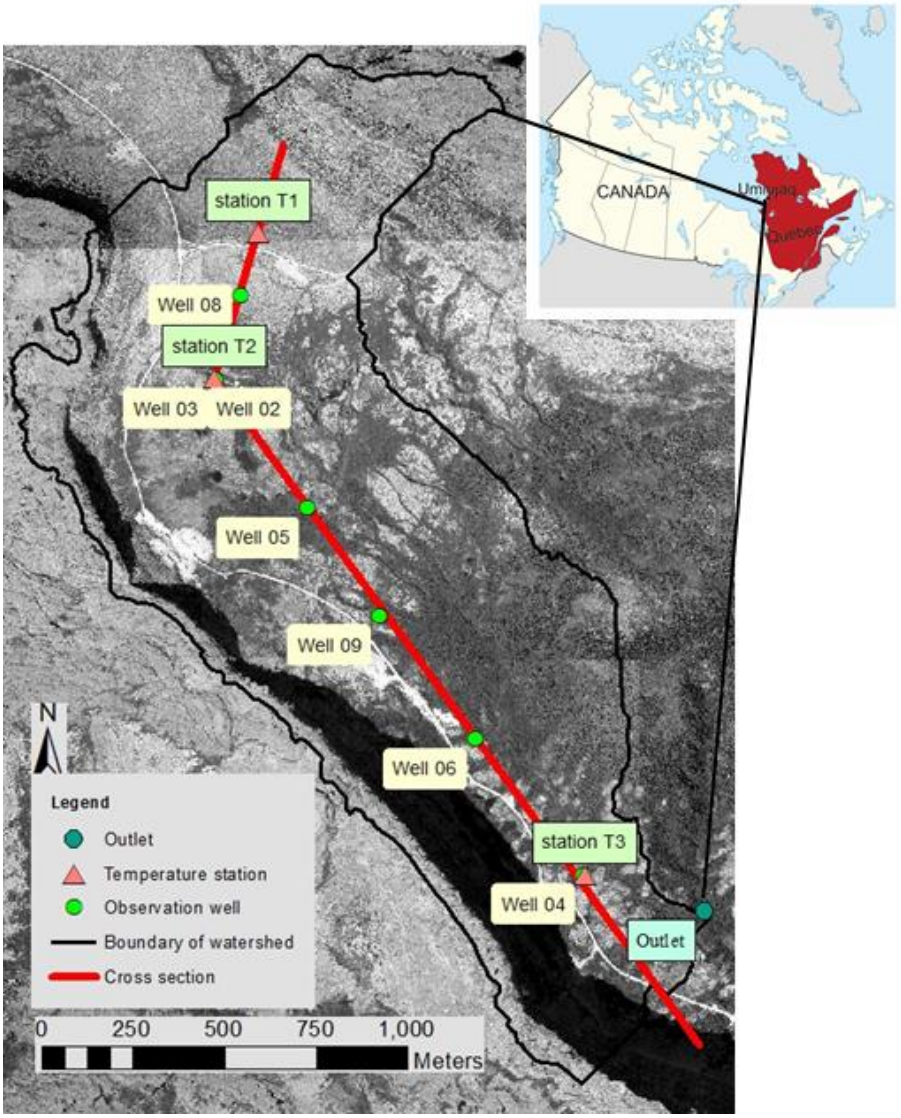

Figure 6.1 The Study area is located in a valley close to the village of Umiujaq. Seven observation wells along with 3 temperature stations and a gauging station to measure the discharge at the outlet provide the observation data for the field studies. Wells 2 and 3 are close together. The red line shows the cross-section of Figure 6.2.

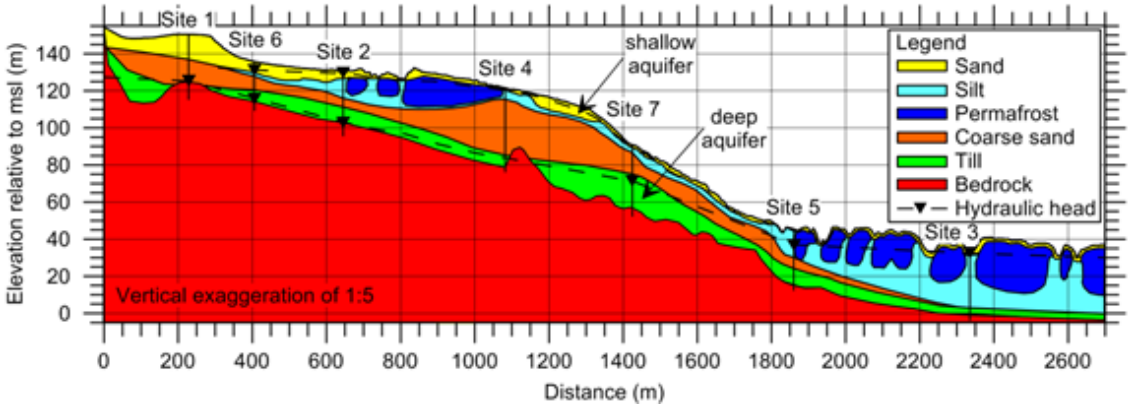

Figure 6.2 The study area consists of 6 distinct hydrostratigraphic units. Refer to Figure 6.1 for the location of the cross-section (Modified from Lemieux et al. 2016).

A steep slope connects the relatively flat upstream and downstream parts of the valley, resulting in an elevation difference of 100 m between the two plateaus. (Figure 6.1). The frost-susceptible silty marine layer is embedded with discontinuous permafrost, which is predominantly located in the thicker part of the silt layer at the downstream side of the catchment.

Table 6.1 lists the thermal and hydraulic properties of each layer. Thermal properties such as thermal conductivities and specific heat capacity were measured in the field (Buteau, 2002). Hydraulic conductivity and specific storage were calibrated according to the method described in Chapter 4. Unsaturated properties were calculated from the grain size distribution, using the Rosetta Software. In the numerical simulations carried out with HydroGeoSphere, the temperature is assumed to have an impact on both fluid density and viscosity (Aquanty, 2017). However, the simulations did not account for soil freeze-thaw cycles and the effect of latent heat.

Three temperature stations located in the valley have been used to measure vertical temperature profiles from ground surface down to 35 m in depth. In addition, land surface temperature was measured with 38 probes installed at a depth of 10 cm and distributed throughout the catchment (Figure 6.3).

Table 6.1 Hydraulic and thermal properties of the hydrostratigraphic units

	Hydraulic properties			Unsaturated van Genuchten properties			Physical and Thermal properties	
	K[1] (m/s)[a]	S_s[2] (1/m)[a]	θ_s[3,c]	α[b]	β[b]	K_T[4] (J/m/s/°C)[c,d]	c_s[5](J/kg/°C)[d]	ρ_b[6](kg/m^3)[e]
Sand	1.74E-4	1E-4	0.3	3.7	3.6	2	2480	1690
Silt	1E-6	2E-3	0.4	1.6	1.4	1.9	2550	2100[c]
Sandy gravel	1.08E-5	1E-4	0.35	3.7	3.6	2	2480	1690
Gravel	1E-5	1E-4	0.25	3.6	4.1	2	1764	1912
Rock	2.7E-10	1E-6	0.002	1.6	1.4	2.28	1340	2800
Permafrost	6.74E-8	-	0.002	1.6	1.4	2.6	1980	1600[c]

[1] Hydraulic conductivity; represents the unfrozen, saturated value
[2] Specific storage
[3] Porosity
[4] Thermal conductivity
[5] Specific heat
[6] Bulk density; representing bulk values of the porous medium under saturated conditions
[a] Calibration
[b] Rosetta Software, based on grain distribution
[c] (Buteau, 2002)
[d] (Dagenais *et al.*, 2020)
[e] (Leblanc, 2013)

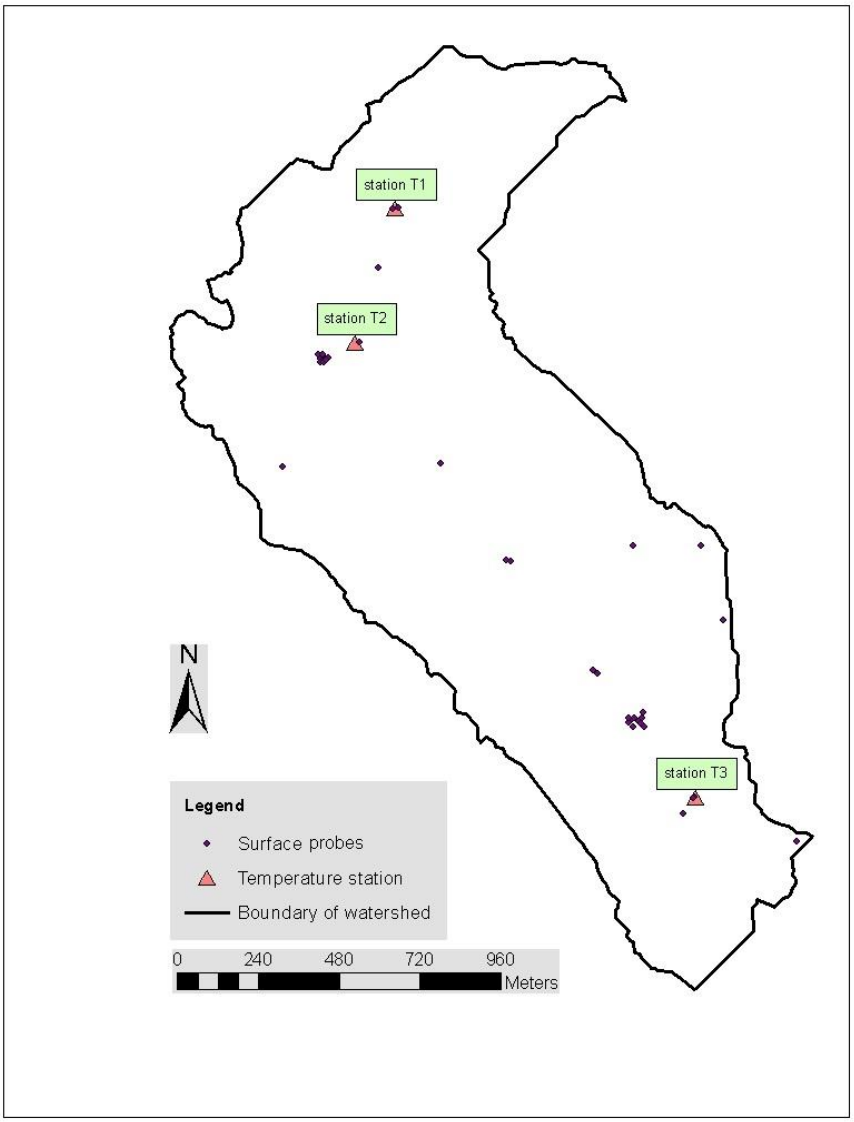

Figure 6.3 Location of installed probes to measure soil temperature in the catchment

The climate in Umiujaq is subarctic with cool and damp summers, and relatively dry and cold winters. Hudson Bay has a major influence on regional climate due to the strong winds in winter when the bay is frozen and due to the dense fog in summer. Figure 6.4 shows measured precipitation and air temperature at a weather station located in the catchment, for the period 2012-10-01 to 2015-07-10. The mean annual air temperature for this period was -6 °C and the minimum and maximum monthly temperatures were -36 °C and 23 °C, respectively. Precipitation was measured with a Geonor-T200 instrument and the data were processed according to the method described in Chapter 2. The mean annual precipitation between 2012 and 2015, including rain and snow, was 760 mm. Evapotranspiration was

calculated manually and subtracted from the precipitation time series to obtain the net precipitation. Then, the daily net precipitation was applied to the surface flow domain as a top flux boundary condition.

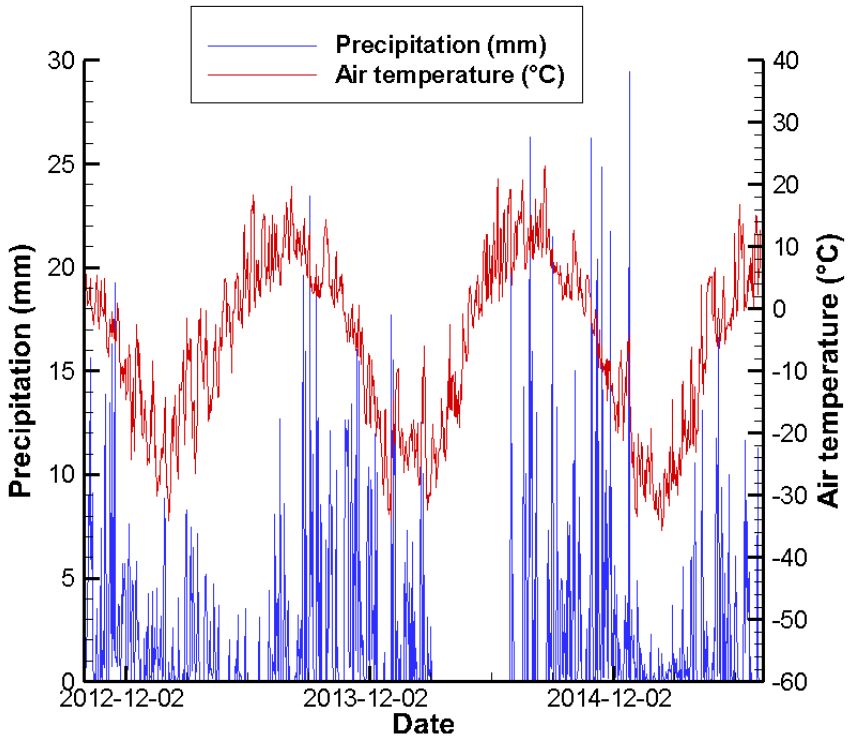

Figure 6.4 Observed precipitation and air temperature in the study area from 2012-10-01until 2015-07-10.

6.1.2 Numerical modelling

Three-dimensional surface water and groundwater flow, coupled with heat transport, was simulated with the HydroGeoSphere (HGS) code (Therrien *et al.*, 2010). The main feature of HGS is its ability to integrate 2D surface flow and transport equations with the 3D variably saturated subsurface equations. The model considers key components of the hydrologic cycle, for example, surface run-off, surface/subsurface coupled water flow, infiltration, and evaporation.

6.1.3 Governing equations

The governing flow equations are fully described in Chapter 5. The equation for variably-saturated subsurface heat transport is given by (Therrien *et al.*, 2010):

$$\frac{[(\partial c_b T)]}{\partial t} = -\nabla[q\rho_\omega c_\omega T - (k_{Tb} + \theta_s S_w c_w \rho_w D)\nabla T] \pm Q_T + \Omega_o \quad (6\text{-}1)$$

where ρ is density, c is the heat capacity, T is the bulk temperature of the subsurface (assuming local thermal equilibrium), t is time, q is the Darcy flux in the subsurface, $\mathbf{k_T}$ is the thermal conductivity, D is the hydrodynamic dispersion term, θ_s is porosity, S_w is water saturation, Q_T is a thermal source/sink and Ω_o is the thermal surface/subsurface interaction term. The subscript b denotes a bulk term, whereas w represents the aqueous phase.

Heat transport in the surface water is represented by the following equation:

$$\frac{\partial \rho_w c_w d_o T_o}{\partial t} = -\nabla\left[q_o \rho_w c_w T_o - \left(k_w + D_o \rho_w c_w\right) d_o \nabla T_o\right] + E_{atm} \pm Q_{To} - d_o \Omega_o \quad (6\text{-}2)$$

where d is the depth of the surface water, E_{atm} represents the atmospheric inputs to the surface thermal energy system, and the subscript o denotes overland flow.

The model does not account for freeze-thaw cycles and the effect of latent heat, at this stage. Therefore, the variability of hydraulic and thermal conductivities of units due to freezing and thawing processes is not considered

6.1.4 Heat transport simulations

The effect of initial temperature on the thermal regime in the Tasiapik valley near Umiujaq was explained in Chapter 5. This chapter studies the effects of two other factors: the land-surface boundary condition, and the unsaturated zone. The effect of initial temperature on heat transport simulations was investigated in Chapter 5. Results from the spin-up model of Chapter 5 (i.e., scenario ICSpin) are used as the initial condition for the simulations presented here.

Three different strategies are used here to assign land-surface temperature: 1) air temperatures and N-factors (the ratio of the ground surface freezing index to the air freezing index (Lunardini, 1978)), 2) average measured land-surface temperature, and 3) spatially-variable temperatures. The effect of considering the unsaturated zone on the thermal regime of a shallow hydrogeological system is also studied. A fully saturated model of the Umiujaq catchment was developed and compared to an otherwise equivalent variably-saturated model. The effect of a climate change -induced temperature rise on the thermal regime of the subsurface is also studied for Umiujaq.

6.1.4.1 Initial conditions

The result of the spin-up simulation (ie., the ICSpin model in Chapter 6) was used as the initial condition for the heat transport simulations in this chapter. In the spin-up simulation, the coupled water flow and heat transport model was run with average precipitation and temperature values until reaching its equilibrium state, at which point the change in model variables, such as energy storage, was minimal.. At the end of the spin-up, the temperature of the permafrost blocks, corresponding to the average measured temperature, was set to -2.5 °C (Buteau, 2002).

6.1.4.2 Boundary conditions

The flow boundary conditions are similar to those described in Chapter 5. For heat transport, the lateral subsurface boundaries were assigned a zero temperature gradient, which neglects horizontal conductive heat transfer. Along the bottom boundary, a geothermal flux of 0.032 W/m^2 was applied (Buteau, 2002). The land surface temperature was assigned to nodes of the surface domain. Through the dual-node approach used in HGS, heat energy can naturally be transferred between the surface domain and the subsurface porous medium.

In this study, three different scenarios were used to assign the land surface temperature: 1) The AirTemp model scenario uses measured air-temperature and N-factors, 2) The AveSTemp scenario applies the average temperature measured by surface probes across the entire model surface, and 3) The DistSTemp scenario includes the spatial distribution of land surface temperature, measured by the surface probes. The three land-surface time series, demonstrated in Figure 6.5, were then used to develop three coupled heat transfer models. The spin-up initialization explained in Chapter 5 was applied to all three scenarios.

Measured vertical temperature profiles at temperature stations T1, T2, and T3 were used to validate the three scenarios (Figure 6.3).

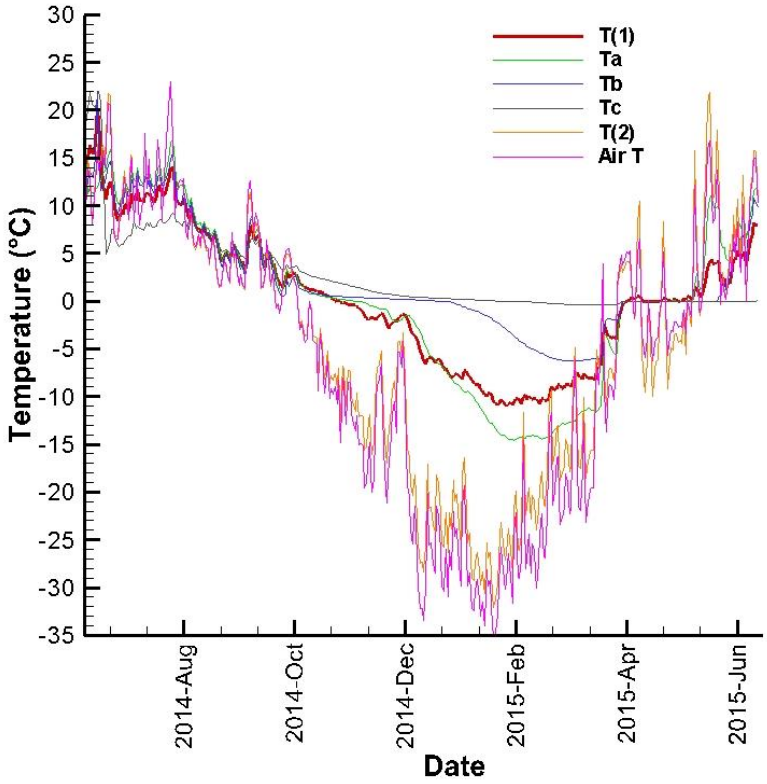

Figure 6.5 Temperature data used in the study. Average surface temperature obtained from temperature probes (T(1)), average surface temperature obtained from air temperature using N factor (T(2)) and three surface probes were used in model scenarios 1, 2 and 3, respectively.

For model scenario AirTemp, the averaged time series of the surface temperature derived from air temperatures was used as the boundary condition for the surface layer. Several factors cause the surface temperature to be different from air temperature, including net radiation, vegetation, snow cover, ground thermal properties, surface relief and sub-surface drainage (Andersland and Ladanyi, 2004). To obtain the land-surface temperature from air temperature, the N-factor approach was used, which is the ratio of the ground surface freezing index to the air freezing index (Lunardini, 1978). Monthly N-factors empirically determined by Buteau, 2002 were used here (Figure 6.6). Snow cover in winter and dry

vegetation cover in late summer act as insulators, which results in heat loss and an N-factor lower than 1. During the wet season (May to July), the thawing of snow cover, the lower albedo and the increased amount of surface water induce more heat accumulation from air temperature and solar radiation, which results in an N-factor higher than 1. The N-factors shown in Figure 6.6 were multiplied by the average air temperature to obtain the average land surface temperature (Average Surface T(2)) used in model scenario AirTemp (Figure 6.5).

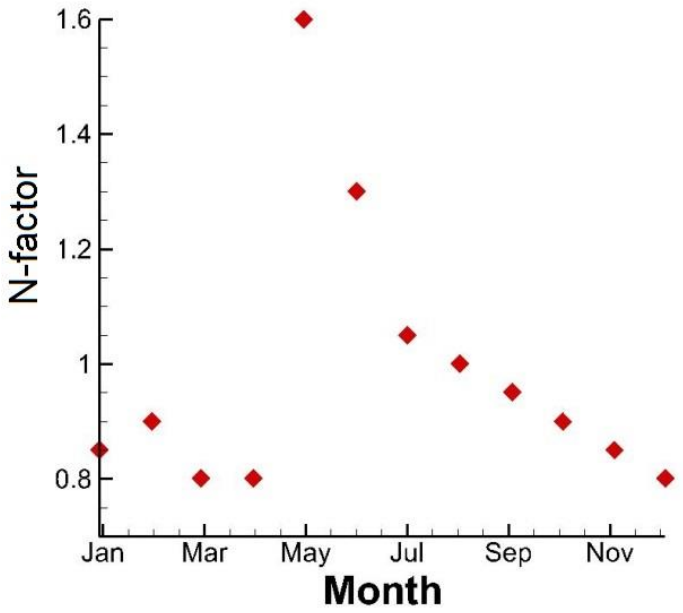

Figure 6.6 N-factors used for Umiujaq (Buteau, 2002)

For model AveSTemp, the temperature time series measured by the surface probes (Figure 6.3) were averaged and applied as the boundary condition to the surface layer (Average Surface T(1) in Figure 6.5). Model scenario AveSTemp will be used for methodologies explained in sections 6.2.3.3.

To investigate the effect of the difference between average land-surface temperature and the actual land-surface temperature, three individual surface probes were chosen for model scenario DistSTemp. These surface probes, named Ta, Tb, Tc, were chosen because they are the closest to the stations T1, T2 and T3, respectively. Figure 6.5 compares the temperature measured by each probe to the average land-surface temperature, for the simulation period (from July 2014 to July 2015). During the warm season (until October), the

difference between the temperature time series is not significant. However, during the cold season, when there is a snow cover, the temperature time series become distinctly different. The insulating effect of snow and the latent heat of soil moisture influence the surface temperature. This causes an offset between the actual surface temperature at each location and the average temperature. The temperature time series at each given probe was applied to ground surface and the simulated temperature profile was compared to the observed temperature profile at the corresponding temperature station.

6.1.4.3 The effect of the unsaturated zone

The model was run in the fully saturated mode to compare with the variably-saturated flow model. The model was passed through the two-step spin-up and then run for a one-year period from July 2014 to July 2015. The average surface temperatures measured by surface probes (similar to model AveSTemp in Section 6.2.3.2) were used as the land surface boundary condition.

6.1.4.4 The effect of increasing temperatures

Climate change scenarios for the Nunavik-Nunatsiavut IRIS region, downscaled from Global Climate Models (GCMs), predict a temperature rise of around 3°C in Umiujaq by 2050 (Brown et al., 2012, Dagenais et al., 2020). In this study, an average temperature rise of 0.09 °C/yr is applied to the ground surface temperature as a boundary condition for the subsurface simulations. The model was run from the initial condition in 2016 until 2050. Precipitation is assumed similar to that for the period of 2016 to 2017.

Some simplifying assumptions were used in the simulation. In addition to the assumptions explained in section 4.3.5, the simulations did not account for soil freeze-thaw cycles and the effect of latent heat. Therefore, variability of hydraulic and thermal conductivities of units due to transient freezing and thawing processes was not considered. Instead, the permafrost blocks were assigned a lower hydraulic K that did not change in time.

6.2 Results and discussion

6.2.1 The effect of the surface boundary condition

Comparison of the simulated temperature profiles (Figure 6.7) shows that using a globally uniform value for the land-surface temperature in models AirTemp and AveSTemp (not considering a variable spatial distribution of temperature) resulted in simulated temperatures that differ more from those observed during cold seasons than warm seasons. During the warm season, as there is not a significant difference between applied surface values (Figure 6.5), the simulated temperature profiles were similar for the three models. During the cold season, using the land-surface temperature gives a closer fit to observed values than using the land-surface temperature derived from air temperature. Compared to using an average value for the whole catchment, results are improved when applying a spatially-variable distribution of surface temperature as the boundary condition. This is more important in the cold regions where snow covers the area for a long period throughout the year. This effect was seen down to a depth of 5 m, below which the variable land-surface temperature does not penetrate. Below this depth, the temperature profile is controlled by the geothermal flux and thermal properties of the geologic units. Therefore, at these depths the temperature profiles were similar in the three models. The study by Shojae Ghias et al. (2017) supports the idea that the presence of snow cover affects the thermal regime of permafrost-impacted soil, which can be captured by using spatially distributed land-surface temperature.

(a)

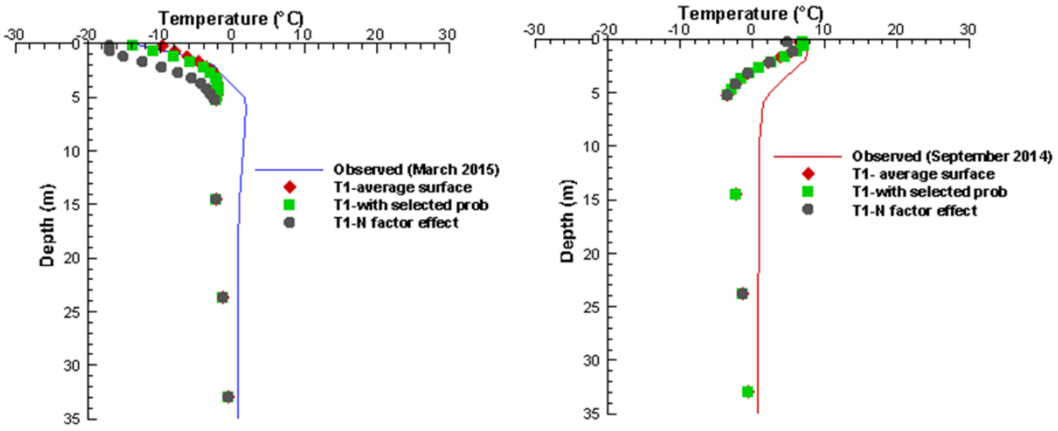

(b)

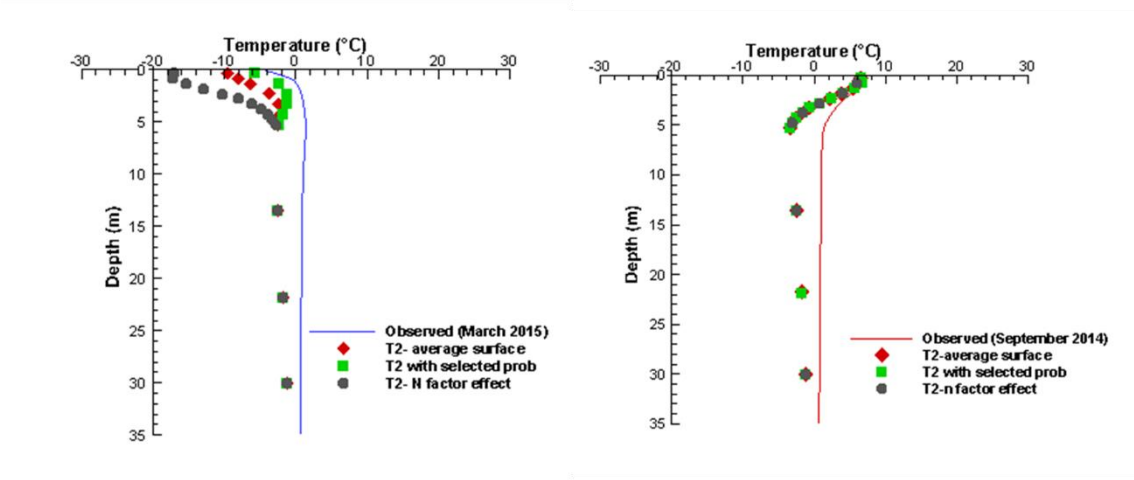

(c)

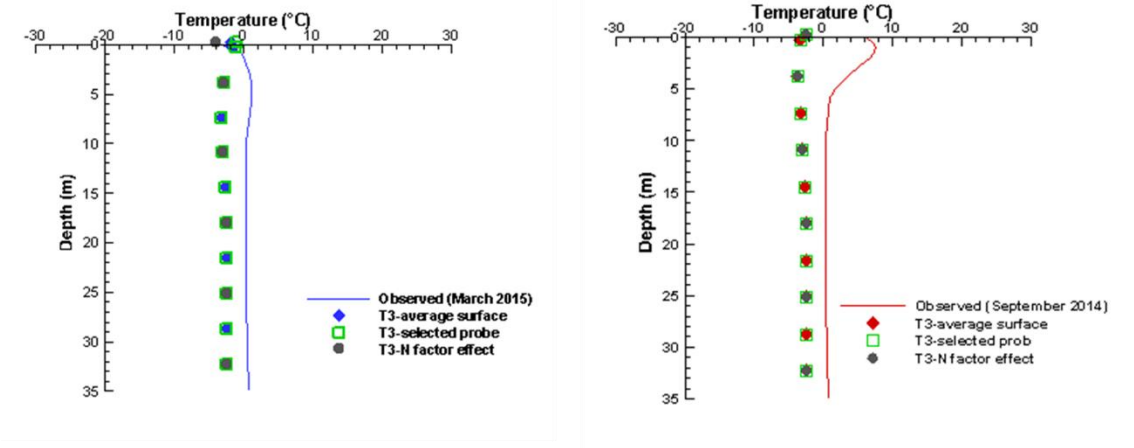

Figure 6.7 The effect of different surface boundary conditions on temperature profile at a) station T1 b) station T2, and c) station T2 in mid September and mid March as the result of applying the N-factor to air temperature (model AirTemp), average temperature measured by probes (model AveSTemp), temperature in the closest probe to the station (model DistSTemp).

Comparing the observed and simulated temperature profiles at the three stations (Figure 6.7) shows that the temperature profiles at station T3 are quite different compared to those at stations T1 and T2. For instance, comparing the near-surface temperatures in the profiles at stations T1 and T2 shows an offset between observed and simulated temperatures during the cold season, rather than during the warm season. The offset was higher in models AirTemp and AveSTemp than in model DistSTemp, which employs the temperature measured by the probes closest to the stations as the boundary condition. However, at

station T3, the offset between the observed and simulated temperatures near the surface occurred during the warm season rather than the cold season. Furthermore, there was no improvement in the results in the case of using the temperature at the probe closest to T3 (probe Tc) for modelling (Figure 6.7).

6.2.2 The effect of the unsaturated zone

To investigate the effect of saturation on the thermal regime, the transient model was run in fully-saturated and variably-saturated conditions. Simulated water saturation and temperature results are shown for the permafrost units near station T3 (Figure 6.8 to Figure 6.10). The results show the saturation and thermal regimes over four different seasons (extreme winter, spring, maximum summer and before the extreme winter). Comparing the saturation in Figure 6.8 and the thermal regime with the variably saturated model in Figure 6.9 show a lower temperature where the saturation is lower. For instance, results show that the temperature is higher at the bottom of units 2 and 3 compared to the temperature elsewhere in these units. By referring to Figure 6.8 demonstrating the saturation in these locations, it can be seen that the saturation is almost 1 at the bottom of units 2 and 3. That indicates the effect of a fully saturated layer below these units, which has a higher thermal conductivity compared to an unsaturated layer. Comparing the thermal regime in the variably saturated and fully saturated models in Figure 6.9 and Figure 6.10, respectively, shows that considering a fully saturated condition accelerates the temperature rise in the permafrost units due to the higher thermal conductivity of saturated materials. Therefore, the temperature is higher at the bottom of units 2 and 3.

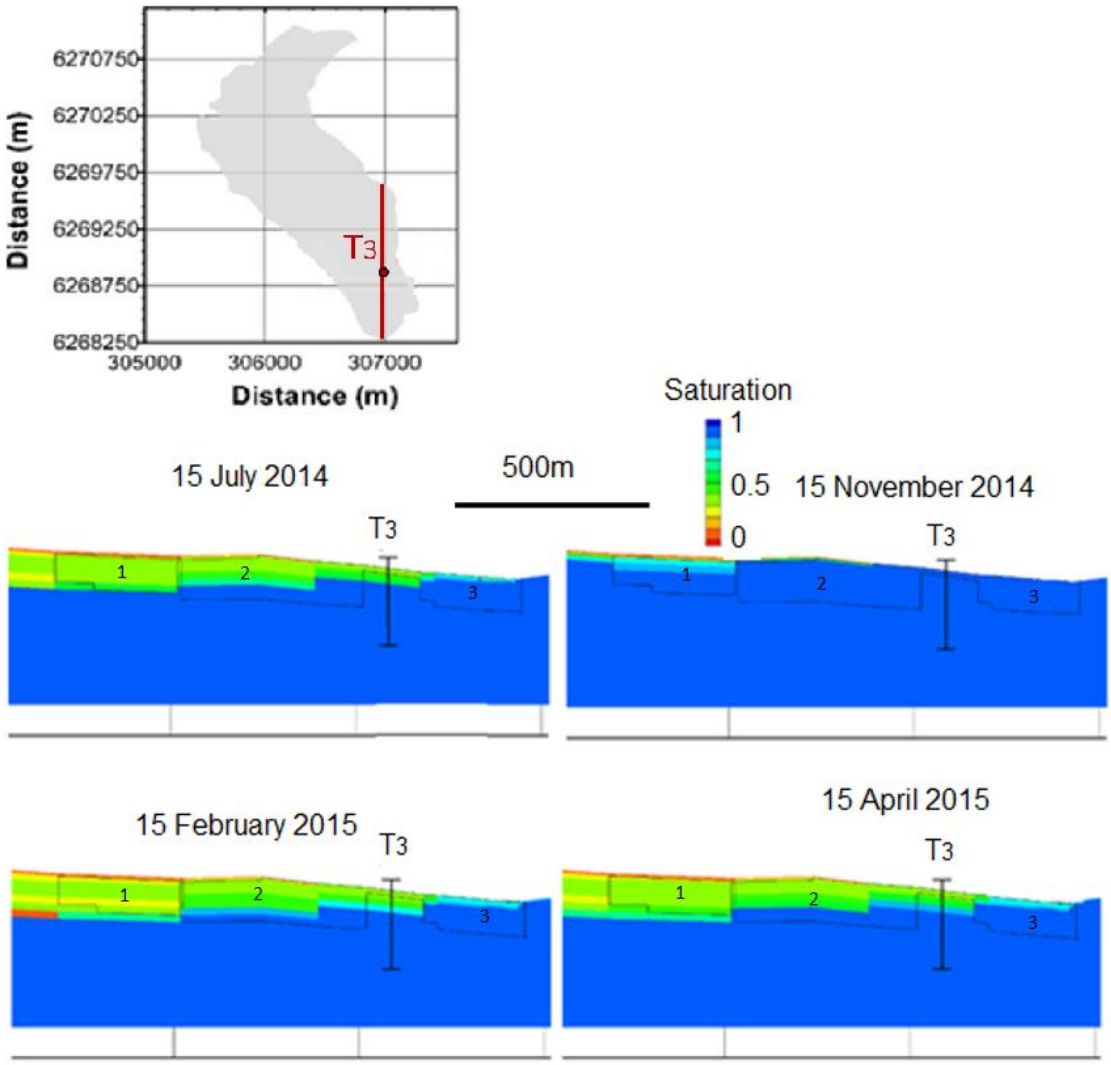

Figure 6.8 Simulated water saturation near station T3 in the variably-saturated model. The black outlines identify three permafrost units near station T3 (vertical exaggeration of 1:3, cross section: X=306990m).

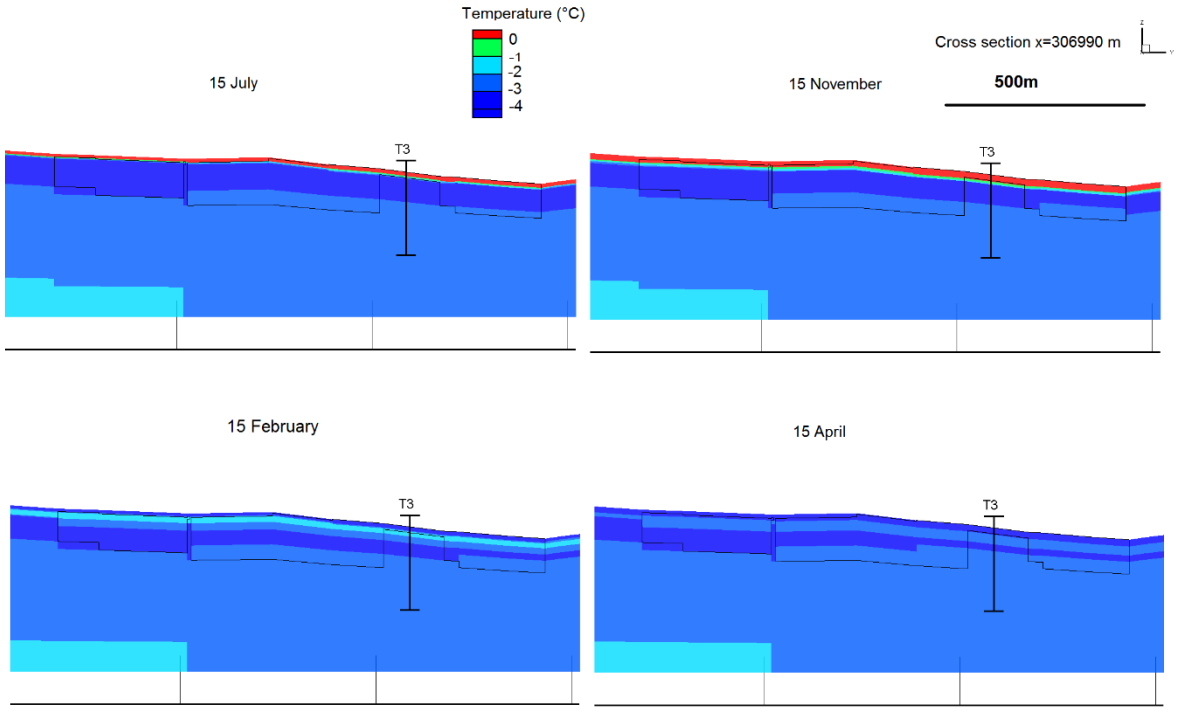

Figure 6.9 Simulated temperatures (°C) near station T3 in the variably-saturated model (vertical exaggeration of 1:3).

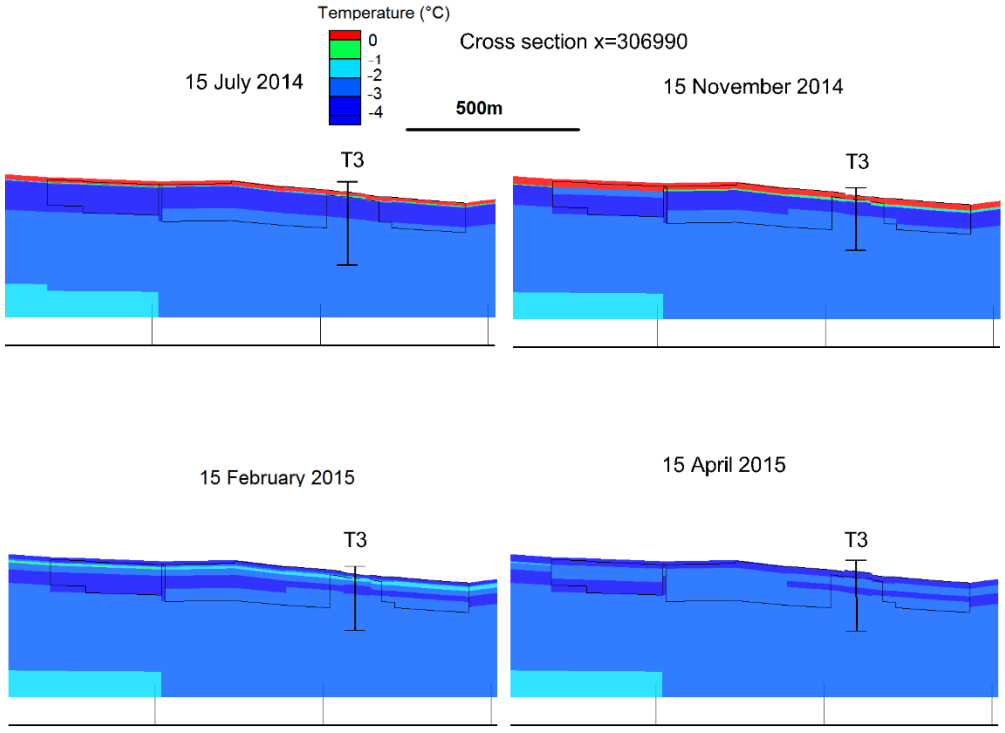

Figure 6.10 Simulated temperature (°C) near the station T3 in the fully-saturated model (vertical exaggeration of 1:3).

6.2.3 The effect of climate warming

A cross-section of the subsurface hydraulic and thermal conditions in July 2017 is shown in Figure 6.11. The transverse cross-section is very close to the outlet (Y=6268750m; see Fig 6.11a). The hydraulic heads decrease towards the outlet indicating flow direction towards the outlet. Following the flow paths with particle tracking in Figure 6.11d shows groundwater flow to the center of the cross-section, where the thin layer of till exists (Figure 6.11b). Simulated temperatures are higher at the left boundary of the model and decrease towards the outlet, indicating the cooling effect of the subsurface.

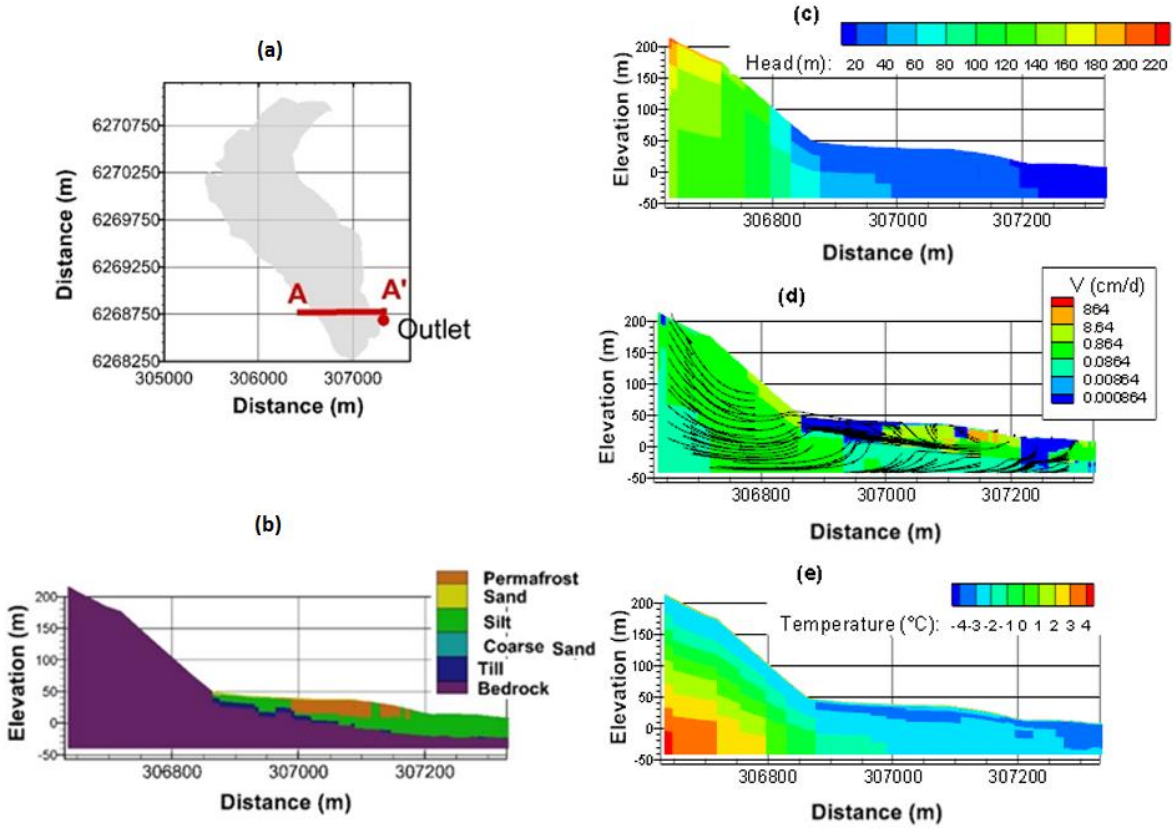

Figure 6.11 Simulated hydraulic and thermal conditions in July 2017 a) location of the AA' cross-section at Y=6268750 m, b) hydrostratigraphic units, c) hydraulic heads, d) velocity, e) temperature along the cross-section.

Figure 6.12 shows the predicted temperature change over 30 years, starting from current conditions in 2017, and applying the 0.09 °C/yr rate of increase. Simulations show that the temperature increases more at the center of the cross section, where flow paths are denser. As water moves towards the right side of the cross-section and eventually to the surface on the top right boundary, it cools down. Therefore, the temperature increase at the right boundary is less than at center. Field studies also suggests that in Umiujaq, groundwater reaching the discharge areas is significantly colder than in the recharge areas (as also shown at Umiujaq by Dagenais et al., 2020, and at Iqaluit by Shojae-Ghias et al., 2017).

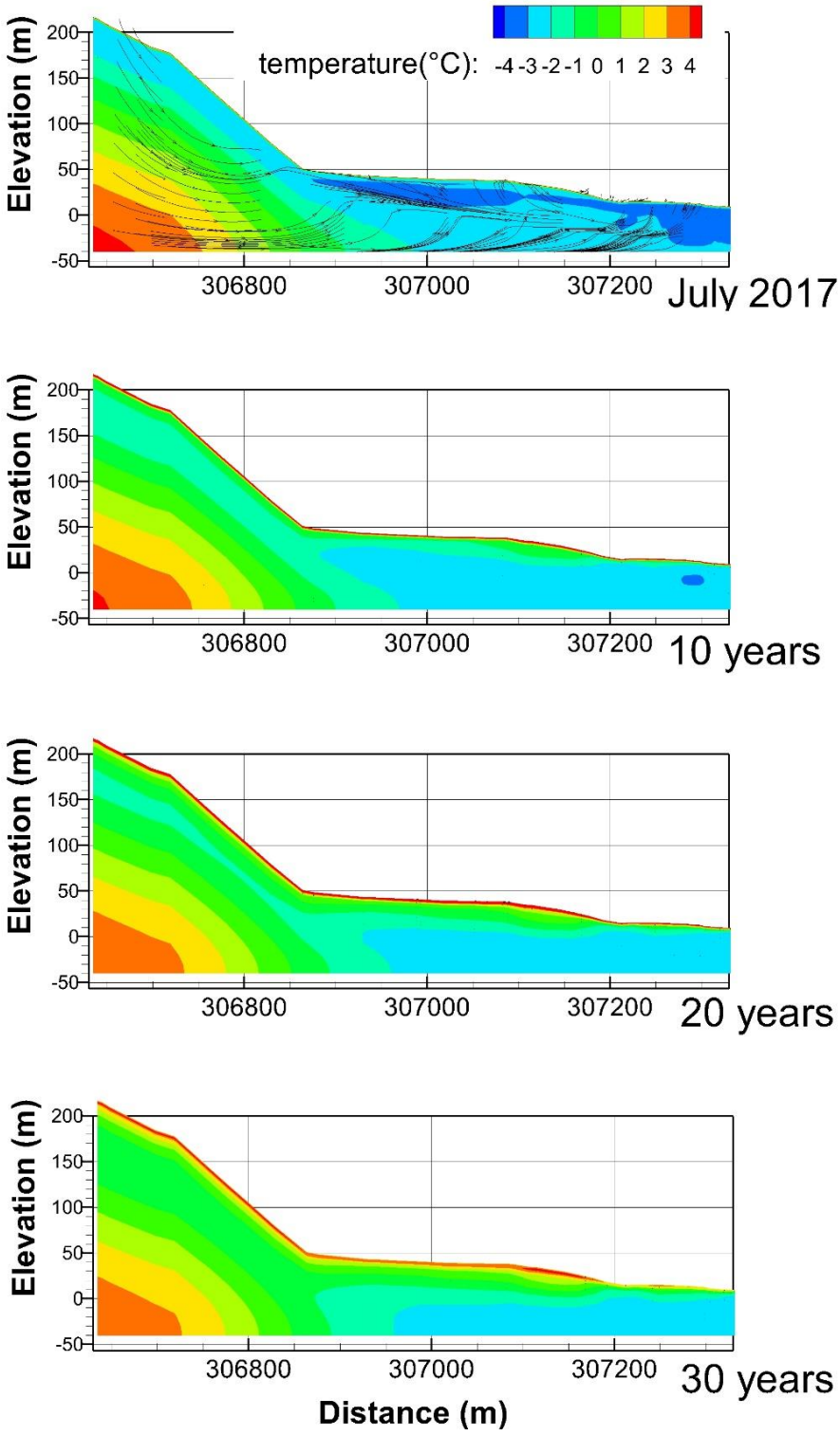

Figure 6.12 Predicted subsurface temperatures from 2017 to 2047 along section AA'. Since the model is 3D, some of the flow paths cross the section.

The predicted subsurface temperature field around the central permafrost unit for the climate-warming scenario is magnified in Figure 6.13. Over the 30–year simulation period, the temperature at the permafrost table increases from -3 °C in 2017 to approximately +1 °C in 2047, and from -3 °C to -1°C at the permafrost base. As a consequence, the rate of displacement of the thaw front is approximately 12 cm/yr at the permafrost table and 5.8 cm/yr at the permafrost base, in this location.

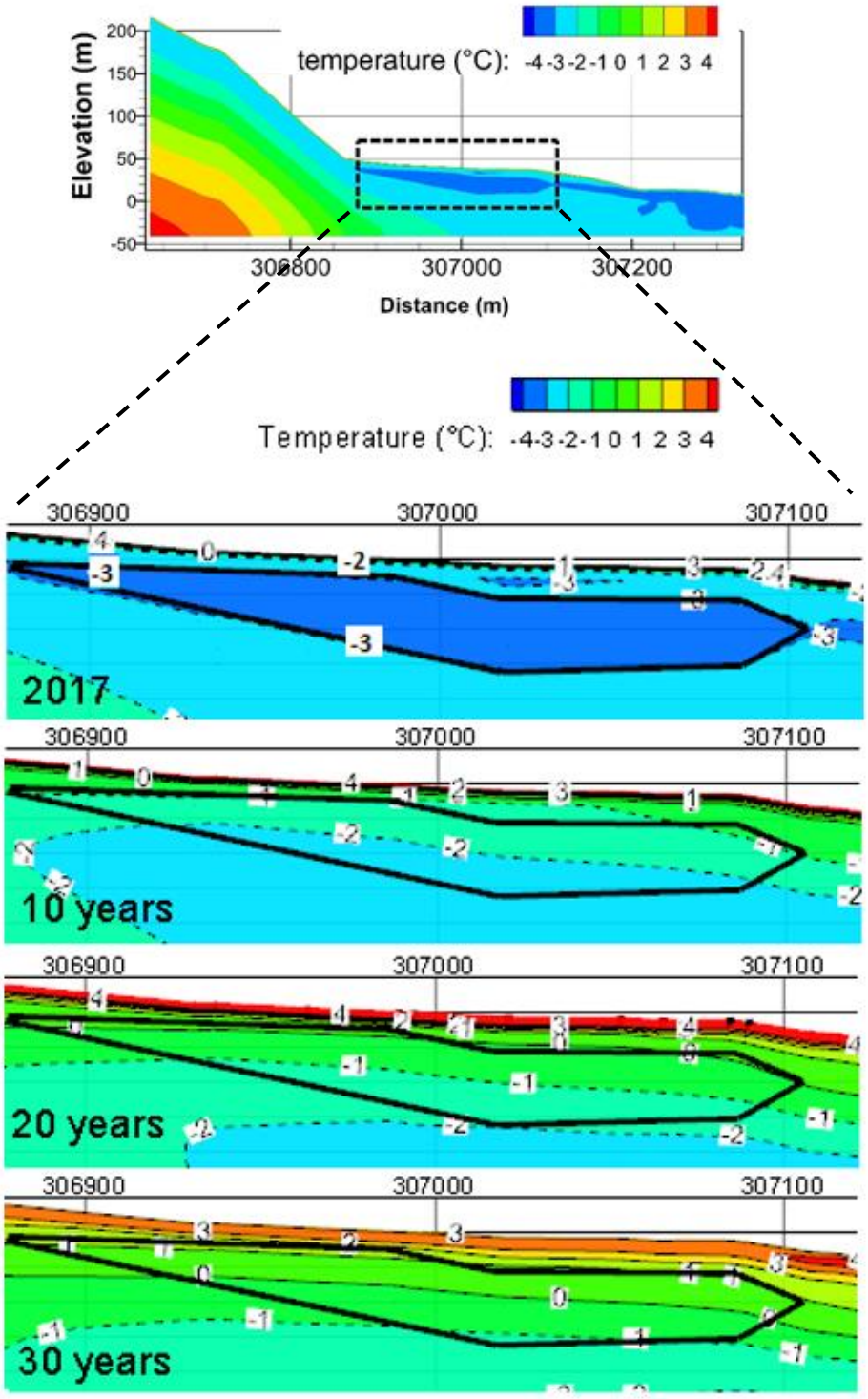

Figure 6.13 Predicted temperature distribution in July from 2017 to 2047 (magnified images). The original extent of permafrost is outlined in black.

Buteau et al. (2004) and Dagenais et al. (2020) predicted similar thaw rates at the surface of permafrost mounds upgradient of this cross-section, under similar climate scenarios, using 1D and 2D simulations, respectively. Although the predicted rate of temperature rise at the permafrost base in the 3D model is also similar to that of Buteau et al. (2004) (assuming conduction only), it was only comparable to the Scenario 2 simulation of Dagenais et al. (2020), which also only considered conductive heat transport. The more complete advective-conductive heat transport simulations of Dagenais et al (2020) predicted significantly higher thaw rates at the permafrost base. One reason for the different temperature rise in the 2D and 3D models can be due to the effect of flow perpendicular to the cross section, which has not been considered in the 2D model. As groundwater has a cooling effect in subsurface, the perpendicular flow can reduce the rate of temperature rise. At this cross-section location of the 3D model, conductive heat transport therefore appears more important than advective heat transport, which is supported by the relatively low groundwater flow velocities (mainly below 1E-6 m/s) as shown in Figure 6.11.

A longitudinal cross-section of the subsurface structure is shown in Figure 6.14, and subsurface temperatures in the cross section are shown in Figure 6.15. The figure shows that the temperature increases more rapidly at y=6268950 m to y=6269050 m and y=6269150 m to 6269250 m. The direction of flow at this cross section is mostly towards y=6269120 m, representing a discharge point in the cross-section (Figure 6.16). Similar to the transverse cross-section (Figure 6.12), the longitudinal cross-sections (Figure 6.15) show that the discharging groundwater flow has a cooling effect, reducing the rate of temperature increase below the discharge point.

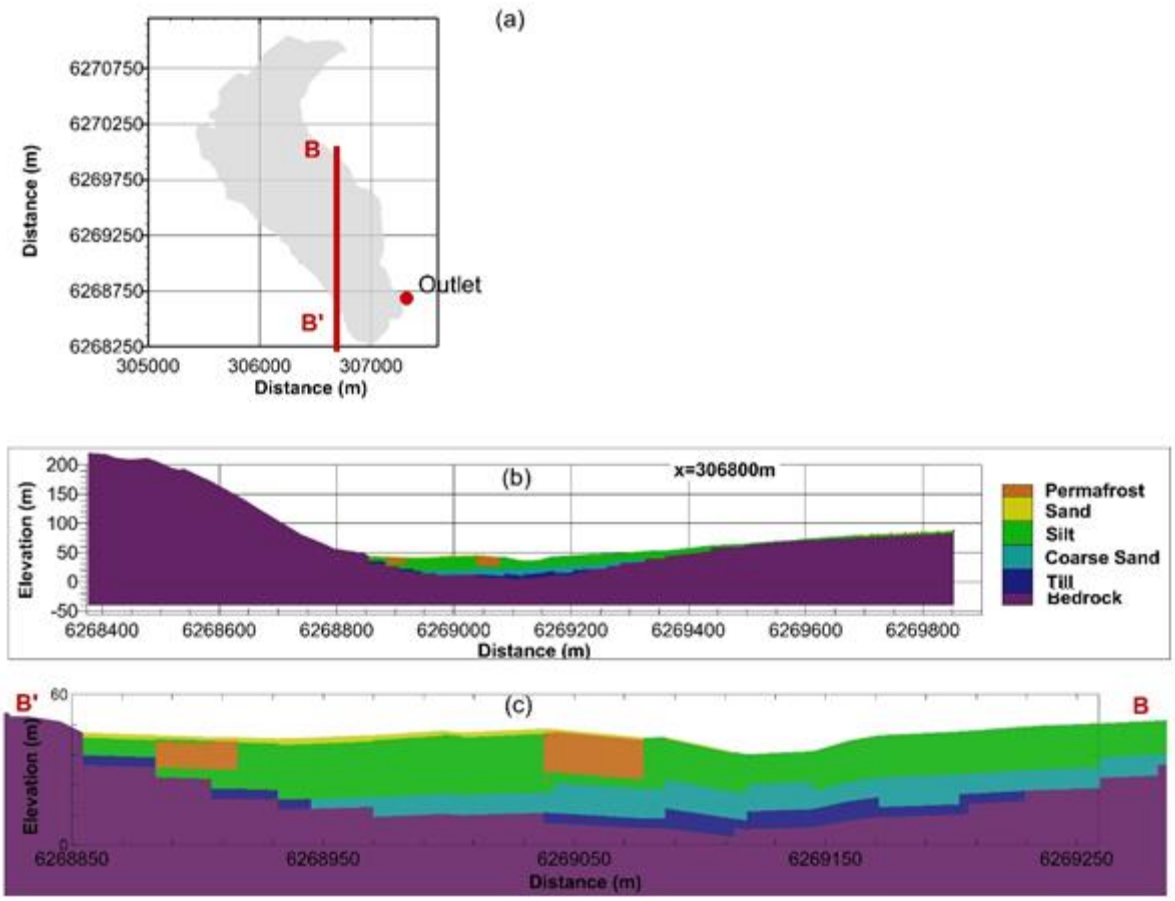

Figure 6.14 a) Location of the longitudinal cross-section (BB') at x=306800 m, b) subsurface structure c) detailed figure showing the cross-section between y=6268850 m and y=6269250 m

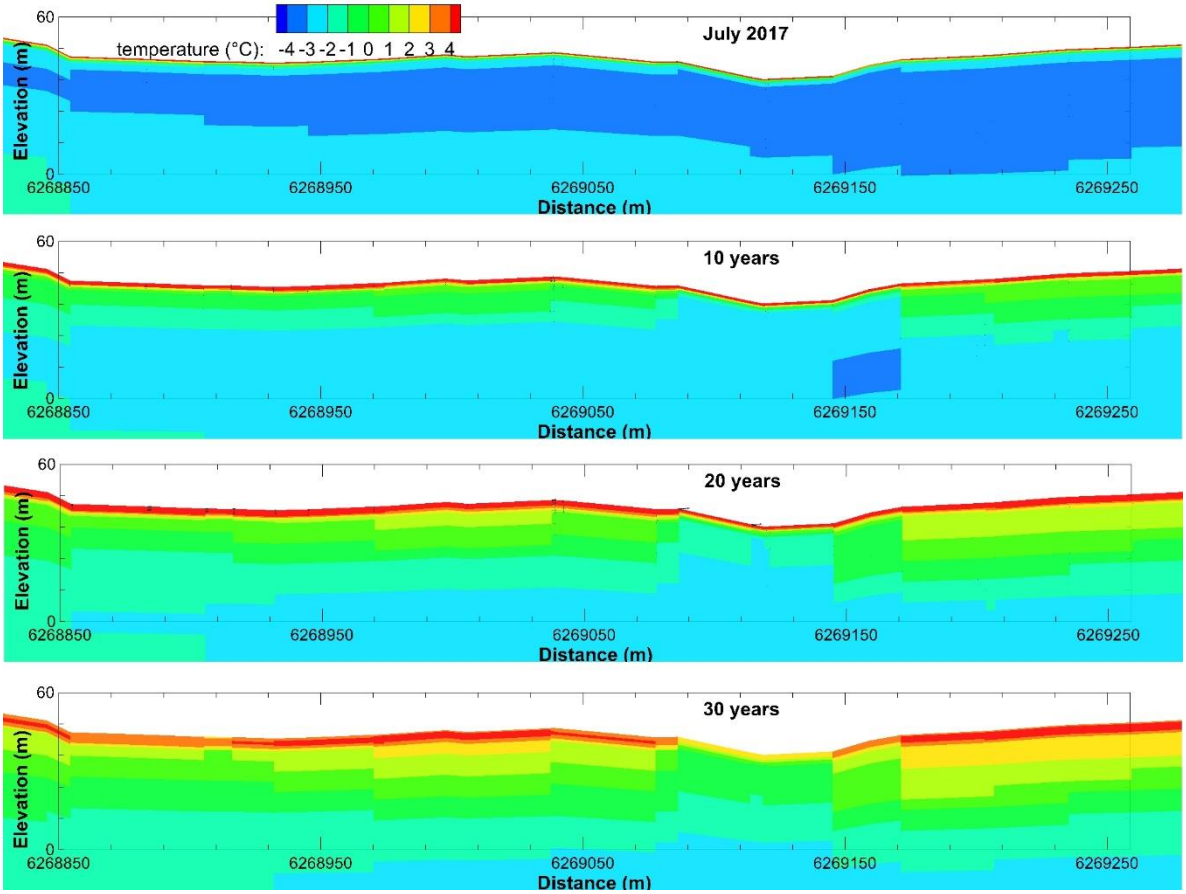

Figure 6.15 Predicted subsurface temperatures from 2017 to 2047 along section BB' and between y=6268850 m and y=6269250 m.

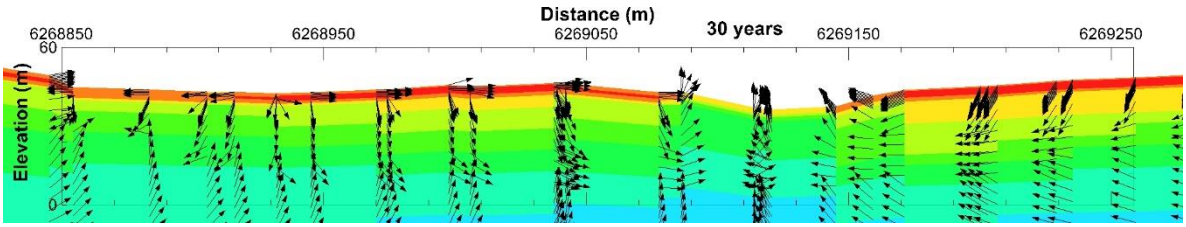

Figure 6.16 Velocity vectors for cross-section BB' after 30 years of simulation (2047). A uniform velocity vector length is used to better highlight the direction of flow.

The predicted effect of climate warming on the subsurface temperature increase at the three temperature stations is shown in Figure 6.17. Generally, temperatures increase at all depths over time. The rate of temperature increase near ground surface is higher compared to the deeper parts. The temperature profile at T1 is predicted to exceed zero at station T1, at all

depths, within 30 years. At both stations T2 and T3, the temperature is predicted to remain below zero below a depth of 15m, after 30 years.

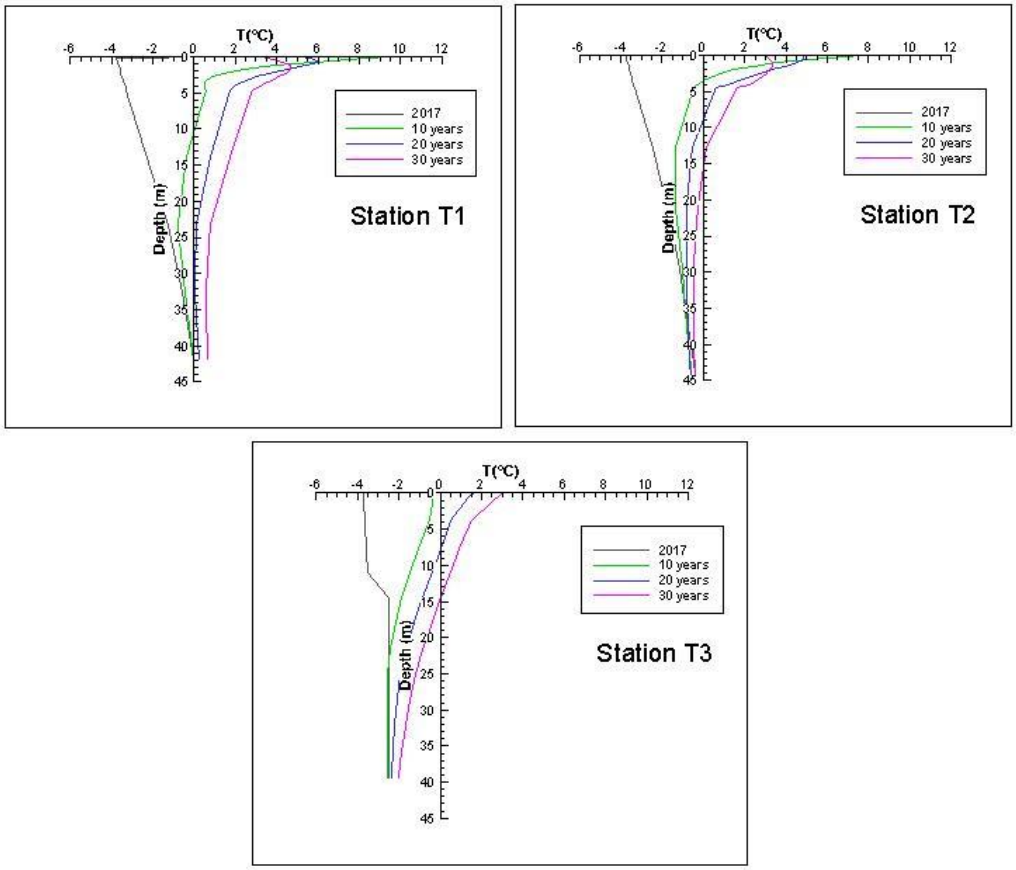

Figure 6.17 Effect of climate warming on the predicted subsurface temperature profiles, at the three temperature stations T1, T2 and T3.

It is acknowledged that this is a simplified simulation of the effect of climate warming on subsurface temperatures in a cold region. In particular, the freeze-thaw processes in discontinuous permafrost under climate warming, and therefore the effect of latent heat, is not considered in this simulation.

6.3 Conclusions

In this chapter, a coupled surface-subsurface water flow and heat transfer model was used to study the subsurface thermal regime in a northern catchment.

Different strategies were first applied to obtain the land surface temperature. Simulations showed that employing average land surface temperature as the boundary condition gives a good fit to observed subsurface temperatures during the warm season. However, in cold regions with snow, applying a uniform temperature to the whole catchment is not realistic. In these areas, using a spatially distributed land-surface temperature gives a better representation of the catchment.

The effect of saturation on the subsurface thermal regime was studied by running the simulation under fully saturated and variably saturated conditions. The fully saturated model overestimated the rate of subsurface temperature increase in the model, due to a higher thermal conductivity of the saturated layers.

The effect of climate change is studied by applying an annual temperature increase of 0.09°C to the imposed ground surface temperature. The 3D simulations showed that the groundwater temperatures in up-gradient and mid-gradient areas are higher than in down-gradient areas. In addition, the rate of temperature increase is higher in the up-gradient zones. The simulations showed that where groundwater flow is slow or absent at the base of permafrost, the rate of temperature increase at the permafrost table is higher (by a factor of approximately 2) than at the permafrost base. Simulations predict the temperature to increase at all three temperature stations in Umiujaq, leading to above-zero temperatures at all depths at station T1, after 30 years.

General conclusions and suggestions for future studies

The focus of this PhD project was to develop a 3D variably saturated model for the cold-region of the Tasiapik Valley catchment near Umiujaq, which embeds discontinuous permafrost units. The aim of the study was to better understand the hydrological and thermal regimes in this region, test conceptual models and study the effect of climate warming.

The simulations focused on:

- Sensitivity analysis of a coupled surface and subsurface water flow model of the catchment
- Calibration of the water flow model, using extensive field measurements
- Methodologies to obtain the initial conditions for a heat transport model at the catchment scale
- Application of the water flow and heat transport model to study the effect of climate warming on the subsurface thermal regime in Umiujaq

A conceptual model was first developed based on the observed surface and subsurface hydrogeological characteristics in the Tasiapik valley, Umiujaq, in northern Quebec, Canada. The numerical code HydroGeoSphere was then used to develop the 3D coupled model to simulate water flow and heat transport. A sensitivity analysis was completed to identify the effect of surface and subsurface parameters on the simulated hydraulic heads. Then, the model was calibrated to field-measured hydraulic heads using PEST, and was manually calibrated for the unsaturated characteristics to ensure that it was representative of the study area. Advective-conductive heat transport was then added to the water flow model. Different methods of obtaining the initial temperature conditions were investigated and compared. Finally, the model was used to simulate coupled water flow and heat transport processes in the study area.

The main outcomes of this PhD project are as follows:

Sensitivity analysis of a coupled surface and subsurface water flow model:

Sensitivity of hydraulic heads at different monitor points depends on the monitoring point locations in the study area. For example, hydraulic heads at the monitor wells that are located in the downstream part of the catchment, where surface water is present, were more sensitive to surface parameters. In contrast, hydraulic heads at wells that are located in the upstream part of the study area with no surface water flow were more sensitive to subsurface characteristics, such as hydraulic conductivity and specific storage.

Calibration of the water flow model in the heterogeneous system including discontinuous low-K permafrost blocks:

Using the defined hydrostratigraphic units in calibrating hydraulic heads and using the zoning method reduces the number of unknowns during calibration, which reduces the calibration time and respects the geologic field measurements and especially the permafrost units, which is important in studying groundwater flow systems in regions of discontinuous permafrost. However, this approach might not be efficient in highly heterogeneous areas, because it provides less freedom in the simulation to modify the parameters. Integrating this method with the pilot-point method would force the geologic field measurements to be considered, which should improve the fit to measured hydraulic heads.

Spin-up strategies in a water flow- heat transport simulation:

It is shown that the initial assumed temperature condition influences the subsequent simulated transient temperature field. Without applying a spin-up, the temperature - time series for models with a warmer initial condition show a tendency towards colder temperatures. The temperature - time series for the colder initial conditions have a tendency towards the warmer temperature. The thermal dynamics between the surface medium and the subsurface porous medium mainly depends on the temperature difference between the two media. Initial temperature conditions therefore influence the subsequent simulated temperatures. Results show that the effect of the initial conditions declines as the simulation time increases. Therefore, if the model is run long enough, the effect of the initially assumed temperature fades. The model initiated from an equilibrium temperature state gave more stable results.

Another indication of the importance of spin-up in heat transport models is the simulated temperatures at deeper depths. Simulated temperatures at greater depths are more significantly influenced by the applied geothermal flux than the surface temperature. A significant amount of simulation time is needed to observe the effect of the geothermal flux at mid-range depths of the model, away from the bottom boundary. Therefore, in the models without spin-up, the resulting temperatures below the seasonal depth remained at their initially assumed values. In the model with spin-up, the effect of the initially assumed temperature was eliminated at these depths.

Application of the water flow and heat transport model in a cold discontinuous permafrost environment:

Using the measured land-surface temperatures as a Type-1 surface boundary condition gives a better fit to observed temperature profiles compared to using surface temperatures obtained by applying N-factors to the air temperature. Furthermore, using a globally uniform value such as the land-surface temperature, while neglecting spatial variations, will result in a poorer fit to observed temperature profiles. The effect is more evident during the cold season, due to the insulating effect of snow cover and different snow thicknesses throughout the catchment. Therefore, applying a uniform surface temperature to the entire catchment is not realistic.

The effect of saturation on the subsurface thermal regime was studied by running the simulation under fully saturated and variably saturated conditions. The fully saturated model produced a more rapid temperature increase, due to the higher thermal conductivity of the saturated layers.

The effect of climate warming on subsurface temperatures was studied using the coupled water flow - heat transport model. In groundwater recharge areas, simulated temperatures increased more rapidly than in discharge areas.

In summary, using integrated models to simulate water flow and heat transport processes in cold regions should provide a more realistic representation of the physical system since more realistic hydrologic processes are included. Integrated models, for example, do not include as many assumptions and simplifications as in unintegrated models. Nevertheless, specific model characteristics including the initial temperature conditions can still have significant effects on the results. Including a spin-up step to obtain the initial conditions is

recommended to improve the fit to observed values. Calibrating integrated models, however, needs more computational time.

Future studies could consider further simulations to improve our understanding of the hydrogeological and thermal processes in cold catchments like Umiujaq. This work could include:

- Using a more focused study on the surface characteristics to better simulate surface water flow in summer and to improve the fit of simulated hydrographs.
- Using the pilot-points method with a transient model to better represent confining layers and perched aquifers, and to obtain a better fit to observed hydraulic heads and hydrograph.
- Include freeze-thaw processes of permafrost in coupled water flow and heat transport models
- Apply more detailed future climate scenarios to study the effect of future climate change on these types of cryo-hydrogeological systems.
- Calibrate the couple water flow-heat transport simulation against thermal variables.

References

Ajami, H., McCabe, MF., Evans, JP., and Stisen S.. 2014. Assessing the Impact of Model Spin-up on Surface Water-Groundwater Interactions Using an Integrated Hydrologic Model. Water Resources Research 50(3): 2636–56.

Albers BMC., Molson J., and Bense V., Parameter sensitivity analysis of a 2D cryo-hydrogeological numerical model of degrading permafrost near Umiujaq (Nunavik, Canada),Hydrogeology Journal, 2020.

Andersland, O., and Ladanyi, B. 2004. Frozen Ground Engineering. Chichester, UK: Wiley.

Bardsley, T., and Williams, MW. 1997. Overcollection of Solid Precipitation by a Standard Precipitation Gauge, Niwot Ridge, Colorado. In Western Snow Conf., Banff, AB, Canada, 354–62.

Barrère, M., 2018. Évolution couplée de la neige, du pergélisol et de la végétation arctique et subarctique. Université Laval.

Bense, VF., Kooi, H., Ferguson, G., Read, T. 2012. Permafrost degradation as a control on hydrogeological regime shifts in a warming climate, Journal of Geophysical Research: Earth Surface, doi:10.1029/2011JF002143.

Bloomfield, J., Jackson, C., & Sturat, M. 2013. Changes in groundwater levels, temperature and quality in the UK over the 20th century: an assessment of evidence of impacts from climate change. UK: Living With Environmental Change Report.

Briggs, MA., Walvoord, MA., McKenzie, JM., Voss, CI., Day-Lewis, FD., Lane, JW. 2014. New permafrost is forming around shrinking Arctic lakes, but will it last?, Geophysical Research Letter, 1585-1592.

Buteau S, Fortier R, Delisle G, Allard M., 2004. Numerical simulation of the impacts of climate warming on a permafrost mound. Permafrost and Periglacial Processes, 15:41–57.

Buteau, S. 2002. Étude de l'affaiblissement du comportement mécanique du pergélisol dû au Réchauffement climatique. Université Laval

Chow, V.T.. 1959. Open-Channel Hydraulics. Blackburn Press.

Cochand, M., Molson J., Barth J.A-C., van Geldern R., Lemieux J-M., Fortier R., Therrien R., Rapid groundwater recharge dynamics determined from hydrogeochemical and isotope data in a small permafrost watershed near Umiujaq (Nunavik, Canada), Hydrogeology Journal, https://doi.org/10.1007/s10040-020-02109-x, 2020.

Dagenais, S. 2018. Coupled cryo-hydrogeological modelling of permafrost dynamics at Umiujaq, Quebec, Canada. Université Laval.

Dagenais, S., Molson, J., Lemieux, JM., Fortier, R. and Therrien, R. 2020. Coupled cryo-hydrogeological modelling of permafrost degradation near Umiujaq (Nunavik, Canada), https://doi.org/10.1007/s10040-020-02111-3, Topical collection “Hydrogeology of a cold region watershed near Umiujaq (Nunavik, Canada)” Hydrogeology Journal.

Dagenais, S., Molson, J., Lemieux, JM., Fortier, R., Therrien, R. 2017. Coupled Cryo-Hydrogeological Modelling of Permafrost Degradation at Umiujaq, Quebec Canada. In GeoOttawa 2017, 12th Joint CGS/IAH-CNC Groundwater Conference, Ottawa, Canada, Oct. 1-4, 2017.

Dobinski, W. 2011. Permafrost. Earth-science Reviews, 158-169.

Doherty, J. 2010. PEST: Model-Independent Parameter Estimation. 5th ed. Brisbane, Queensl., Australia: Watermark Numerical Computing.

Doherty, JE., Fienen, MN., and Hunt, RJ. 2010. Approaches to Highly Parameterized Inversion—A Guide to Using PEST for Groundwater-Model Calibration. U.S. Geological Survey Scientific Investigations Report: 59 p.

El-Zehairy, A. A., Lubczynski, M. W. and Gurwin, J. 2018. Interactions of Artificial Lakes with Groundwater Applying an Integrated MODFLOW Solution. Hydrogeology Journal: 109–32. http://link.springer.com/10.1007/s10040-017-1641-x.

Fortier, R., & Aubé-Maurice, B. 2008. Fast Permafrost Degradation Near Umiujaq in Nunavik (Canada) Since 1975 Assessed from Time-Lapse Aerial and Satellite Photographs. 9th International conference on Permafrost (pp. 457-462). Alaska, USA: Institute of Northern Engineering University of Alaska Fairbanks.

Fortier, R., Banville, D., Lévesque, R., Lemieux, JM., Molson, J., Therrien, R., and Ouellet, M. 2020. Development of a 3D cryo-hydrogeological model of a small watershed in a degrading permafrost environment near Umiujaq (Nunavik, Canada), Hydrogeology J.

Frei, S., Lischeid, G., and Fleckenstein, JH. 2010. Effects of Micro-Topography on Surface-Subsurface Exchange and Runoff Generation in a Virtual Riparian Wetland - A Modelling Study. Advances in Water Resources 33(11): 1388–1401. http://dx.doi.org/10.1016/j.advwatres.2010.07.006.

Goderniaux, P., Brouyere, S., Fowler, HJ. Blenkinsop, S., Therrien, R., Orban, F., Dassrgues, A.. 2009. Large Scale Surface-Subsurface Hydrological Model to Assess Climate Change Impacts on Groundwater Reserves. Journal of Hydrology 373(1–2): 122–38.

Goodison, B E, Louie, P. Y. T., and Yang, D. 1998. WMO solid precipitation measurement intercomparison. World Meteorol. Org., Geneva.

Google Maps, 2019. Umiujaq, 56°32′N 76°33′W, viewed 07 November 2011. <https://www.google.co.uk/maps/place/Umiujaq>.

Grenier, C., Anbergen, H., Bense, V., Chanzy, Q., Coon, E., Collier, N., Costard, F., Ferry, M., Frampton, A., Frederick, J., Holmen, J., Jost, A., Kokh, S., Kurylyk, B., McKenzie, J., Molson, J., Mouche, E., Orgogozo, L., Pannetier, R., Rivière, A., Roux, N., Rühaak, W., Scheidegger, J., Selroos, J.O., Therrien, R., Vidstrand, P., Voss, C. 2018. Groundwater flow and heat transport for systems undergoing freeze-thaw: Intercomparison of numerical simulators for 2D test cases, Advances in Water Resources, vol. 114, p196–218, https://doi.org/10.1016/j.advwatres.2018.02.001.

Haynes, MW., Horowitz, FG., Sambridge, M., Gerner, EdJ. Beardsmore, GR. 2018. Australian Mean Land-Surface Temperature. Geothermics 72(October 2017): 156–62. https://doi.org/10.1016/j.geothermics.2017.10.008.

Huo, AD., Dang, J., Song, J., Chen, XH., Mao, HR. 2016. Simulation Modelling for Water Governance in Basins Based on Surface Water and Groundwater. Agricultural Water Management 174: 22–29. http://dx.doi.org/10.1016/j.agwat.2016.02.027.

Hwang, HT., Park, YJ., Sudicky, EA., Berg, SJ., Mclaughlin, R., Jones, JP. 2018. “Understanding the Water Balance Paradox in the Athabasca River Basin, Canada.” Hydrological Processes 32(6): 729–46.

Ireson, AM., Van der Kamp, G., Ferguson, G., Nachshon, U., Wheater, HS. 2013. Hydrogeological processes in seasonally frozen northern latitudes: understanding, gaps and challenges, Hydrogeology Journal, 53-66.

IPCC. 2007. Climate Change 2007: Synthesis Report. IPCC Fourth Assessment Report. Intergovernmental Panel on Climate Change. Available from www.ipcc.ch/pdf/assessment-report/ar4/syr/ar4_- syr.pdf.

Jones, J. P., Sudicky, E. A., and McLaren, R. G. 2008. “Application of a Fully-Integrated Surface-Subsurface Flow Model at the Watershed-Scale: A Case Study.” Water Resources Research 44(3): 1–13.

Kurylyk, BL., MacQuarrie, KTB., McKenzie, JM. 2014a. Climate change impacts on groundwater and soil temperatures in cold and temperate regions: Implications, mathematical theory, and emerging simulation tools, Earth-Science Review, 313-334.

Kurylyk, BL., MacQuarrie, KTB., Voss, CI. 2014b. Climate change impacts on the temperature and magnitude of groundwater discharge from shallow, unconfined aquifers, Water Resources Research, 3253-3274.

Leblanc, A.M., Fortier, R., Cosma, C., & Allard, M. 2006. Tomographic imaging of permafrost using three-component seismic cone-penetration test. Geophysics, 55-65.

Leblanc, A.M. 2013. “Modélisation Tridimensionnelle Du Régime Thermique Du Pergélisol de La Vallée de Salluit Au Québec Nordique En Fonction de Différents Scénarios de Réchauffement Climatique.” Université Laval. http://www.theses.ulaval.ca/2013/29687/.

Lemieux, JM., Fortier, R., Murray, R., Dagenais, S., Cochand, M., Delottier, H., Therrien, R., Molson, J., Pryet, A., Parhizkar, M. 2019. Groundwater dynamics within a watershed in the discontinuous permafrost zone near Umiujaq (Nunavik, Canada), accepted June 6, 2019 (in press), Hydrogeology Journal, 2019.

Liggett, JE., Partington, D., Frei, S., Werner, AD., Simmons, CT., Fleckenstein, JH. 2015. An Exploration of Coupled Surface-Subsurface Solute Transport in a Fully Integrated Catchment Model. Journal of Hydrology 529: 969–79. http://dx.doi.org/10.1016/j.jhydrol.2015.09.006.

Lunardini, VJ. 1978. “Theory of N-Factors and Correlation of Data.” In 3rd International Conference on Permafrost, Edmonton, Alberta: National Research Council of Canada, 40–46.

Luo, D., Jin, J., Marchenko, SS., and Romanovsky, VE. 2018. Difference between Near-Surface Air, Land Surface and Ground Surface Temperatures and Their Influences on the Frozen Ground on the Qinghai-Tibet Plateau. Geoderma 312(October 2017): 74–85. https://doi.org/10.1016/j.geoderma.2017.09.037.

Maheswaran, R., Khosa, R., Gosain, AK., Lahari, S., Sinha, SK., Chahar, BR., Dhanya, CT. 2016. Regional Scale Groundwater Modelling Study for Ganga River Basin. Journal of Hydrology 541: 727–41. http://dx.doi.org/10.1016/j.jhydrol.2016.07.029.

McKenzie, JM., Voss, CI. 2013. Permafrost thaw in a nested groundwater-flow system, Hydrogeology Journal, 299-316.

Menberg, K., Blum, P., Kurylyk, BL., Payer, P. 2014. Observed groundwater temperature response to recent climate change, Hydrology and earth system sciences, 69-85.

Molson, J.W., Frind, E.O. and Palmer, C.D. 1992. Thermal energy storage in an unconfined aquifer 2.Model development, validation and application. Water Resources Research, Vol. 28, No. 10, pp. 2857-2867.

Molson, JW and Frind, EO., 1992. Thermal Energy Storage in an unconfined Aquifer 2. Model Development, validation, and Application. Water Resources Research, vol. 28, p 2857-2867.

Painter, SL. 2011. Three-phase numerical model of water migration in partially frozen geological media: model formulation, validation, and applications, Computational Geosciences, 69-85.

Painter, SL., Coon, ET., Atchley, AL., Berndt, M., Garimella, R., Moulton, JD., Svyatskiy, D., Wilson, CJ. 2016. Integrated surface/subsurface permafrost thermal hydrology: Model formulation and proof-of-concept simulations, Water Resources Research, 6062- 6077.

Pan, X., Yang, D., Li, Y., Barr, A., Helgason, W., Hayashi, M., Marsh, P., Pomeroy, J, Janowicz, RJ. 2016. Bias Corrections of Precipitation Measurements across Experimental Sites in Different Ecoclimatic Regions of Western Canada. The Cryosphere 10: 2347–60.

Park, Y. J., Sudicky, E. A., Brookfield, A. E., and Jones, J. P. 2011. Hydrologic Response of Catchments to Precipitation: Quantification of Mechanical Carriers and Origins of Water. Water Resources Research 47(12): 1–11.

Pertti, A. Rossi, PM., Isokangas, E., and Kløve, B.. 2015. Fully Integrated Surface-Subsurface Flow Modelling of Groundwater-Lake Interaction in an Esker Aquifer: Model Verification with Stable Isotopes and Airborne Thermal Imaging. Journal of Hydrology 522: 391–406.

Pertti, A., Soulsby, C., Wang, H., and Tetzlaff, D. 2017. Integrated Surface-Subsurface Model to Investigate the Role of Groundwater in Headwater Catchment Runoff Generation: A Minimalist Approach to Parameterisation. Journal of Hydrology 547: 664–77. http://dx.doi.org/10.1016/j.jhydrol.2017.02.023.

Rui, H., Liu, Q. and Xing, Y.. 2018. Case Study of Heat Transfer during Artificial Ground Freezing with Groundwater Flow. Water (Switzerland) 10(10).

Schilling, OS., Park, YJ., Therrien, R., and Nagare, RM. 2019. Integrated Surface and Subsurface Hydrological Modelling with Snowmelt and Pore Water Freeze–Thaw. Groundwater 57(1): 63–74.

Seck, A., Welty, C., and Maxwell, RM. 2015. Spin-up Behavior and Effects of Initial Conditions for an Integrated Hydrologic Model. Water Resources Research 51: 2188–2210.

Shojae Ghias, M., Therrien, R., Molson, J., and Lemieux, JM. 2016. Controls on Permafrost Thaw in a Coupled Groundwater-Flow and Heat-Transport System: Iqaluit Airport, Nunavut, Canada. Hydrogeology Journal (2007). http://link.springer.com/10.1007/s10040-016-1515-7.

Sjöberg, Y., Frampton, A., and Lyon, SW. 2013. Using Streamflow Characteristics to Explore Permafrost Thawing in Northern Swedish Catchments. Hydrogeology Journal 21(1): 121–31.

Smith, Craig D. 2007. Correcting the Wind Bias in Snowfall Measurements Made with a Geonor T-200B Precipitation Gauge and Alter Wind Shield. Proceedings of the 14th SMOI, San Antonio (October).

Sterte, EJ., Johansson, E., Sjoberg, Y., Karlsen, RH., Laudon, H. 2018. "Groundwater-Surface Water Interactions across Scales in a Boreal Landscape Investigated Using a Numerical Modelling Approach." Journal of Hydrology 560: 184–201. https://doi.org/10.1016/j.jhydrol.2018.03.011.

Therrien, R., McLaren, R.G., Sudicky, E.a., and Panday, S.M. 2010. HydroGeoSphere A Three-Dimensional Numerical Model Describing Fully-Integrated Subsurface and Surface Flow and Solute Transport. R. Therrien, E.A. Sudicky, R.G. McLaren Groundwater Simulation Group.

Thompson, C., Mendoza, CA., Devito, KJ., Petrone, RM. 2015. Climatic controls on groundwater–surface water interactions within the Boreal Plains of Alberta: Field observations and numerical simulations, 2015, 734-746.

Van der Gun, J. (2012). Groundwater and global change:trends, opportunities and challenges. (p. 38 pp). Paris, France: Assessment Programme Side Publications Series UNESCO.

Weill, S. Altissimo, M., Cssiani, G., Deiana, R., Marani, M., Putti, M. 2013. Saturated Area Dynamics and Streamflow Generation from Coupled Surface-Subsurface Simulations and Field Observations. Advances in Water Resources 59: 196–208. http://dx.doi.org/10.1016/j.advwatres.2013.06.007.

Wood, A W, Leung, LR., Sridhar, V., and Lettenmaier, DP. 2004. Hydrologic Implications of Dynamical and Statistical Approaches To Downscaling Climate Model Outputs. 189–216.

Yang, D., Kane, D., Zhang, Z., Legates, D., Goodison, B. 2005. Bias Corrections of Long-Term (1973-2004) Daily Precipitation Data over the Northern Regions. Geophysical Research Letters 32(19): 1–5.

Annexe Processing of measured precipitation data

The following steps explain how the precipitation data were processed in this project.

1- Eliminate changes associated with gauge services, e.g. emptying the bucket and adding the antifreeze

2- Implementing a “Brute-force” filtering algorithm to eliminate negative and small positive (less than 0.1 mm) changes. This method aggregates these values with the nearest positive value above the threshold of 0.1 mm. The method preserves the total accumulated precipitation but aggregates all changes into values above the threshold. The Matlab code used in this step (removenegative.M) is as follows:

```
Rf = xlsread('prec.xls');
time = xlsread('time.xls');
k = length(Rf);
Rf_init = Rf;
iter_num = 1;


while min(Rf) < 0
    [minval,minIdx] = min(Rf);
    new_Rf_Idx = knnsearch(time,time(minIdx),'K',k)';
    new_Rf = Rf(new_Rf_Idx,1);
    Rf_nearest_pos = new_Rf_Idx(find(new_Rf > 0,1),1);
    if ~isempty(Rf_nearest_pos)
        Rf(Rf_nearest_pos,1) = Rf(minIdx,1) + Rf(Rf_nearest_pos,1);
    end
    Rf(minIdx)=0;
    iter_num = iter_num + 1;
    disp(iter_num);
end
xlswrite('precip.xls',Rf);
```

To use Matlab for removing negative values:

a. Save the hourly precipitation data in .xls format with no heading

b. Save the time in decimal format

c. Run the removenegative.M

Therefore, the precip.xls file is the precipitation data without the negative values.

3- Calculate the wind speed at gauge height (Pan, Yang, Li, Barr, Helgason, Hayashi, Marsh, Pomeroy and Richard J. Janowicz, 2016):

$$W_s(h) = W_s(H)\left[\frac{\ln\left(\frac{h}{z_0}\right)}{\ln\left(\frac{H}{z_0}\right)}\right]$$

$Ws(h)$: wind speed at gauge height (m/s), $\mathrm{Ws(H)}$: wind speed measured by anemometer (m/s) h: Elevation of Geonor (1.75 m) H: Elevation of anemometer (3m) z_0:roughness(m) here I considered $z_0 = 0.001m$ for $T_a < 0$ $z_0 = 0.02m$ for $T_a \geq 0$, T_a :air temperature (°C)

4- Calculate the coefficient of efficiency (CE):

$\mathrm{T_a} \geq 1°\mathrm{C}$ Rain CE=1

$T_a < 1°C$ Snow :

if	$Ws(h)$ >6 (m/s)	$CE = 0.4$
if	$Ws(h)$ <1.2 (m/s)	$CE = 1$
if	1.2< $Ws(h)$ <6	$\mathrm{CE}=1.18e^{-0.18\mathrm{W_s(h)}}$

$\mathrm{P_{cor}} = \mathrm{P_{obs}} / \mathrm{CE}$ P_{cor}: Corrected precipitation (mm) P_{obs}: measured precipitation after filtering

Mixed snow-rain was not considered because another student had already done this and there wasn't much difference in the final results.

Step 3 and 4 are included in the following Matlab code (precipitation_process.M):

```
%insert the data
pr=xlsread('precip.xls');
temp=xlsread('temp.xls');
wind=xlsread('wind.xls');
L=length(pr);
z0=zeros(L,1);
wind2=zeros(L,1);
CE=zeros(L,1);
pr_edit=zeros (L,1);
for i=1:L; %define z0
    if temp(i,1)<0
        z0(i,1)=0.01;
    else
        z0(i,1)=0.03;
    end
    wind2(i,1)=wind(i,1)*((log(1.75/(z0(i,1))))/(log(10/(z0(i,1)))));

    if temp(i,1)>1

    CE(i,1)=1;
    else if wind2(i,1)<1.2
            CE(i,1)=1;
        else if wind2(i,1)>6
                CE(i,1)=0.4;
            else
                CE(i,1)=1.18*exp(-0.18*wind2(i,1));
```

```
            end
        end
    end

    pr_edit(i,1)=pr(i,1)/CE(i,1);

end



xlswrite('CE.xls',CE);
xlswrite('wind_at_gauge.xls',wind2);
xlswrite('pr_edit',pr_edit);
```

After running the precipitation_process.M, CE.xls, wind_at_gauge.xls, and pr_edit are CE, wind speed at the gauge height and edited precipitation, respectively.